The Astrophysical Journal Letters, 955:L6 (31pp), 2023 September 20 https://doi.org/10.3847/2041-8213/acf216

Tidal Disruption Event Demographics with the Zwicky Transient Facility: Volumetric Rates, Luminosity Function, and Implications for the Local Black Hole Mass Function

Yuhan Yao[1,2,3], Vikram Ravi[1], Suvi Gezari[4,5], Sjoert van Velzen[6], Wenbin Lu[3], Steve Schulze[7], Jean J. Somalwar[1], S. R. Kulkarni[1], Erica Hammerstein[8], Matt Nicholl[9,10], Matthew J. Graham[1], Daniel A. Perley[11], S. Bradley Cenko[12,13], Robert Stein[1], Angelo Ricarte[14,15], Urmila Chadayammuri[14], Eliot Quataert[16], Eric C. Bellm[17], Joshua S. Bloom[3], Richard Dekany[18], Andrew J. Drake[1], Steven L. Groom[19], Ashish A. Mahabal[20,21], Thomas A. Prince[1], Reed Riddle[18], Ben Rusholme[19], Yashvi Sharma[1], Jesper Sollerman[22], and Lin Yan[1]

[1] Cahill Center for Astrophysics, California Institute of Technology, MC 249-17, 1200 E California Boulevard, Pasadena, CA 91125, USA; yuhanyao@berkeley.edu
[2] Miller Institute for Basic Research in Science, 468 Donner Lab, Berkeley, CA 94720, USA
[3] Department of Astronomy, University of California, Berkeley, CA 94720, USA
[4] Space Telescope Science Institute, 3700 San Martin Drive, Baltimore, MD 21218, USA
[5] Department of Physics and Astronomy, Johns Hopkins University, Baltimore, MD 21218, USA
[6] Leiden Observatory, Leiden University, Postbus 9513, 2300 RA, Leiden, The Netherlands
[7] Department of Physics, The Oskar Klein Centre, Stockholm University, AlbaNova, SE-10691 Stockholm, Sweden
[8] Department of Astronomy, University of Maryland, College Park, MD 20742, USA
[9] Birmingham Institute for Gravitational Wave Astronomy and School of Physics and Astronomy, University of Birmingham, Birmingham B15 2TT, UK
[10] Astrophysics Research Centre, School of Mathematics and Physics, Queens University Belfast, Belfast BT7 1NN, UK
[11] Astrophysics Research Institute, Liverpool John Moores University, IC2, Liverpool Science Park, 146 Brownlow Hill, Liverpool L3 5RF, UK
[12] Astrophysics Science Division, NASA Goddard Space Flight Center, Greenbelt, MD 20771, USA
[13] Joint Space-Science Institute, University of Maryland, College Park, MD 20742, USA
[14] Center for Astrophysics | Harvard & Smithsonian, 60 Garden Street, Cambridge, MA 02138, USA
[15] Black Hole Initiative at Harvard University, 20 Garden Street, Cambridge, MA 02138, USA
[16] Department of Astrophysical Sciences, Princeton University, Princeton, NJ 08544, USA
[17] DIRAC Institute, Department of Astronomy, University of Washington, 3910 15th Avenue NE, Seattle, WA 98195, USA
[18] Caltech Optical Observatories, California Institute of Technology, Pasadena, CA 91125, USA
[19] IPAC, California Institute of Technology, 1200 E. California Blvd, Pasadena, CA 91125, USA
[20] Division of Physics, Mathematics and Astronomy, California Institute of Technology, Pasadena, CA 91125, USA
[21] Center for Data Driven Discovery, California Institute of Technology, Pasadena, CA 91125, USA
[22] Department of Astronomy, The Oskar Klein Centre, Stockholm University, AlbaNova, SE-10691 Stockholm, Sweden
Received 2023 March 11; revised 2023 August 3; accepted 2023 August 11; published 2023 September 15

Abstract

We conduct a systematic tidal disruption event (TDE) demographics analysis using the largest sample of optically selected TDEs. A flux-limited, spectroscopically complete sample of 33 TDEs is constructed using the Zwicky Transient Facility over 3 yr (from 2018 October to 2021 September). We infer the black hole (BH) mass ($M_{\rm BH}$) with host galaxy scaling relations, showing that the sample $M_{\rm BH}$ ranges from $10^{5.1}\,M_\odot$ to $10^{8.2}\,M_\odot$. We developed a survey efficiency corrected maximum volume method to infer the rates. The rest-frame g-band luminosity function can be well described by a broken power law of $\phi(L_g) \propto [(L_g/L_{\rm bk})^{0.3} + (L_g/L_{\rm bk})^{2.6}]^{-1}$, with $L_{\rm bk} = 10^{43.1}\,{\rm erg\,s^{-1}}$. In the BH mass regime of $10^{5.3} \lesssim (M_{\rm BH}/M_\odot) \lesssim 10^{7.3}$, the TDE mass function follows $\phi(M_{\rm BH}) \propto M_{\rm BH}^{-0.25}$, which favors a flat local BH mass function ($dn_{\rm BH}/d\log M_{\rm BH} \approx$ constant). We confirm the significant rate suppression at the high-mass end ($M_{\rm BH} \gtrsim 10^{7.5}\,M_\odot$), which is consistent with theoretical predictions considering direct capture of hydrogen-burning stars by the event horizon. At a host galaxy mass of $M_{\rm gal} \sim 10^{10}\,M_\odot$, the average optical TDE rate is $\approx 3.2 \times 10^{-5}\,{\rm galaxy^{-1}\,yr^{-1}}$. We constrain the optical TDE rate to be [3.7, 7.4, and 1.6] $\times 10^{-5}\,{\rm galaxy^{-1}\,yr^{-1}}$ in galaxies with red, green, and blue colors.

Unified Astronomy Thesaurus concepts: Tidal disruption (1696); Time domain astronomy (2109); Black holes (162); Galaxy nuclei (609); Supermassive black holes (1663); Luminosity function (942)

Supporting material: machine-readable tables

1. Introduction

In the local universe, a small fraction (∼10%) of galaxies host active massive black holes (BHs) in their nuclei (Kewley et al. 2006; Aird et al. 2012). The remaining massive BHs are quiescent, but can be temporarily *awakened* when a star comes too close to it and becomes disrupted by tidal forces. The stellar debris evolves into an elongated stream, approximately half of which comes back to get accreted (Rees 1988). This produces an electromagnetic flare if the tidal radius $R_{\rm T}$ (where the self gravity of the star balances the tidal forces) is greater than the size of the BH event horizon. Since $R_{\rm T} \propto M_{\rm BH}^{1/3}$ and the size of the event horizon $\propto M_{\rm BH}$, there exists a maximum BH mass for an observable TDE—the so-called Hills mass. For Sun-like stars, $M_{\rm Hills} \sim 10^{8}\,M_\odot$ (Hills 1975).

The first tidal disruption event (TDE) was identified with the ROSAT all-sky X-ray survey, where the soft X-rays are thought to come from a newly formed accretion disk (Bade et al. 1996; Grupe et al. 1999; Saxton et al. 2020). Recently, the eROSITA telescope (Predehl et al. 2021) on

board the Spektrum-Roentgen-Gamma (SRG) X-ray mission (Sunyaev et al. 2021) reported 13 TDEs selected from the second eROSITA all-sky survey (Sazonov et al. 2021). Low-temperature (few $\times 10^4$ K) thermal emission from TDEs has been discovered with UV and optical sky surveys (Gezari et al. 2006; van Velzen et al. 2011; Gezari et al. 2012; Arcavi et al. 2014; Holoien et al. 2014; Hung et al. 2017), which has been postulated to arise from either energy dissipation within a stream–stream collision shock (Piran et al. 2015; Jiang et al. 2016) or reprocessing of high-energy photons (Metzger & Stone 2016; Roth et al. 2016). In the latter scenario, the physical origin of the "reprocessing layer" may be the optically thick gas from the self-collision shock (Lu & Bonnerot 2020), a radiation-driven outflow formed under super-Eddington accretion (Miller 2015; Dai et al. 2018; Thomsen et al. 2022), or a quasi-static weakly bound envelope (Loeb & Ulmer 1997; Coughlin & Begelman 2014; Metzger 2022).

Theoretically, the TDE rate is determined by processes that govern stellar diffusion into the "loss cone," which defines a phase-space volume of orbits with angular momentum $J \leqslant J_{\rm lc} \equiv \sqrt{2GM_{\rm BH}R_{\rm T}}$ (Alexander 2017; Stone et al. 2020). Observational constraints on TDE demography can help address various open questions in astrophysics. First, the TDE luminosity function (LF) provides clues to how the emission mechanism is tied to the loss-cone filling (Kochanek 2016; Stone & Metzger 2016; Stone et al. 2020) and provides an essential input to predict TDE rates in future sky surveys.

Moreover, measuring the volumetric rate of TDEs as a function of $M_{\rm BH}$ offers a unique approach to trace the local BH population. At the low-mass end ($M_{\rm BH} \lesssim 10^6\,M_\odot$), the TDE mass function depends on the unknown bottom end of the massive black hole mass function (BHMF). The space density of such intermediate-mass black holes (IMBHs) encodes formation mechanisms of primordial BHs in the early Universe at redshifts of $z > 10$ (Ricarte & Natarajan 2018a; Woods et al. 2019; Greene et al. 2020; Chadayammuri et al. 2023). The mergers of IMBHs and extreme mass-ratio inspirals are prime targets for the upcoming space-based gravitational-wave detector Laser Interferometer Space Antenna (Amaro-Seoane et al. 2017; Jani et al. 2020; Amaro Seoane 2022).

At the high-mass end, the location of the TDE mass function's cutoff is set by the size of the event horizon, which probes the spin distribution of BHs in the mass range of $10^{7.5}\,M_\odot \lesssim M_{\rm BH} \lesssim 10^{8.5}\,M_\odot$ (Kesden 2012; Stone et al. 2019; Du et al. 2022; Huang & Lu 2022). The spin of such quiescent BHs cannot be measured via the traditional method of X-ray reflection spectroscopy (Reynolds 2021) developed for X-ray binaries and active galactic nulei (AGN).

van Velzen (2018) made the first attempt to construct the TDE LF and mass function. Using a sample of 13 objects selected from five different UV and optical sky surveys, the authors inferred a rest-frame g-band LF of $dN/dL_g \propto L_g^{-5/2}$ for $L_g \in (10^{42.3}, 10^{44.8})$ erg s^{-1} and a nearly constant TDE mass function for $M_{\rm BH} \in (10^{5.8}, 10^{7.3})M_\odot$. While these early results have demonstrated the important role that TDEs play in understanding BH demographics, they are susceptible to small number statistics and the heterogeneous nature of the sample.

Over the past few years, time domain sky surveys have led to a surge of TDE discoveries. The Zwicky Transient Facility (ZTF; Bellm et al. 2019a; Graham et al. 2019) is one of the most prolific optical discovery engines. Previous ZTF TDE sample studies have made significant progress on characterizing the photometric and spectroscopic properties of TDEs (van Velzen et al. 2021; Hammerstein et al. 2023). However, since the classification completeness of photometric candidates was not assessed, recent studies that attempt to constrain the TDE optical LF using previously published ZTF TDE samples (e.g., Lin et al. 2022; Charalampopoulos et al. 2023) had to rely on false assumptions regarding the spectroscopic completeness. In this work, we aim to put new observational constraints on TDE demography. To this end, we constructed a flux-limited, spectroscopically complete sample of 33 TDEs selected from 3 yr of the ZTF operation.

This paper is organized as follows. The procedures of the TDE sample selection, observation, and classification are outlined in Section 2. UV and optical light-curve fitting is described in Section 3. Host galaxy observation and analysis (including measurements of the $M_{\rm BH}$) are presented in Section 4. The survey efficiency is assessed in Section 5. We compute and discuss the volumetric rate of optical TDEs as a function of $M_{\rm BH}$, L_g, as well as other host galaxy and transient properties in Section 6. We summarize our conclusions in Section 7.

UT time is used throughout the paper. We assume a basic cosmology of $\Omega_{\rm M} = 0.3$, $\Omega_\Lambda = 0.7$, and $h = 0.7$. Optical magnitudes are reported in the AB system. Assuming $R_V = 3.1$, we correct the observed photometry for Galactic extinction using the Cardelli et al. (1989) extinction law and the Schlafly & Finkbeiner (2011) extinction map. The coordinates are given in J2000. We use t to denote rest-frame time relative to the maximum-light epoch.

2. Sample Construction

2.1. The ZTF TDE Experiment

ZTF is an optical time domain sky survey operated by the Palomar Observatory. It uses the Palomar Oschin Schmidt 48 inch telescope (P48) equipped with a 47 deg^2 camera (Dekany et al. 2020) to scan the entire northern visible sky at decl. $> -35.^\circ2$. The three ZTF filters (g, r, and i) were designed to maximize throughput by avoiding major Palomar sky lines. The typical survey depth is $\sim$20.5 mag (Graham et al. 2019).

Image processing and reference subtraction are performed by the ZTF Science Data System (Masci et al. 2019). Every 5σ point-source detection is saved as an "alert" in the Avro format and distributed to community brokers via the ZTF Alert Distribution System (Patterson et al. 2019). The alerts are enhanced with additional contextual information such as the machine-learning real-bogus score (Duev et al. 2019; Mahabal et al. 2019), the proximity to the nearest object in archival catalogs (Soumagnac & Ofek 2018), and the star–galaxy classifier (Tachibana & Miller 2018).

ZTF phase I (hereafter ZTF-I) ran from 2018 March to 2020 September, during which 40% of the total time was dedicated to two public sky surveys, including a Northern sky survey ($1g + 1r$ every 3 days) and a Galactic Plane survey (Bellm et al. 2019b). On 2020 October 1, ZTF increased the MSIP/NSF-funded public program to 50% of the total time, and the Northern sky survey cadence was shortened from 3 to 2 days. Therefore, in this paper, we use 2020 October 1 as the start of ZTF phase II (hereafter ZTF-II).[23]

[23] Note that some other publications from the ZTF collaboration (such as Hammerstein et al. 2023) consider 2020 December as the start of ZTF-II, as the Phase II Partnership surveys did not begin until that time.

Table 1
Steps for Selecting TDE Candidates

Step	Criteria	# TDE Candidates
1	Initial cuts to select nuclear transients	890,266
2	More detailed cuts to select nuclear transients	143,731
3	Cuts on peak magnitude, transient duration, and number of detections	9426
4	Cuts on the peak color, PS1 machine-learning classification, and IR variability; remove known quasars	1390
5	Alert photometry: cuts on color, cooling rate, and rise and decline timescales	174
6	Forced photometry: cuts on color, cooling rate, and rise and decline timescales	90
7	Cuts on peak magnitude (of forced photometry)	55
8	Spectroscopic classification for 50 objects; photometric and contextual classification for 5 objects	33

The ZTF team selects nuclear transients in real-time by filtering public alerts with the `AMPEL` broker (Nordin et al. 2019). Details of our filtering techniques are described in van Velzen et al. (2019, 2021). AT2018zr is the first TDE selected by the ZTF nuclear transient filter (van Velzen et al. 2019). Afterwards, van Velzen et al. (2021) presented 17 TDEs selected within the first 1.5 yr of ZTF-I operation, and introduced three distinct spectroscopic subclasses of optically selected TDEs (TDE-H, TDE-H+He, and TDE-He) based on the existence of a combination of broad emission lines around Hα, Hβ, and He II λ4686. Recently, Hammerstein et al. (2023) presented a sample of 30 spectroscopically classified TDEs from the entirety of ZTF-I, and reported a new spectroscopic subclass called "TDE-featureless," which is characterized by a lack of broad emission lines in optical spectra.

Entering into ZTF-II, the TDE experiment was carried out with more spectroscopic follow-up resources allocated from the Keck and Palomar Observatories, which allowed us to classify a larger number of fainter TDE candidates.

The follow-up campaign in ZTF was conducted on a best effort basis. We tried to classify as many TDE candidates as possible, with higher priorities of spectroscopic observations given to objects with brighter peak magnitudes. Unlike previous ZTF work, we here seek to construct a flux-limited sample of TDEs, enabling a systematic study of optical TDE demographics. Therefore, we performed a retrospective search of nuclear transients using historical ZTF alerts, and applied a set of well-defined criteria to select TDE candidates (see Section 2.2). We then find the peak magnitude limits (in ZTF-I and ZTF-II separately) below which our spectroscopic classification is almost ($\gtrsim$90%) complete (see step (7) in Section 2.2). And for the few candidates with no (or ambiguous) spectroscopic classification, we determine the transient type using the photometric properties and other information (see details in Section 2.4).

2.2. Retrospective Candidate Filtering

Table 1 presents a summary of the candidate filtering steps.

1. We applied basic cuts to select nuclear transients. We kept alerts with a real-bogus score `rb>0.5` (Mahabal et al. 2019) or a deep learning score `drb>0.65` (Duev et al. 2019),[24] a position within 0.″6 to the location of the nearest object in the Panoramic Survey Telescope and Rapid Response System Data Release 1 (PS1; Chambers et al. 2016) catalog (`distpsnr1<0.6`) or hostless (`distpsnr1==-999`). We removed alerts in negative subtractions. We kept alerts in coincidence with objects with galaxy-like morphologies, selected using a cut on the star–galaxy score (Tachibana & Miller 2018) of `sgscore1<0.8`. This step left 890,266 unique sources.
2. We kept objects first detected between 2018 October 1 and 2021 September 30, i.e., the last 2 yr of ZTF-I[25] and the first year of ZTF-II. We require that, in either g or r band, the transient is within 0.″6 to the location of the nearest object in the ZTF reference image (`distnr<0.6`). If the nearest reference object is brighter than 15 mag (`magnr<=15`), we require `sgscore1<0.2`; similarly, we require `sgscore1<=0.5` for `15<magnr<=18` and `sgscore1<0.8` for `magnr>18`. This left 143,731 sources.
3. We define n_g (n_r) as the number of detections in g band (r band), and $t_{\rm dur}$ as the duration of all detections. The peak magnitudes in the g and r bands are $m_{g,\rm peak}$ and $m_{r,\rm peak}$, respectively. We required $m_{g,\rm peak} < 19.5$ mag, $m_{r,\rm peak} < 19.5$ mag, $t_{\rm dur} > 30$ d, $n_g > 10$, and $n_r > 10$. This left 9426 sources.
4. We applied a few cuts to remove stellar and AGN variability. We required $m_{g,\rm peak} - m_{r,\rm peak} < 1$, and that the closest object in the "Pan-STARRS1 Source Types and Redshifts with Machine learning" catalog (Beck et al. 2021) is not classified as "QSO" or "STAR." We removed objects with a counterpart in the Million Quasars catalog (Milliquas v6.3, Flesch 2019). We constructed a W1-band light curve from the NeoWISE (Mainzer et al. 2011) photometry prior to the first ZTF detection, and rejected any galaxies with significant variability in the W1 band (χ^2/degrees of freedom> 10). This left 1390 sources.
5. We selected candidates based on the alert photometry. We kept objects with at least 5 nights of post-peak multiband photometry. We required the rate of post-peak g–r color change to be <0.02 mag day^{-1}, and the mean g–r color to be <0.2 mag. We calculated the rise and decay e-folding times in the alert photometry light curve (smoothed with a Gaussian process). We required the rise e-folding time to be $2 < t_{e,\rm rise} < 300$ d, and the decline e-folding time to be $2 < t_{e,\rm decline} < 300$ d. This step left 174 sources, including 104 sources first detected during ZTF-I, and 70 sources first detected during the first year of ZTF-II.

[24] The deep learning score was not included in the alert packets until 2019 June 19. Therefore, we used `rb` and `drb` for alerts released before and after that date, respectively.

[25] Due to a likely low recovery efficiency for TDEs detected in the reference images, we do not consider events first detected before 2018 October 1, when ZTF reference images for most fields were still being constructed.

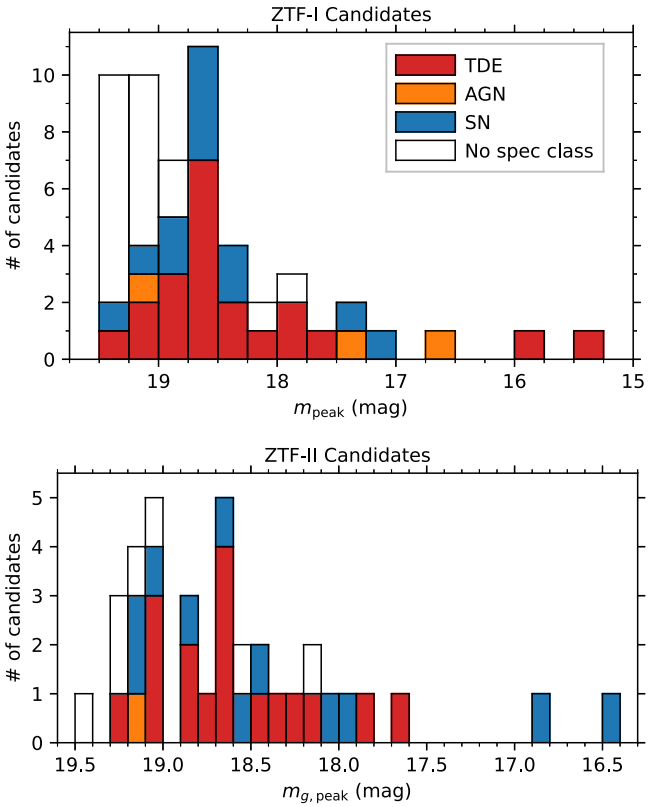

Figure 1. Histograms of the photometric TDE candidates that passed the filtering step (6) (see Table 1), color-coded by their spectroscopic classifications. For ZTF-I candidates, the spectroscopic classification is ∼93% complete at $m_{\rm peak} < 18.75$. For ZTF-II candidates, the spectroscopic classification is ∼89% complete at $m_{g,\rm peak} < 19.1$.

6. We ran forced point-spread function (PSF) photometry, which provide more accurate light curves. We also visually examined the light curves and excluded 8 objects[26] that are reminiscent of AGN and one object[27] with a typical dwarf nova light curve. We applied the criteria outlined in step (4) to the ZTF forced photometry. This left 90 sources, including 54 in ZTF-I and 36 in ZTF-II.
7. We found that for candidates in ZTF-I, our spectroscopic classification completeness was ∼93% at $m_{\rm peak} < 18.75$; for candidates in ZTF-II, our spectroscopic classification completeness was ∼89% complete at $m_{g,\rm peak} < 19.1$ (see Figure 1). Therefore, we kept ZTF-I sources with $m_{\rm peak} < 18.75$, and ZTF-II sources with $m_{g,\rm peak} < 19.1$. This left 55 sources, including 27 in ZTF-I and 28 in ZTF-II.

A few notes are worth mentioning. First, as pointed out in van Velzen et al. (2021), by applying step (4), our search is biased against TDEs hosted by AGN, such as PS1-16dtm (Blanchard et al. 2017) and ZTF20abisysx/AT2020nov (Dahiwale & Fremling 2020a). The local AGN fraction for galaxies throughout the stellar mass range of $9.5 < \log(M_{\rm gal}/M_\odot) < 12$ is $\lesssim$10% (Kewley et al. 2006; Aird et al. 2012), and the fraction is even lower in dwarf galaxies (Latimer et al. 2021a). Therefore, the majority of TDEs should be hosted by quiescent galaxies without strong AGN activity, unless the rate is enhanced by a factor ∼10 in AGN. Second, unlike previous ZTF TDE sample studies, we do not reject candidates based on the mean W1–W2 color of their host galaxies, since recent studies have found that some star-forming dwarf galaxies also exhibit red neoWISE colors (Latimer et al. 2021b). Third, in steps (5) and (6), the cuts on color and cooling rate are defined such that all TDEs presented in van Velzen et al. (2021), Angus et al. (2022), and Hammerstein et al. (2023) satisfy the selection criteria. Finally, we show in Appendix B that our cuts on `sgscore1`, $t_{e,\rm rise}$, and $t_{e,\rm decline}$ do not hit the boundary of the selection.

2.3. Observations

2.3.1. UV and Optical Photometry

For all TDE candidates, we constructed the optical and UV light curves using data from ZTF, the Asteroid Terrestrial-impact Last Alert System (ATLAS; Tonry et al. 2018; Smith et al. 2020; Shingles et al. 2021), and the Ultra-Violet/Optical Telescope (UVOT; Roming et al. 2005) on board the Neil Gehrels Swift Observatory (Gehrels et al. 2004). Data reduction procedures follow those outlined in van Velzen et al. (2021), Hammerstein et al. (2023). We show the Galactic extinction-corrected g–r evolution in ZTF forced photometry in Figure 2. The photometry of the final sample of 33 TDEs is presented in Appendix A.

2.3.2. Optical Spectroscopy

To spectroscopically classify the TDE candidates, we obtained low-resolution optical spectra with the Spectral Energy Distribution Machine (SEDM; Blagorodnova et al. 2018; Rigault et al. 2019; Kim et al. 2022) on the robotic Palomar 60 inch telescope (P60; Cenko et al. 2006), the Low Resolution Imaging Spectrograph (LRIS; Oke et al. 1995) on the Keck I telescope, the Double Spectrograph (DBSP; Oke & Gunn 1982) on the 200 inch Hale telescope, and the De Veny Spectrograph on the Lowell Discovery Telescope (LDT). Note that all DBSP observations are affected by a CCD malfunction, which results in a wavelength gap between 5750 and 6200 Å. The instrument configurations and data reduction procedures follow those described in Appendix B of Yao et al. (2022a).

We also made use of spectra uploaded to the transient name server (TNS) by other groups. For each TDE that was not previously reported in the literature, we release at least one optical spectrum in this paper. An observing log of the released data is provided in Appendix A (Table 7).[28]

2.4. Classification

As mentioned in Section 2.2, five of the 55 photometrically selected TDE candidates do not have spectroscopic classifications. Using light curves, host galaxy spectroscopy, and multiwavelength information (see details below), we classify ZTF19aaciohh and ZTF20acvezvs as *TDE?*, ZTF19aaywayr

[26] ZTF18accdkxa, ZTF18acenyfr, ZTF18acpjddi, ZTF19acblzqb, ZTF19abkftuu, ZTF19abukbuc, ZTF20absxaaj, and ZTF20abzpysa show stochastic variability.

[27] ZTF21abiplqz has a fast rise, a rapid decline followed by a sudden flux frop, and a blue optical conterpart.

[28] Upon publication, all spectra in Table 7 will be available in electronic format on the Weizmann Interactive Supernova Data Repository (Yaron & Gal-Yam 2012).

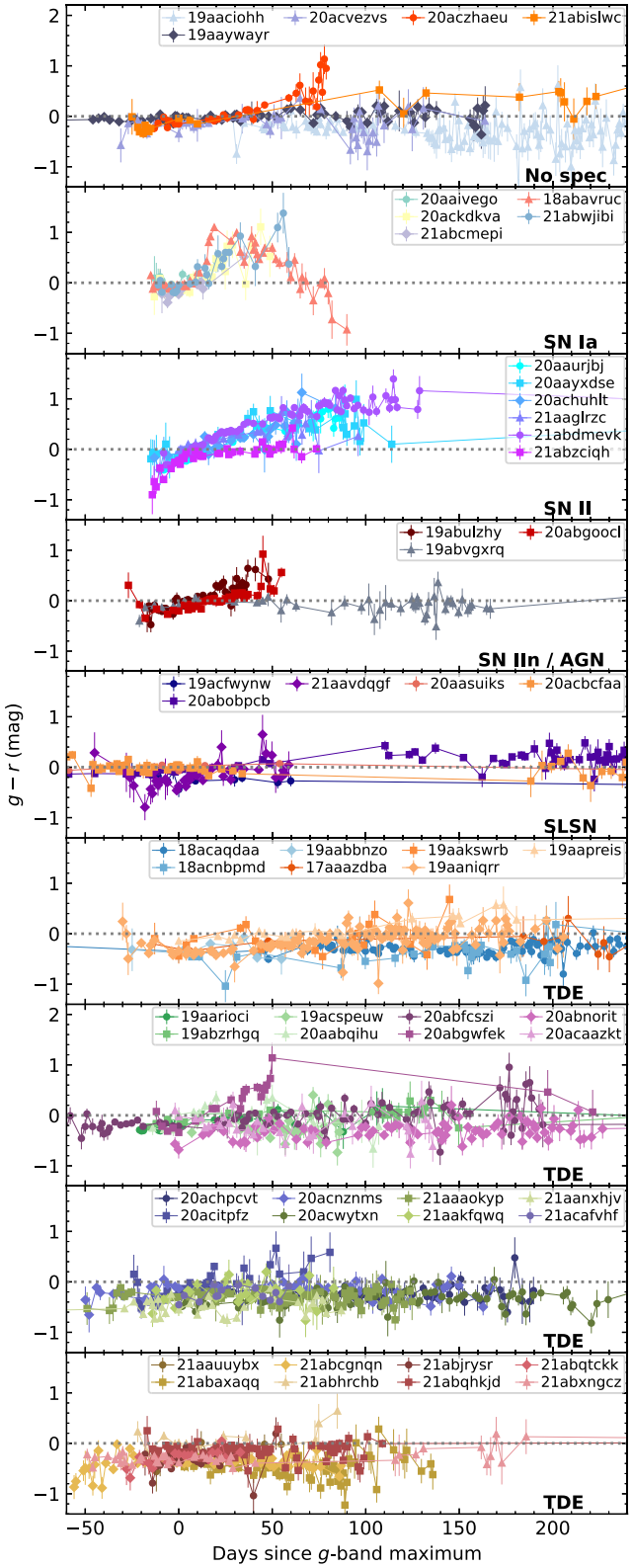

Figure 2. g–r evolution of the 55 TDE candidates. The top panel shows 5 objects without spectroscopic classifications, and the other 8 panels show 50 spectroscopically classified objects. Color has been corrected for Galactic extinction.

as *AGN?*, and ZTF20aczhaeu and ZTF21abislwc as *SN?*. Tables 2 and 3 summarize 22 false positives and 33 TDEs. Below, we comment on the individual events.

Table 2
Spectroscopic Classifications of 22 False Positives

ZTF name	Class	Reference
ZTF18abavruc	SN Ia	Angus (2021)
ZTF20aaivego	SN Ia	Dahiwale & Fremling (2020b)
ZTF20ackdkva	SN Ia	Dahiwale & Fremling (2020c)
ZTF21abcmepi	SN Ia	SNIascore (2021)
ZTF21abwjibi	SN Ia	Yao (2022)
ZTF20aaurjbj	SN II	Siebert (2020)
ZTF20aayxdse	SN II	Dahiwale & Fremling (2020d)
ZTF20achuhlt	SN II	Yan et al. (2020)
ZTF21aaglrzc	SN II	Dahiwale & Fremling (2021)
ZTF21abdmevk	SN II	Bruch et al. (2021)
ZTF21abzciqh	SN II	Chu et al. (2021a)
ZTF19abulzhy	SN IIn	Dahiwale & Fremling (2020e)
ZTF20abgoocl	SN IIn	Perley et al. (2020a)
ZTF19acfwynw	SLSN-I	Nicholl et al. 2019b
ZTF20abobpcb	SLSN-I	Perez-Fournon et al. (2020)
ZTF21aavdqgf	SLSN-I	Yao et al. (2021c)
ZTF20aasuiks	SLSN-II	Tucker (2021)
ZTF20acbcfaa	SLSN-II	Pessi et al. (2020)
ZTF19abvgxrq	AGN	Frederick et al. (2021); Yu et al. (2022)
ZTF21abislwc	SN?	This work
ZTF20aczhaeu	SN?	This work
ZTF19aaywayr	AGN?	This work

2.4.1. False Positives

Among the list of 22 false positives, spectroscopic classifications are available for 19 objects: five were classified as Type Ia supernovae (SNe Ia); six were classified as Type II SNe (SNe II); two were classified as Type IIn SNe (SNe IIn); three were classified as hydrogen-poor superluminous SNe (SLSNe-I); two were classified as hydrogen-rich SLSNe (SLSNe-II); one was classified as an AGN. ZTF20aczhaeu and ZTF21abislwc are probably SNe since their post-peak color reddened significantly, which is different from known TDEs (see Figure 2).

ZTF19aaywayr is probably a slow AGN flare. In the forced photometry light curve, it has two peaks: the first at $m_r = 19.9$ mag in 2019 June, and the second at $m_r = 18.1$ mag in 2020 September. The rise time of the second peak is ≈400 days, which is a factor of ∼10 longer than the typical rise time of the spectroscopically classified TDE sample. Therefore, we think it is more likely to be an AGN.

2.4.2. True Positives

The TDE classifications of 15 objects (IDs 1–3, 5–6, 8–15, 18, 24) have been previously reported in refereed papers (Arcavi et al. 2020; Nicholl et al. 2020; Hinkle et al. 2021; Stein et al. 2021; van Velzen et al. 2021; Yao et al. 2022a; Angus et al. 2022; Hammerstein et al. 2023).

Two objects were detected in the radio band with the Very Large Array Sky Survey (VLASS; Lacy et al. 2020). In short, *ZTF19aaciohh/AT2019baf (ID 4)* is hosted by a galaxy with Seyfert-like emission line ratios. Multiwavelength properties suggest that it is likely a TDE associated with a jet. *ZTF20acaazkt/AT2020vdq (ID 16)* can be spectroscopically classified as a TDE based on the existence of intermediate-width (∼700 km s^{-1}) transient Balmer lines, He II, and Fe X emission lines. Detailed properties of these two events will be presented as part of a sample of VLASS-selected TDE

Table 3
Basic Information of 33 TDEs in Our Sample

ID	ZTF Name	IAU Name	R.A. (deg)	Decl. (deg)	Redshift	TDE Report	Spectral Subtype
1	ZTF18acaqdaa	AT2018iih	262.0163662	30.6920758	0.212	van Velzen et al. (2021)	TDE-He
2	ZTF18acnbpmd	AT2018jbv	197.6898587	8.5678292	0.340	Hammerstein et al. (2023)	TDE-featureless
3	ZTF19aabbnzo	AT2018lna	105.8276892	23.0290953	0.0914	van Velzen et al. (2021)	TDE-H+He
4	ZTF19aaciohh	AT2019baf	268.0005082	65.6266546	0.0890	This paper; J. Somalwar et al. (2023, in preparation)	Unknown
5	ZTF17aaazdba	AT2019azh	123.3206388	22.6483180	0.0222	Hinkle et al. (2021)	TDE-H+He
6	ZTF19aakswrb	AT2019bhf	227.3165243	16.2395720	0.121	van Velzen et al. (2021)	TDE-H
7	ZTF19aaniqrr	AT2019cmw	282.1644974	51.0135422	0.519	This paper; J. Wise et al. (2023, in preparation)	TDE-featureless
8	ZTF19aapreis	AT2019dsg	314.2623552	14.2044787	0.0512	Stein et al. (2021)	TDE-H+He
9	ZTF19aarioci	AT2019ehz	212.4245268	55.4911223	0.0740	van Velzen et al. (2021)	TDE-H
10	ZTF19abzrhgq	AT2019qiz	71.6578313	−10.2263602	0.0151	Nicholl et al. (2020)	TDE-H+He
11	ZTF19acspeuw	AT2019vcb	189.7348778	33.1658869	0.0890	Hammerstein et al. (2023)	TDE-H+He
12	ZTF20aabqihu	AT2020pj	232.8956925	33.0948917	0.0680	Hammerstein et al. (2023)	TDE-H+He
13	ZTF20abfcszi	AT2020mot	7.8063109	85.0088329	0.0690	Hammerstein et al. (2023)	TDE-H+He
14	ZTF20abgwfek	AT2020neh	230.3336852	14.0696032	0.0620	Angus et al. (2022)	TDE-H+He
15	ZTF20abnorit	AT2020ysg	171.3584535	27.4406021	0.277	Hammerstein et al. (2023)	TDE-featureless
16	ZTF20acaazkt	AT2020vdq	152.2227354	42.7167535	0.0450	This paper; J. Somalwar et al. (2023, in preparation)	Unknown
17	ZTF20achpcvt	AT2020vwl	232.6575481	26.9824432	0.0325	Hammerstein et al. (2021a)	TDE-H+He
18	ZTF20acitpfz	AT2020wey	136.3578499	61.8025699	0.0274	Arcavi et al. (2020)	TDE-H+He
19	ZTF20acnznms	AT2020yue	165.0013942	21.1127532	0.204	This paper	TDE-H?
20	ZTF20acvezvs	AT2020abri	202.3219785	19.6710235	0.178	This paper	Unknown
21	ZTF20acwytxn	AT2020acka	238.7581288	16.3045292	0.338	Hammerstein et al. (2021b)	TDE-featureless
22	ZTF21aaaokyp	AT2021axu	176.6514953	30.0854257	0.192	Hammerstein et al. (2021c)	TDE-H+He
23	ZTF21aakfqwq	AT2021crk	176.2789219	18.5403839	0.155	This paper	TDE-H+He?
24	ZTF21aanxhjv	AT2021ehb	46.9492531	40.3113468	0.0180	Yao et al. (2022a)	TDE-featureless
25	ZTF21aauuybx	AT2021jjm	219.8777384	−27.8584845	0.153	Yao et al. (2021d)	TDE-H
26	ZTF21abaxaqq	AT2021mhg	4.9287185	29.3168745	0.0730	Chu et al. (2021b)	TDE-H+He
27	ZTF21abcgnqn	AT2021nwa	238.4636684	55.5887978	0.0470	Yao et al. (2021b)	TDE-H+He
28	ZTF21abhrchb	AT2021qth	302.9121723	−21.1602187	0.0805	This paper	TDE-coronal
29	ZTF21abjrysr	AT2021sdu	17.8496154	50.5749060	0.0590	Chu et al. (2021c)	TDE-H+He
30	ZTF21abqhkjd	AT2021uqv	8.1661654	22.5489257	0.106	Yao (2021)	TDE-H+He
31	ZTF21abqtckk	AT2021utq	229.6212498	73.3587323	0.127	This paper	TDE-H
32	ZTF21abxngcz	AT2021yzv	105.2774821	40.8251799	0.286	Chu et al. (2022)	TDE-featureless
33	ZTF21acafvhf	AT2021yte	103.7697396	12.6341503	0.0530	Yao et al. (2021a)	TDE-H+He

Note. The first 16 objects were selected from ZTF-I (from 2018 October 1 to 2020 September 30) with $m_{\rm peak} < 18.75$. The last 17 objects were selected from the first year of ZTF-II (from 2020 October 1 to 2021 September 30) with $m_{g,\rm peak} < 19.1$. In the "TDE report" column, we include a refereed paper if existent.

(This table is available in machine-readable form.)

(candidates) with optical flares (see J. Somalwar et al. 2023, in preparation).

ZTF19aaniqrr/AT2019cmw (ID 7) was first reported by Perley et al. (2020b) as a peculiar transient discovered in the ZTF Bright Transient Survey (BTS; Perley et al. 2020b; Fremling et al. 2020). With an absolute magnitude of $M < -23$ mag, it was the most luminous event in the BTS sample. Its high luminosity and featureless optical spectra make it similar to events previously classified as TDE-featureless by Hammerstein et al. (2023). Detailed analysis and modeling of this object will be presented by J. Wise et al. (2023, in preparation).

ZTF20acnznms/AT2020yue (ID 19) was previously classified as a SLSN-II by Kangas et al. (2022). However, some observed properties of this object favor a TDE interpretation. The upper panel of Figure 3 shows the UV and optical light curves. The color $uvm2-r$ is 1.56 ± 0.19, 1.47 ± 0.22, and 0.37 ± 0.19 mag at $t\approx14$, 37, and 278 days, respectively. This indicates a significant increase of temperature from 37 to 278 days post peak, which is not uncommon in TDEs (Hammerstein et al. 2023), but not observed in SLSNe.

The middle panel of Figure 3 shows the three optical spectra published in Kangas et al. (2022), as well as a deep late-time optical spectrum obtained by us in 2022 November using 85 minutes of LRIS on-source time (see details in Table 7). Broad Hα emission is seen in the −13, +6, and +39 days spectra. In the +6 days LRIS spectrum, we clearly identified narrow absorption lines of the Mg II λ2800 doublet as well as a broad absorption trough around rest-frame 2660 Å, which can be attributed to blueshifted Mg II absorption. Such near-UV features have been observed in both SLSNe (Chomiuk et al. 2011; Quimby et al. 2011) and the TDE PS1-11af (Chornock et al. 2014).

At ≈595 d, the transient flux is still detected at $r=22.3\pm0.3$ in the ZTF forced photometry. No broad lines characteristic of SLSN nebular emission (such as [O I] λ6300 and [Ca II] λ7300; Nicholl et al. 2019a) are observed. The 6500–6640 Å spectrum can be decomposed into three narrow components (from the host galaxy) and a broader component that originates from the transient (see the bottom panel of Figure 3). The late-time luminosity of the broad Hα component is 1.8×10^{40} erg s^{-1}, which is a factor of 5–10 times brighter than that observed in the optically selected TDEs ASASSN-14li and ASASSN-14ae (Brown et al. 2017) but similar to the radio-selected TDE VLASS J1008 (J. Somalwar et al. 2023, in

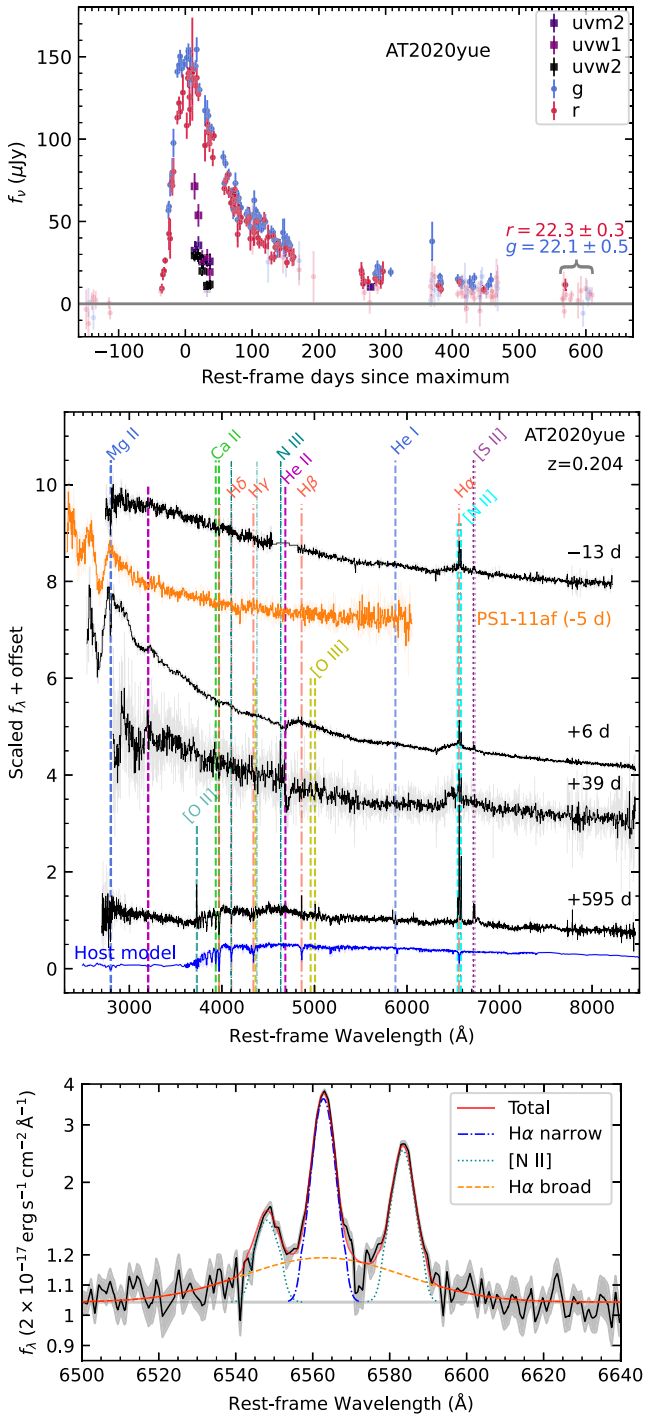

Figure 3. UV and optical properties of AT2020yue. Upper: ZTF and UV light curves of AT2020yue. Detections at $>3\sigma$ are shown with high opacity; other observations are shown in semitransparent. Middle: optical spectra of AT2020yue. For comparison, we also show the host-subtracted optical spectrum of PS1-11af (Chornock et al. 2014), and the host galaxy model derived in Section 4.2.2. Bottom: the +595 days spectrum zoomed around Hα. To highlight the broad Hα component, the *y*-axis is shown in linear-scale below 1.2, and in log scale above 1.2.

preparation). The full width half maximum of the transient Hα line decreased from ≈14,000 km s^{-1} at early time to ≈2250 km s^{-1} at ≈595 days. Such a narrowing phenomenon has been observed in a few known TDEs (Brown et al. 2017; Onori et al. 2019; Nicholl et al. 2020) and can be explained by a decrease in the optical depth of the line-emitting region (Roth & Kasen 2018).

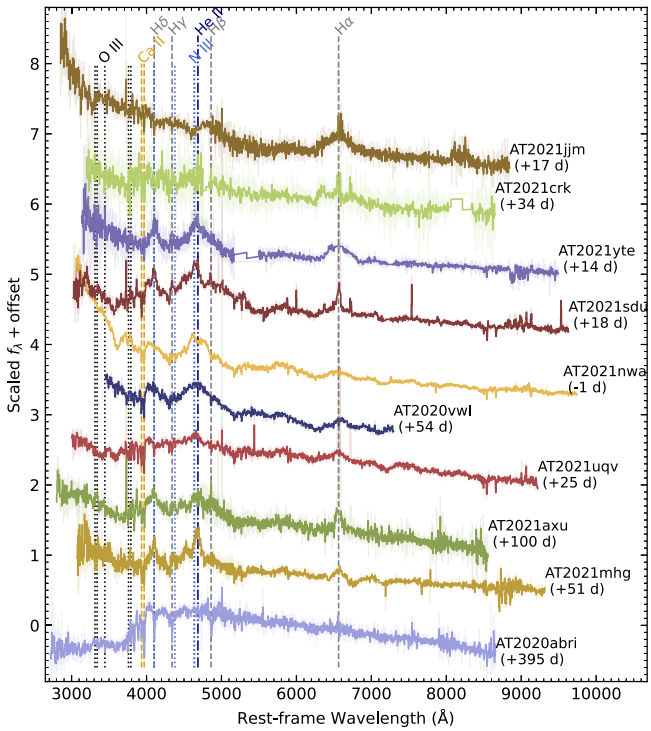

Figure 4. Optical spectra of 10 objects. Strong atmospheric telluric features have been masked. The top 9 objects show broad emission lines characteristic of spectral classes of TDE-H, TDE-H+He, and TDE-He. In a few objects, we have subtracted the blue blackbody continua and masked strong host galaxy narrow emission lines. The bottom spectrum was obtained for the host galaxy of AT2020abri.

ZTF20acvezvs/AT2020abri (ID 20) has no optical spectrum obtained during the optical flare. A post-flare spectrum clearly shows host galaxy absorption lines at $z = 0.178$ (see Figure 4). Following the procedures adopted by Sazonov et al. (2021), we measure the equivalent width (EW) of the Hα emission line and the Lick Hδ_A index, resulting in EW(H α_{em}) = 3.22 Å, and Lick H$\delta_{A,abs}$ = 5.52 Å. We consider this object to be a probable TDE since (i) its color remains blue ($g - r \approx -0.2$ mag) for ∼200 days (see Figure 2), and the lack of cooling makes it different from most SNe; (ii) the relatively strong Hδ absorption and weak Hα emission suggest that the host is a post-starburst galaxy, which is overrepresented in previous samples of TDE host galaxies (French et al. 2016; Law-Smith et al. 2017; French et al. 2020; Hammerstein et al. 2021d).

ZTF21aakfqwq/AT2021crk (ID 23) has a DBSP spectrum obtained during the optical flare, which is not of high signal-to-noise ratio (S/N; see Figure 4). A broad emission line at Hα is clearly present (with the red wing slightly affected by telluric absorptions), while the He II wavelength region is affected by the DBSP CCD malfunction. Therefore, we tentatively assign a spectral subtype of TDE-H+He? for this object.

ZTF21abhrchb/AT2021qth (ID 28) was missed by real-time selection with optical surveys, but was later revealed to be a TDE based on an X-ray detection at $L_X \sim 6 \times 10^{42}$ erg s^{-1} from SRG/eROSITA (private communication). X-ray data of this object will be presented as part of a sample of SRG-selected TDEs with strong optical flares by M. Gilfanov et al. (2023, in preparation). Such a high X-ray luminosity is not theoretically expected in interaction-powered SNe (see Figure 3 of Margalit et al. 2022), and $> \times 10$ brighter than the peak of the most X-ray luminous known SN IIn (see, e.g., Figure 7 of

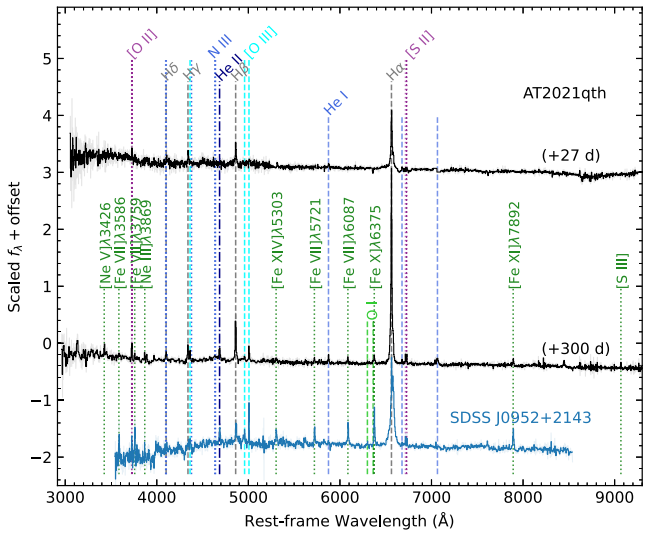

Figure 5. Optical spectra of AT2021qth, compared with the SDSS spectrum of the prototype extreme coronal line emitter SDSS J0952+2143 (Komossa et al. 2008; Palaversa et al. 2016).

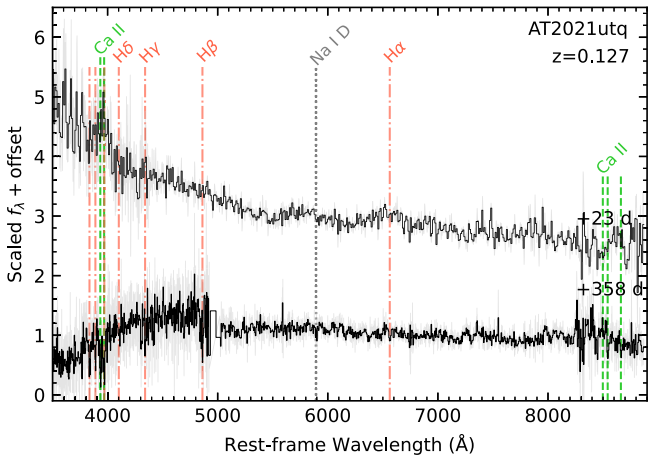

Figure 6. Optical spectra of AT2021utq. The late-time DBSP spectrum shows host galaxy absorption lines (Na I, Ca II, Balmer series) at $z = 0.127$. At this redshift, the early time spectrum reported by Burke et al. (2021) exhibits a broad emission line around Hα, making it consistent with the TDE-H spectral class.

Yao et al. 2022b). Figure 5 shows that its late-time optical spectrum exhibits highly ionized narrow emission lines of [Ne III], [Ne V], [Fe VII], [Fe X], [Fe XI], and [Fe XIV]—reminiscent of the known class of extreme coronal line emitters (Komossa et al. 2008; Somalwar et al. 2022).

ZTF21abqtckk/AT2021utq (ID 31) was previously classified as a variable star on TNS based on the fact that its parallax was reported by Gaia Data Release 2 (DR2) and that the distance was estimated by Bailer-Jones et al. (2018) to be ∼1 kpc (Burke et al. 2021). However, both the Gaia parallax ($\varpi = -0.91 \pm 1.51$ mas) and the distance estimate ($1.16^{+0.81}_{-0.50}$ kpc) have large uncertainties. Moreover, a post-flare optical spectrum reveals host galaxy absorption lines at $z = 0.127$ (see Figure 6). At this redshift, the TNS spectrum exhibits a board emission line at Hα, suggesting a spectral class of TDE-H.

The TDE classifications of the remaining 10 objects have been previously reported to TNS by the ZTF group. Their optical spectra are shown in Figure 4 for objects with broad emission lines, and in Figure 7 for two objects in the TDE-featureless spectral class.

We note that, although TDEs can evolve and change spectroscopic subtypes (Nicholl et al. 2019c; van Velzen et al. 2020; Charalampopoulos et al. 2022), a precise labeling of the subtype is not important for this work.

3. Light-curve Characterization

In this section, we aim to systematically estimate the peak-light properties and light-curve evolution timescales of the 33 TDEs. We outline the procedures of the fitting routine in Section 3.1, describe the choice of the light-curve model in Section 3.2, and summarize the results in Section 3.3.

3.1. The Fitting Routine

Model fitting was performed using the Markov Chain Monte Carlo (MCMC) approach with the `emcee` sampler (Foreman-Mackey et al. 2013). For each TDE (at redshift z) and each observation i, the input data are t_i (rest-frame days relative to the visually determined light-curve maximum), L_i, σ_i (Galactic extinction-corrected luminosity and its uncertainty in the observed band), and ν_i (rest-frame effective frequency of the observed band). We assume negligible host galaxy extinction.

Following Yao et al. (2019), we add a constant additional variance σ_0^2 to each of the measurement variance σ_i^2 to account for systematic uncertainties. We use 100 walkers and N steps, where N is typically 1000–3000. We visually inspect the walker values as a function of step to ensure convergence. The posterior distribution is obtained after discarding the first $N - 500$ steps.

3.2. The Light-curve Model

3.2.1. The SED Shape

It has been shown that the UV and optical emission of TDEs can be described with a thermal blackbody (Gezari 2021). Therefore, we assume that the UV and optical spectrum follows a blackbody $B_\nu(T_{\rm bb})$. Our goal is to determine the blackbody parameters (temperature $T_{\rm bb}$, radius $R_{\rm bb}$, and luminosity $L_{\rm bb}$) at maximum light.

Since the majority of known TDEs show little temperature evolution (van Velzen et al. 2020), we assume the temperature is fixed to that near peak. However, this assumption is not appropriate for a few TDEs in our sample (IDs 2, 5, 7, 8, 10, 13, 14, 18, 21, 24, 27) with significant post-peak $uvw2 - r$ color change. Since our goal is to constrain the peak-light blackbody parameters, we excluded late-time UVOT data for these objects.[29]

3.2.2. The Rise Function

Following van Velzen et al. (2021), we first model the light curve at $t < 100$ days with a Gaussian rise and an exponential decay:

$$L_\nu(t) = A_\nu \times \begin{cases} e^{(t-t_{\rm peak})^2/(2\sigma_{\rm rise}^2)} & t \leqslant t_{\rm peak} \\ e^{-(t-t_{\rm peak})/\tau_{\rm decay}} & t > t_{\rm peak} \end{cases}; \quad \text{(1a)}$$

[29] We removed UVOT data at $t \gtrsim t_{\rm c/h}$, where $t_{\rm c/h}$ is the time when clear evidence of post-peak cooling or heating is observed. We chose $t_{\rm c/h} \in (5, 100)$ days for each of the 10 objects by visually inspecting their multiband light curves.

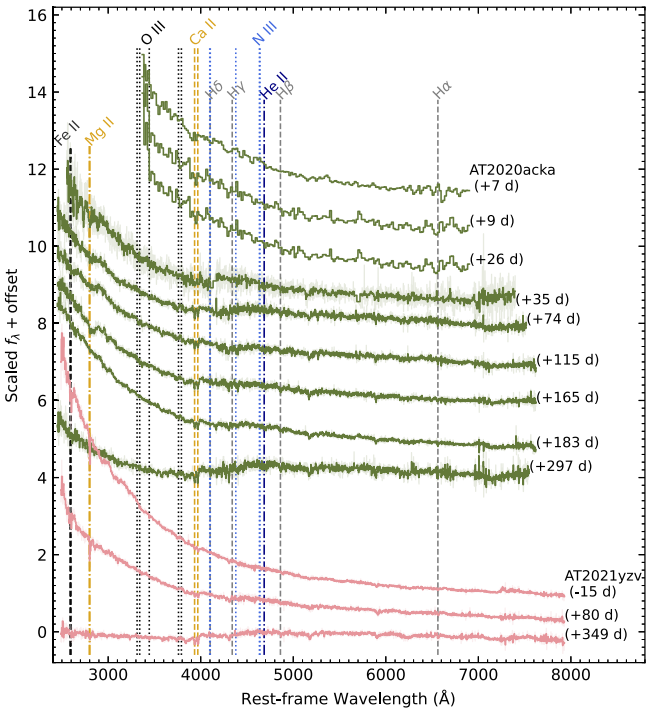

Figure 7. Optical spectra of two TDEs that belong to the TDE-featureless subclass. We highlight the fact that the rest-frame Hα region is covered by our spectra, and no discernible emission lines are present throughout the spectral evolution.

$$A_\nu = L_{\nu_0\,\mathrm{peak}} \frac{B_\nu(T_0)}{B_{\nu_0}(T_0)}. \tag{1b}$$

Here, $L_{\nu_0\,\mathrm{peak}}$ is the rest-frame g-band ($\nu_0 = 6.3 \times 10^{14}$ Hz) peak luminosity, and t_{peak} is the epoch of rest-frame g-band maximum.

A Gaussian function is generally a good model when the data sampling is sparse on the rise, since it reduces the model complexity by imposing strong assumptions on the shape of the light-curve profile. However, it cannot describe a rise where the flux increase rate decreases as a function of time (e.g., see Figure 8). Therefore, for objects with good sampling on the rise,[30] we also fit the rise with a power-law function:

$$L_\nu(t) = A_\nu \times \begin{cases} 0 & t \leqslant t_{\mathrm{fl}} \\ \dfrac{(t - t_{\mathrm{fl}})^n}{(t_{\mathrm{peak}} - t_{\mathrm{fl}})^n} & t_{\mathrm{fl}} < t \leqslant t_{\mathrm{peak}} \end{cases} \tag{2}$$

where t_{fl} is the first-light epoch, and n is the rise power-law index. We consider the power-law rise model to be superior to the Gaussian rise model if the best-fit σ_0 is smaller, and the 68% confidence region of n is <0.5. The adopted rise function for each TDE is given in the "Model" column of Table 4.

3.2.3. The Decline Function

Having decided on the rise function, we fit the light curve within $t < 365$ d with six types of decline functions:

1. an exponential decline (model `d1`; Equation (1a)),
2. a power-law decline (model `d2`)

$$L_\nu(t) = A_\nu \left(\frac{t - t_{\mathrm{peak}} + t_0}{t_0} \right)^p \quad t > t_{\mathrm{peak}}, \tag{3}$$

3. an exponential decline followed by a late-time plateau (model `d3`),
4. a power-law decline followed by a late-time plateau (model `d4`),
5. an exponential decline with a secondary peak on top of that (model `d5`),
6. a power-law decline with a secondary peak on top of that (model `d6`).

In functions `d5` and `d6`, we assume that the secondary peak has a Gaussian rise and an exponential decline. We compare the Bayesian information criterion (BIC) of the six model fits and choose the one with the smallest value of BIC. The adopted decline function for each TDE is given in the "Model" column of Table 4.

3.3. The Fitting Results

Figure 9 shows the fitting results. The light-curve properties obtained with the best-fit models are provided in Table 4, where t_{peak} is the peak-light epoch, T_{bb}, L_{bb}, and R_{bb} are the blackbody parameters at peak; L_g is the rest-frame g-band luminosity at peak (corrected for Galactic extinction). Following conventions of transient studies (Yao et al. 2022b; Ho et al. 2023), we characterize the light-curve evolution speed by calculating the rest-frame duration it takes for a TDE to rise from half-max to max ($t_{1/2,\mathrm{rise}}$) and to decline from max to half-max ($t_{1/2,\mathrm{decline}}$). The rest-frame duration above half-max light is $t_{1/2} \equiv t_{1/2,\mathrm{rise}} + t_{1/2,\mathrm{decline}}$.

4. Host Galaxy Analysis

4.1. Observation

4.1.1. Photometry

For the TDE host galaxies, we retrieved science-ready coadded images from the Galaxy Evolution Explorer (GALEX) general release 6/7 (Martin et al. 2005), the Sloan Digital Sky Survey data release 9 (SDSS DR9; Ahn et al. 2012), the PS1, the Two Micron All Sky Survey (2MASS; Skrutskie et al. 2006), and the unWISE archive (Lang 2014). We measured the brightness of the host galaxies using the `Lambda Adaptive Multi-Band Deblending Algorithm in R` (`LAMBDAR`; Wright et al. 2016) and the methods described in Schulze et al. (2021).

We note that some fields were observed more than once with GALEX, while the Schulze et al. (2021) pipeline only utilizes the deepest GALEX exposure. Therefore, in two objects (IDs 8, 28), to make the most of GALEX observations, we supplemented the `LAMBDAR` measurements with GALEX photometry extracted by `gPhoton` (Million et al. 2016). We adopted an aperture of 10″ and 5″ for the host galaxies of AT2019dsg and AT2021qth, respectively. Appendix A presents the photometry in different bands.

4.1.2. ESI Spectroscopy

To measure the velocity dispersion of TDE host galaxies, we obtained medium-resolution spectra using the Echellette Spectrograph and Imager (ESI; Sheinis et al. 2002) on the

[30] Here, *good sampling* is defined as follows. For each object, we select data within $[t_{\mathrm{peak}} - 2\sigma_{\mathrm{rise}}, t_{\mathrm{peak}} + \sigma_{\mathrm{rise}}]$, where t_{peak} and σ_{rise} are best-fit model parameters from Equation (1(a)). We require that the maximum time separation in consecutive pairs of observations is less than σ_{rise}.

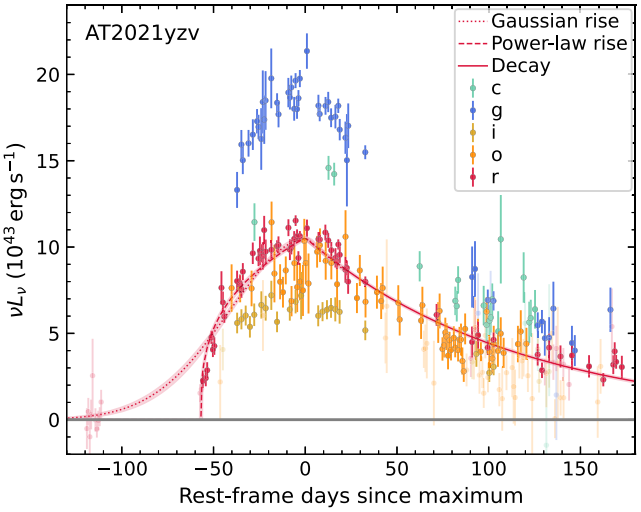

Figure 8. ZTF and ATLAS light curves of AT2021yzv, overplotted with the best-fit models in the ZTF r band. Detections at $>4\sigma$ are shown with high opacity. A power-law function provides a better description for the rise profile.

Keck II telescope. In all observations, we used the Echelle mode. Spectra were obtained for the host galaxies of 17 TDEs (see Table 8 in Appendix A for details). A slit width of 0.″3, 0.″5, and 0.″75 gives an instrumental broadening of $\sigma_{\rm inst} = 9.5$, 15.8, and 23.7 km s^{-1}. We reduced the ESI spectra with the `makee` pipeline.[31] We extracted the spectrum using a radius of $r_{\rm extract}$, which was implemented by specifying the `hw` and `uop` parameters in `makee`. For most objects, $r_{\rm extract}$ was chosen to match the half-light radius (see $r_{1/2}$ in Table 5). For a few faint host galaxies, $r_{\rm extract}$ was chosen to enclose a larger aperture to maximize the S/N.

4.2. Analysis

4.2.1. ESI Spectral Fitting

The galaxy central velocity dispersion σ_* (i.e., the intensity weighted mean of the root-mean-square of the line-of-sight stellar velocity) is known to be correlated with the central massive BH mass (Merritt & Ferrarese 2001; Pinkney et al. 2003; Gültekin et al. 2009; Kormendy & Ho 2013). Following previous works (Wevers et al. 2017; Somalwar et al. 2022), we measured σ_* with the penalized pixel-fitting (`pPXF`) software (Cappellari & Emsellem 2004; Cappellari 2017), which fits the ESI absorption line spectrum by convolving a template stellar spectral library with Gauss-Hermite functions.

We used the ELODIE v3.1 high-resolution ($R = 42{,}000$) library (Prugniel & Soubiran 2001; Prugniel et al. 2007). For all ESI spectra, we fit the rest-frame wavelength range from 5030 to 5600 Å. Prominent galaxy absorption lines[32] of Mg I, Fe I, Ca I, and Cr I in this wavelength range are shown in Figure 10. We masked wavelength ranges of common galaxy emission lines, hydrogen Balmer lines, telluric regions, an instrument artifact feature at observer-frame ∼4510 Å, and the Na I D doublet at $z = 0$ if Galactic absorption is strong.

Following previous works (Wevers et al. 2017, 2019; French et al. 2020), we performed 1000 Monte Carlo (MC) simulations to robustly determine σ_*. In each MC simulation, the observed spectrum was resampled within its error spectrum and refitted with `pPXF`. By visually examining results of the simulations, we confirmed that the distributions of the velocity dispersion are well-behaved (i.e., not double-peaked or skewed). We took the median of the distribution as the velocity dispersion, and the difference between the 84th/16th percentiles as the uncertainty. The best-fit spectra and the measured σ_* are shown in Figure 10.

4.2.2. SED Fitting

We modeled the photometric spectral energy distribution (SED) of host galaxies with the software package `prospector` version 1.1 (Johnson et al. 2021). `prospector` uses the `Flexible Stellar Population Synthesis` (`FSPS`) code (Conroy et al. 2009) to generate the underlying physical model and `python-fsps` (Foreman-Mackey et al. 2014) to interface with `FSPS` in Python. We assumed a Chabrier initial mass function (Chabrier 2003) and approximated the star formation history (SFH) by a delayed exponentially declining function. The model was attenuated with the Calzetti et al. (2000) model. The fitted parameters are presented in columns (3)–(8) of Table 5, where $M_{\rm gal}$ is the host galaxy total stellar mass; ${}^{0,0}u-r$ is the Galactic extinction-corrected, synthetic rest-frame $u-r$ color; $\tau_{\rm SFH}$ is the characteristic e-folding timescale of the SFH; $t_{\rm age}$ is the stellar age; Z is the metallicity; and $E(B-V)_{\rm h}$ is the host galaxy extinction.

A fraction of our TDE host galaxies have been analyzed with similar approaches in the literature (Ramsden et al. 2022; Hammerstein et al. 2023). In Appendix C, we show that our estimates of $M_{\rm gal}$ and ${}^{0,0}u-r$ are mostly consistent with previous results, and point out possible reasons for the differences. The best-fit galaxy SEDs are also shown in Appendix C.

4.2.3. Black Hole Mass Estimates

Here, we estimate the BH mass $M_{\rm BH}$ of our TDE sample using host galaxy scaling relations.

For objects with σ_* measurements, we use the (Kormendy & Ho 2013, Equation (3)) $M_{\rm BH}$–σ_* relation:

$$\log M_{\rm BH,9} = -(0.509 \pm 0.049) + (4.384 \pm 0.287) \times \log\left(\frac{\sigma_*}{200\ {\rm km\ s^{-1}}}\right);\ \text{intrinsic scatter} = 0.29, \quad (4)$$

where $M_{\rm BH,9} \equiv M_{\rm BH}/10^9\,M_\odot$. In addition to the 17 objects with ESI spectra (Table 8), we adopt $\sigma_* = 69 \pm 2$ km s^{-1} for AT2019qiz (Nicholl et al. 2020), and $\sigma_* = 40 \pm 6$ km s^{-1} for AT2020neh (Angus et al. 2022).

Figure 11 shows the inferred $M_{\rm BH}$ versus $M_{\rm gal}$ (derived from galaxy SED fitting; Section 4.2.2) of these 19 objects. We fit a linear relation to these objects:

$$\log M_{\rm BH,9} = -(1.75 \pm 0.13) + (1.73 \pm 0.23) \times \log\left(\frac{M_{\rm gal}}{3 \times 10^{10}\,M_\odot}\right);\ \text{intrinsic scatter} = 0.17, \quad (5)$$

which is shown as the solid red line. For reference, we also show empirical relations from the literature. Reines & Volonteri (2015) adopt dynamical BH masses for inactive

[31] https://www2.keck.hawaii.edu/inst/esi/makee.html

[32] We take the strong lines table in the National Institute of Standards and Technology atomic database.

Table 4
Light-curve Properties and Survey Efficiencies

ID	IAU Name	Model	$t_{\rm peak}$ (MJD)	log $T_{\rm bb}$ (K)	logL_g (erg s^{-1})	log $L_{\rm bb}$ (erg s^{-1})	log $R_{\rm bb}$ (cm)	$t_{1/2,\rm rise}$ (days)	$t_{1/2,\rm decline}$ (days)	$D_{\rm max,t}$ (Mpc)	$z_{\rm max,t}$	$f_{\rm loss}$
1	AT2018iih	r2+d2	$58451.13^{+2.78}_{-2.20}$	4.22	44.11	44.59	15.43	$31.0^{+2.5}_{-1.5}$	$86.5^{+3.3}_{-5.0}$	1501	0.291	0.525
2	AT2018jbv	r1+d2	$58470.36^{+0.00}_{-0.00}$	4.50	44.23	45.33	15.24	$34.4^{+2.1}_{-1.4}$	$65.9^{+2.3}_{-1.7}$	2052	0.381	0.328
3	AT2018lna	r1+d1	$58507.31^{+1.20}_{-0.95}$	4.49	43.21	44.27	14.73	$15.5^{+1.3}_{-1.0}$	$30.2^{+1.3}_{-1.1}$	488	0.106	0.241
4	AT2019baf	r2+d6	$58514.16^{+0.82}_{-0.78}$	4.10	43.52	43.81	15.28	$23.2^{+0.9}_{-1.0}$	$27.6^{+0.6}_{-0.9}$	668	0.141	0.475
5	AT2019azh	r2+d2	$58561.39^{+1.05}_{-0.77}$	4.46	43.30	44.31	14.80	$24.7^{+1.3}_{-1.0}$	$44.1^{+1.1}_{-0.9}$	547	0.118	0.652
6	AT2019bhf	r1+d2	$58544.78^{+1.10}_{-1.34}$	4.14	43.46	43.81	15.20	$9.9^{+0.7}_{-0.9}$	$29.1^{+1.9}_{-1.4}$	630	0.134	0.207
7	AT2019cmw	r2+d2	$58588.82^{+0.00}_{-0.00}$	4.34	44.68	45.41	15.60	$14.0^{+0.3}_{-0.3}$	$28.9^{+0.7}_{-0.5}$	3714	0.626	0.288
8	AT2019dsg	r1+d1	$58606.97^{+3.51}_{-3.22}$	4.41	43.18	44.05	14.79	$19.7^{+2.3}_{-2.0}$	$43.1^{+1.0}_{-1.1}$	465	0.101	0.526
9	AT2019ehz	r2+d6	$58618.69^{+0.70}_{-0.51}$	4.29	43.28	43.90	14.94	$15.7^{+0.7}_{-0.8}$	$28.0^{+0.0}_{-1.0}$	521	0.112	0.380
10	AT2019qiz	r1+d4	$58766.50^{+0.25}_{-0.26}$	4.23	42.90	43.40	14.81	$11.6^{+0.3}_{-0.3}$	$17.9^{+0.7}_{-0.8}$	322	0.0714	0.545
11	AT2019vcb	r1+d1	$58819.83^{+1.08}_{-0.89}$	4.11	43.35	43.65	15.19	$13.6^{+1.1}_{-0.8}$	$24.6^{+0.4}_{-0.4}$	546	0.117	0.309
12	AT2020pj	r1+d2	$58866.42^{+0.58}_{-0.55}$	4.10	42.95	43.24	14.99	$12.4^{+0.7}_{-0.5}$	$17.2^{+1.3}_{-1.1}$	335	0.0742	0.158
13	AT2020mot	r1+d4	$59082.04^{+1.24}_{-1.30}$	4.29	43.22	43.84	14.92	$42.6^{+1.3}_{-1.6}$	$46.1^{+1.9}_{-2.1}$	485	0.105	0.515
14	AT2020neh	r1+d1	$59030.93^{+0.53}_{-0.39}$	4.19	43.26	43.70	15.04	$6.4^{+0.4}_{-0.4}$	$16.4^{+0.6}_{-0.6}$	501	0.108	0.269
15	AT2020ysg	r1+d2	$59094.32^{+3.30}_{-3.03}$	4.37	44.24	45.04	15.35	$24.0^{+2.1}_{-1.5}$	$72.5^{+2.1}_{-3.3}$	1963	0.367	0.463
16	AT2020vdq	r1+d2	$59113.09^{+1.00}_{-0.93}$	4.16	42.62	42.99	14.76	$11.9^{+1.7}_{-1.3}$	$23.3^{+1.5}_{-1.7}$	227	0.0511	0.210
17	AT2020vwl	r1+d4	$59166.88^{+1.17}_{-1.14}$	4.30	43.13	43.77	14.86	$22.2^{+0.8}_{-0.7}$	$27.4^{+1.9}_{-1.7}$	515	0.111	0.623
18	AT2020wey	r1+d5	$59155.84^{+0.19}_{-0.20}$	4.32	42.47	43.15	14.51	$13.9^{+0.4}_{-0.4}$	$5.2^{+0.2}_{-0.2}$	228	0.0514	0.302
19	AT2020yue	r1+d4	$59179.44^{+1.25}_{-1.12}$	4.06	44.00	44.24	15.57	$19.5^{+1.0}_{-0.9}$	$62.8^{+2.0}_{-1.9}$	1399	0.274	0.465
20	AT2020abri	r2+d3	$59208.56^{+0.83}_{-0.80}$	4.10	43.66	43.95	15.35	$16.7^{+1.2}_{-0.9}$	$31.7^{+0.7}_{-0.8}$	948	0.194	0.261
21	AT2020acka	r1+d5	$59217.15^{+1.38}_{-1.14}$	4.45	44.47	45.44	15.39	$26.9^{+1.6}_{-1.8}$	$28.8^{+0.7}_{-0.5}$	3629	0.614	0.514
22	AT2021axu	r1+d2	$59252.50^{+0.55}_{-0.50}$	4.58	43.75	45.05	14.93	$23.9^{+0.5}_{-0.6}$	$33.4^{+0.9}_{-1.0}$	1253	0.249	0.368
23	AT2021crk	r1+d2	$59273.90^{+0.53}_{-0.52}$	4.30	43.50	44.14	15.05	$10.2^{+0.7}_{-0.4}$	$20.9^{+1.1}_{-1.1}$	831	0.173	0.216
24	AT2021ehb	r1+d3	$59314.51^{+2.78}_{-1.90}$	4.44	42.58	43.54	14.46	$23.7^{+1.9}_{-1.4}$	$50.5^{+3.6}_{-3.8}$	265	0.0593	0.661
25	AT2021jjm	r1+d1	$59327.68^{+0.99}_{-0.93}$	4.17	43.59	43.99	15.23	$9.1^{+0.7}_{-0.7}$	$29.1^{+2.6}_{-1.7}$	893	0.184	0.304
26	AT2021mhg	r1+d4	$59370.28^{+0.89}_{-0.85}$	4.49	43.22	44.28	14.74	$17.2^{+0.7}_{-0.7}$	$14.7^{+1.1}_{-1.0}$	595	0.127	0.399
27	AT2021nwa	r1+d3	$59402.51^{+0.64}_{-0.68}$	4.51	42.68	43.81	14.45	$27.1^{+0.6}_{-0.8}$	$76.2^{+1.9}_{-1.6}$	301	0.0669	0.483
28	AT2021qth	r2+d4	$59401.88^{+1.26}_{-1.26}$	3.96	43.14	43.30	15.30	$15.8^{+1.2}_{-1.3}$	$39.1^{+1.3}_{-2.0}$	481	0.104	0.374
29	AT2021sdu	r1+d3	$59419.36^{+0.33}_{-0.36}$	4.30	43.09	43.73	14.84	$12.2^{+0.4}_{-0.4}$	$11.0^{+0.3}_{-0.4}$	488	0.106	0.340
30	AT2021uqv	r1+d5	$59446.39^{+0.66}_{-0.63}$	4.29	43.15	43.77	14.87	$14.9^{+0.7}_{-0.7}$	$36.0^{+2.2}_{-2.0}$	525	0.113	0.251
31	AT2021utq	r1+d6	$59457.51^{+0.83}_{-0.85}$	4.39	43.39	44.22	14.91	$14.6^{+0.6}_{-0.6}$	$43.4^{+5.8}_{-4.3}$	736	0.155	0.390
32	AT2021yzv	r2+d2	$59511.50^{+1.35}_{-1.38}$	4.43	44.07	45.01	15.21	$51.8^{+1.4}_{-1.2}$	$69.9^{+2.6}_{-2.6}$	1920	0.360	0.456
33	AT2021yte	r1+d3	$59484.99^{+0.59}_{-0.60}$	4.29	42.90	43.52	14.75	$18.4^{+0.5}_{-0.6}$	$23.7^{+0.7}_{-0.7}$	385	0.0847	0.413

Note. Column (3) indicates the light-curve rise and decline functional forms of the adopted model. r1: Gaussian rise. r2: power-law rise. See Section 3.2.3 for the meaning of the six decline models. Columns (4)–(10) are light-curve properties (see Section 3.3 for definitions). Columns (11)–(13) are parameters relevant to the survey efficiencies (see Section 5 for definitions).

(This table is available in machine-readable form.)

galaxies (Kormendy & Ho 2013), and use $M_{\rm BH}$ derived from the width and luminosity of the Hα broad line for AGN. Greene et al. (2020) adopt dynamical BH masses provided by Kormendy & Ho (2013) and recent literatures (see details in Section 8.2 of Greene et al. 2020). We use Equation (5) to infer the $M_{\rm BH}$ for the remaining 14 objects without σ_* measurements.

The inferred values of $M_{\rm BH}$ are shown in Table 5. The majority of events (25/33) in our sample are hosted by BHs with $M_{\rm BH} \in (10^5, 10^7) M_\odot$. We computed the Eddington ratio of the UV and optical emitting component $\lambda_{\rm Edd} \equiv L_{\rm bb}/L_{\rm Edd}$, where $L_{\rm Edd} \equiv (M_{\rm BH}/M_\odot) \times 1.25 \times 10^{38}$ erg s^{-1}.

Among our sample, AT2020acka (ID 21) has the greatest value of $M_{\rm BH}$ at $10^{8.23\pm0.40}\,M_\odot$. For a Schwarzschild BH, the maximum mass at which a star of mass m_* (in $M_\odot$) and radius r_* (in $R_\odot$) can be tidally disrupted outside the horizon is given by

$$M_{\rm Hills}(m_*) = 1.1 \times 10^8\, M_\odot m_*^{-1/2} r_*^{3/2}. \quad (6)$$

Assuming $r_* \sim m_*^{0.6}$ for $m_* > 1$ (Demircan & Kahraman 1991), $M_{\rm Hills} = 10^{8.4}\, M_\odot (m_*/10)^{0.4}$. Therefore, the $M_{\rm BH}$ of AT2020acka is still below $M_{\rm Hills}$ of a massive star ($m_* \gtrsim 4$). The disruption of a low-mass main-sequence star requires a rapid BH spin (Kesden 2012). Given that the $t_{\rm age}$ of its host galaxy is not young, the relatively large $M_{\rm BH}$ can also be explained by the disruption of evolved stars (MacLeod et al. 2012, 2013).

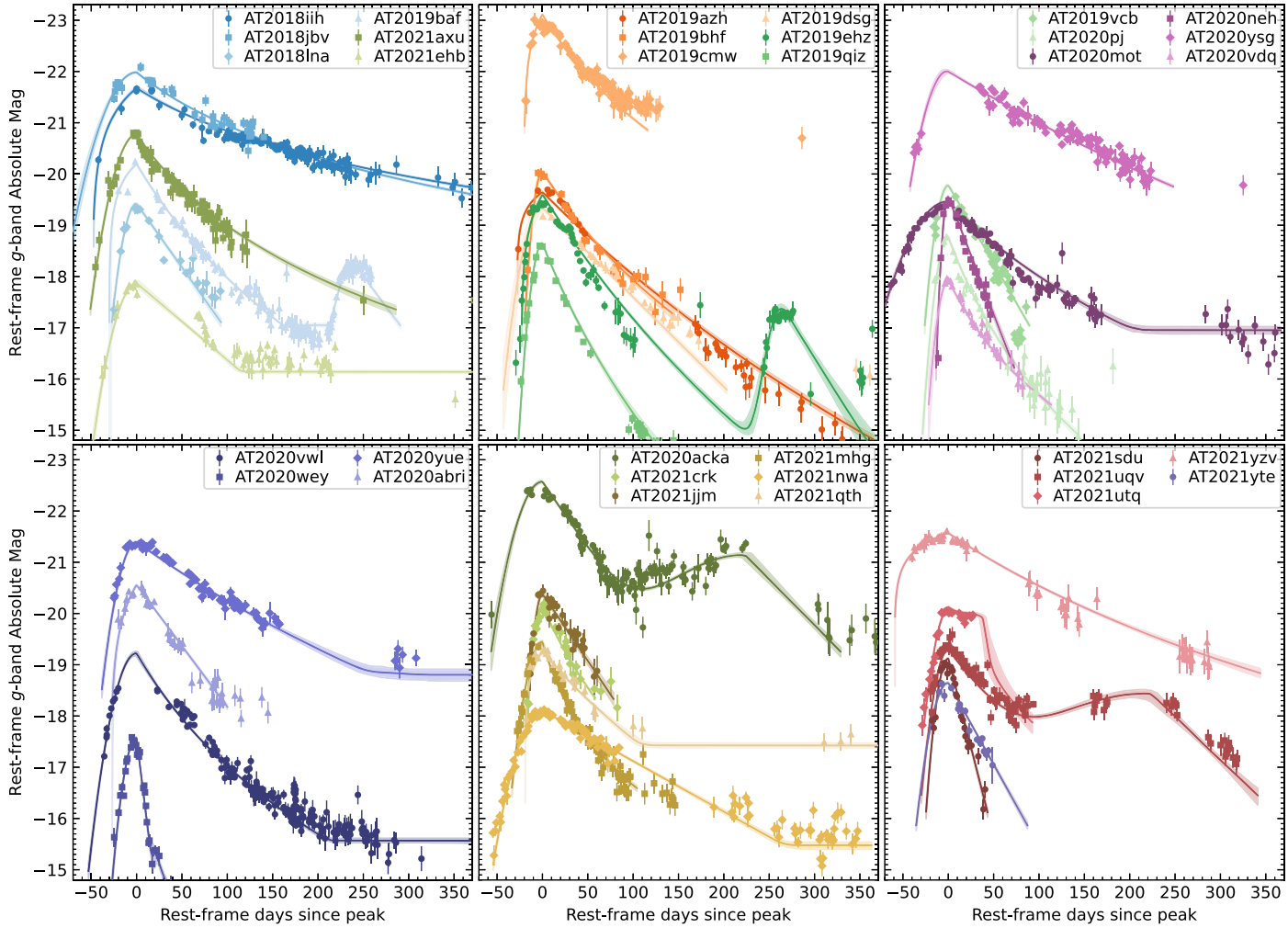

Figure 9. Rest-frame g-band light curves of the 33 TDEs in our sample. The solid lines show the best-fit models.

5. Survey Efficiency

For an ideal survey that scans the entire sky to a given flux limit, the volumetric rate of a given type of transient can be estimated using the following (Schmidt 1968):

$$\mathcal{R} = \sum_{i=1}^{N} \mathcal{R}_i = \sum_{i=1}^{N} \frac{1}{T_{\mathrm{span},i}/(1+z_i)} \frac{1}{V_{\mathrm{max},i}}, \tag{7}$$

where $T_{\mathrm{span},i}/(1+z_i)$ is the rest-frame duration of the experiment within which the ith transient is selected, N is the number of transients that have passed the flux limit, the maximum volume $V_{\mathrm{max},i} \equiv \frac{4\pi}{3} D_{\mathrm{max},i}^3$, and D_{max} is the maximum luminosity distance (see Section 5.2). In this work, $N = 33$. For the 16 ZTF-I TDEs, $T_{\mathrm{span},i} = 2$ yr (from 2018 October 1 to 2020 September 30); while for the 17 ZTF-II TDEs, $T_{\mathrm{span},i} = 1$ yr (from 2020 October 1 to 2021 September 30).

5.1. Loss Function

For a realistic sky survey, V_{max} in Equation (7) needs to be replaced by the effective volume $\mathcal{V}_{\mathrm{max}} = V_{\mathrm{max}} f_{\mathrm{loss}}$ (Perley et al. 2020b). Here, the loss factor f_{loss} takes into account the facts that the survey coverage is not all-sky, that the Galactic extinction reduces the survey volume, that the limiting magnitude of observations is not constant (it depends strongly on the moon phase, weather, and airmass), and that fast-evolving TDEs with fainter peak magnitudes are easier to be missed.

To estimate f_{loss}, we took the observation history of ZTF. We obtained the limiting magnitude for each observation (with a certain field ID and MJD) from the exposure table of ZTF DR14.[33] For each TDE, using the light-curve model obtained in Section 3.3, we simulated fake ZTF observations by inserting 10^5 light curves uniformly across all sky and $T_{\mathrm{span},i}$. We then applied the cuts outlined in Section 2.2 to compute the fraction of observations that would have passed our selection criteria. The values of f_{loss} are given in the last column of Table 4.

5.2. Maximum Volume

If the TDE candidate selection only depends on transient photometric properties, then $D_{\mathrm{max}} = D_{\mathrm{max,t}}$, where $D_{\mathrm{max,t}}$ is the distance out to which a transient can be detected above the flux limit of our experiments (i.e., $m_{\mathrm{peak}} < 18.75$ for ZTF-I TDEs, and $m_{g,\mathrm{peak}} < 19.1$ for ZTF-II TDEs). $D_{\mathrm{max,t}}$ can be computed using the redshifts and the best-fit values of T_{bb}, L_{bb}

[33] Accessible at https://irsa.ipac.caltech.edu/data/ZTF/docs/ztf_metadata_latest.db.

Table 5
Host Galaxy Properties

ID	IAU name	log $M_{\rm gal}$ ($M_\odot$)	$^{0.0}u-r$ (mag)	$\tau_{\rm SFH}$ (Gyr)	$t_{\rm age}$ (Gyr)	log$Z$ ($Z_\odot$)	$E(B-V)_{\rm h}$ (mag)	log $M_{\rm BH}$ ($M_\odot$)	σ_* (km s^{-1})	$r_{1/2}$ ($''$)	$z_{\rm max,h}$
1	AT2018iih	$10.69^{+0.12}_{-0.16}$	$2.17^{+0.09}_{-0.13}$	$0.33^{+0.54}_{-0.19}$	$8.59^{+2.81}_{-3.63}$	$-1.02^{+0.43}_{-0.65}$	$0.13^{+0.10}_{-0.09}$	7.93 ± 0.35	148.64 ± 14.42	1.5	0.60
2	AT2018jbv	$10.20^{+0.17}_{-0.19}$	$1.98^{+0.18}_{-0.19}$	$0.71^{+1.29}_{-0.50}$	$7.87^{+3.38}_{-3.73}$	$-1.27^{+0.61}_{-0.51}$	$0.15^{+0.08}_{-0.09}$	6.77 ± 0.40	⋯	1.0	0.52
3	AT2018lna	$9.50^{+0.12}_{-0.17}$	$1.84^{+0.11}_{-0.19}$	$0.37^{+0.60}_{-0.22}$	$8.33^{+2.66}_{-3.29}$	$-1.43^{+0.43}_{-0.39}$	$0.06^{+0.04}_{-0.04}$	5.56 ± 0.51	⋯	1.4	0.26
4	AT2019baf	$10.27^{+0.04}_{-0.05}$	$1.75^{+0.05}_{-0.04}$	$3.23^{+0.76}_{-0.95}$	$10.57^{+1.35}_{-2.40}$	$-0.54^{+0.27}_{-0.39}$	$0.17^{+0.04}_{-0.04}$	6.89 ± 0.24	⋯	1.8	0.43
5	AT2019azh	$9.88^{+0.03}_{-0.03}$	$1.76^{+0.01}_{-0.01}$	$0.29^{+0.05}_{-0.04}$	$2.26^{+0.28}_{-0.24}$	$-0.63^{+0.10}_{-0.10}$	$0.06^{+0.01}_{-0.01}$	6.44 ± 0.33	67.99 ± 2.03	4.0	0.41
6	AT2019bhf	$10.39^{+0.05}_{-0.06}$	$1.96^{+0.04}_{-0.04}$	$1.74^{+0.35}_{-0.47}$	$10.45^{+1.49}_{-2.29}$	$-0.95^{+0.42}_{-0.44}$	$0.12^{+0.05}_{-0.05}$	7.10 ± 0.24	⋯	1.7	0.45
7	AT2019cmw	$10.88^{+0.17}_{-0.20}$	$2.22^{+0.12}_{-0.24}$	$0.40^{+1.00}_{-0.23}$	$7.40^{+3.39}_{-3.61}$	$-0.74^{+0.60}_{-0.85}$	$0.16^{+0.09}_{-0.10}$	7.94 ± 0.42	⋯	1.0	0.63
8	AT2019dsg	$10.34^{+0.06}_{-0.05}$	$2.12^{+0.04}_{-0.04}$	$0.49^{+0.13}_{-0.09}$	$4.30^{+0.96}_{-0.69}$	$0.11^{+0.05}_{-0.07}$	$0.01^{+0.02}_{-0.01}$	6.90 ± 0.32	86.89 ± 3.92	2.5	0.42
9	AT2019ehz	$9.65^{+0.13}_{-0.16}$	$1.93^{+0.05}_{-0.04}$	$0.76^{+0.67}_{-0.58}$	$6.08^{+4.18}_{-3.05}$	$-1.36^{+0.53}_{-0.46}$	$0.13^{+0.04}_{-0.06}$	5.81 ± 0.46	⋯	1.7	0.32
10	AT2019qiz	$10.28^{+0.04}_{-0.06}$	$2.36^{+0.04}_{-0.06}$	$0.26^{+0.34}_{-0.13}$	$10.95^{+1.16}_{-1.88}$	$-0.41^{+0.14}_{-0.18}$	$0.03^{+0.03}_{-0.02}$	6.48 ± 0.33	69.70 ± 2.30	9.9	0.27
11	AT2019vcb	$9.77^{+0.03}_{-0.07}$	$1.54^{+0.02}_{-0.03}$	$3.00^{+0.57}_{-0.84}$	$10.46^{+1.50}_{-2.48}$	$-0.95^{+0.23}_{-0.22}$	$0.10^{+0.02}_{-0.02}$	6.03 ± 0.36	⋯	1.2	0.44
12	AT2020pj	$10.01^{+0.07}_{-0.08}$	$2.01^{+0.07}_{-0.05}$	$1.43^{+0.47}_{-0.88}$	$9.28^{+2.32}_{-3.84}$	$-1.35^{+0.53}_{-0.34}$	$0.17^{+0.03}_{-0.05}$	6.44 ± 0.31	⋯	1.7	0.35
13	AT2020mot	$10.40^{+0.06}_{-0.08}$	$2.20^{+0.05}_{-0.05}$	$1.18^{+0.35}_{-0.50}$	$9.52^{+2.09}_{-2.65}$	$-0.73^{+0.32}_{-0.38}$	$0.12^{+0.05}_{-0.05}$	6.66 ± 0.34	76.61 ± 5.33	1.4	0.49
14	AT2020neh	$9.80^{+0.05}_{-0.06}$	$1.49^{+0.03}_{-0.03}$	$3.25^{+0.71}_{-0.94}$	$10.41^{+1.46}_{-2.36}$	$-1.19^{+0.26}_{-0.24}$	$0.12^{+0.02}_{-0.02}$	5.43 ± 0.46	40.00 ± 6.00	1.7	0.38
15	AT2020ysg	$10.70^{+0.06}_{-0.07}$	$2.09^{+0.17}_{-0.12}$	$1.63^{+0.43}_{-0.71}$	$10.24^{+1.65}_{-2.79}$	$-0.12^{+0.20}_{-0.37}$	$0.07^{+0.06}_{-0.05}$	8.04 ± 0.33	157.78 ± 13.03	1.2	0.56
16	AT2020vdq	$9.25^{+0.07}_{-0.11}$	$1.69^{+0.09}_{-0.07}$	$1.34^{+0.81}_{-1.08}$	$8.18^{+2.95}_{-3.71}$	$-1.10^{+0.30}_{-0.53}$	$0.06^{+0.04}_{-0.04}$	5.59 ± 0.37	43.56 ± 3.07	1.3	0.27
17	AT2020vwl	$9.89^{+0.08}_{-0.08}$	$2.08^{+0.03}_{-0.04}$	$0.36^{+0.42}_{-0.21}$	$8.81^{+2.18}_{-2.16}$	$-0.84^{+0.17}_{-0.28}$	$0.05^{+0.04}_{-0.03}$	5.79 ± 0.35	48.49 ± 2.00	2.4	0.27
18	AT2020wey	$9.67^{+0.09}_{-0.12}$	$2.05^{+0.04}_{-0.03}$	$0.61^{+0.40}_{-0.39}$	$7.92^{+2.39}_{-1.85}$	$-1.18^{+0.59}_{-0.56}$	$0.11^{+0.04}_{-0.08}$	5.40 ± 0.38	39.36 ± 2.79	2.1	0.24
19	AT2020yue	$10.19^{+0.10}_{-0.14}$	$1.48^{+0.10}_{-0.07}$	$4.18^{+2.94}_{-2.02}$	$7.68^{+3.07}_{-2.93}$	$-0.51^{+0.25}_{-0.34}$	$0.16^{+0.04}_{-0.04}$	6.75 ± 0.32	⋯	1.5	0.59
20	AT2020abri	$9.54^{+0.14}_{-0.17}$	$1.85^{+0.07}_{-0.08}$	$0.29^{+0.46}_{-0.15}$	$6.74^{+3.73}_{-3.04}$	$-1.29^{+0.49}_{-0.48}$	$0.05^{+0.05}_{-0.04}$	5.62 ± 0.51	⋯	0.9	0.36
21	AT2020acka	$11.03^{+0.15}_{-0.19}$	$2.21^{+0.08}_{-0.09}$	$0.56^{+0.98}_{-0.40}$	$7.21^{+3.58}_{-3.71}$	$-1.20^{+0.83}_{-0.50}$	$0.21^{+0.07}_{-0.09}$	8.23 ± 0.40	174.47 ± 25.30	1.1	0.70
22	AT2021axu	$10.20^{+0.11}_{-0.13}$	$1.78^{+0.05}_{-0.05}$	$0.42^{+0.74}_{-0.26}$	$7.82^{+3.16}_{-3.24}$	$-1.57^{+0.33}_{-0.29}$	$0.06^{+0.04}_{-0.03}$	6.59 ± 0.55	73.50 ± 17.26	1.2	0.51
23	AT2021crk	$9.89^{+0.11}_{-0.10}$	$1.28^{+0.11}_{-0.06}$	$2.90^{+2.62}_{-1.57}$	$8.59^{+2.90}_{-3.79}$	$-1.09^{+0.40}_{-0.53}$	$0.06^{+0.04}_{-0.04}$	6.12 ± 0.39	57.62 ± 6.29	1.6	0.48
24	AT2021ehb	$10.23^{+0.01}_{-0.02}$	$2.34^{+0.01}_{-0.02}$	$0.20^{+0.21}_{-0.08}$	$11.96^{+0.41}_{-0.72}$	$-0.43^{+0.04}_{-0.04}$	$0.01^{+0.01}_{-0.00}$	7.16 ± 0.32	99.58 ± 3.83	3.3	0.27
25	AT2021jjm	$9.47^{+0.13}_{-0.14}$	$1.13^{+0.08}_{-0.08}$	$4.53^{+3.34}_{-2.85}$	$6.38^{+3.41}_{-2.76}$	$-1.23^{+0.54}_{-0.52}$	$0.11^{+0.03}_{-0.05}$	5.51 ± 0.51	⋯	0.7	0.52
26	AT2021mhg	$9.65^{+0.12}_{-0.14}$	$2.05^{+0.07}_{-0.07}$	$0.26^{+0.45}_{-0.12}$	$7.71^{+3.14}_{-2.99}$	$-1.27^{+0.57}_{-0.55}$	$0.12^{+0.05}_{-0.07}$	6.13 ± 0.37	57.78 ± 5.25	1.0	0.31
27	AT2021nwa	$10.13^{+0.03}_{-0.05}$	$2.24^{+0.02}_{-0.02}$	$1.09^{+0.12}_{-0.16}$	$10.94^{+1.06}_{-1.55}$	$-0.58^{+0.12}_{-0.12}$	$0.06^{+0.02}_{-0.02}$	7.22 ± 0.32	102.44 ± 5.37	1.7	0.36
28	AT2021qth	$9.73^{+0.14}_{-0.21}$	$1.91^{+0.24}_{-0.17}$	$2.65^{+3.63}_{-1.82}$	$5.17^{+4.93}_{-3.60}$	$-0.94^{+0.67}_{-0.70}$	$0.40^{+0.15}_{-0.17}$	5.95 ± 0.48	⋯	1.2	0.31
29	AT2021sdu	$10.15^{+0.07}_{-0.09}$	$1.45^{+0.07}_{-0.06}$	$2.22^{+2.47}_{-1.28}$	$6.63^{+3.86}_{-2.88}$	$-0.01^{+0.09}_{-0.11}$	$0.07^{+0.02}_{-0.02}$	6.68 ± 0.29	⋯	2.6	0.42
30	AT2021uqv	$10.14^{+0.08}_{-0.11}$	$1.65^{+0.04}_{-0.03}$	$2.18^{+1.16}_{-1.03}$	$7.70^{+3.07}_{-2.87}$	$-1.54^{+0.42}_{-0.33}$	$0.21^{+0.02}_{-0.03}$	6.27 ± 0.39	62.30 ± 7.08	1.4	0.49
31	AT2021utq	$9.66^{+0.09}_{-0.12}$	$1.49^{+0.11}_{-0.08}$	$2.44^{+1.32}_{-1.15}$	$8.81^{+2.64}_{-3.79}$	$-0.94^{+0.48}_{-0.55}$	$0.09^{+0.06}_{-0.06}$	5.84 ± 0.43	⋯	1.1	0.45
32	AT2021yzv	$10.83^{+0.12}_{-0.15}$	$2.15^{+0.08}_{-0.08}$	$0.29^{+0.38}_{-0.15}$	$8.35^{+2.87}_{-3.23}$	$-1.13^{+0.61}_{-0.55}$	$0.13^{+0.07}_{-0.08}$	7.90 ± 0.40	146.38 ± 20.78	1.5	0.61
33	AT2021yte	$9.17^{+0.17}_{-0.21}$	$1.38^{+0.24}_{-0.17}$	$3.40^{+3.48}_{-2.60}$	$6.38^{+3.82}_{-3.57}$	$-1.24^{+0.77}_{-0.58}$	$0.15^{+0.06}_{-0.06}$	5.13 ± 0.45	34.22 ± 4.81	1.6	0.29

Notes. Columns (3)–(8) are host galaxy properties inferred with SED fitting (see Section 4.2.2). The black hole mass $M_{\rm BH}$ is inferred using the $M_{\rm BH}$–σ_* scaling relation for the 19 objects with available σ_* measurements, and using the $M_{\rm BH}$–$M_{\rm gal}$ scaling relation for the remaining 14 objects. $r_{1/2}$ is the mean of (seeing-corrected) half-light radii in the g-, r-, and i-band images as measured by LAMBDAR. $z_{\rm max,h}$ is the maximum redshift out to which the host galaxy can be detected in the ZTF reference catalog (see details in Section 5.2).

(This table is available in machine-readable form.)

(Section 3). The results of $D_{\rm max,t}$ and the corresponding maximum redshift $z_{\rm max,t}$ are shown in Table 4.

However, in steps (1) and (2) of our TDE selection criteria (Section 2.2), we required the detection of each host galaxy in the ZTF reference image, the depth of which (for point sources) is $m \lesssim 23$ (Masci et al. 2019). It is easy to imagine that TDEs hosted by lower-mass galaxies and galaxies with redder colors can only be selected out to a smaller volume (because at higher redshifts, these galaxies will not be cataloged in the ZTF reference, and the transient will appear as *hostless*).

Therefore, for each of the TDE host galaxies, we estimated $z_{\rm max,h}$, which is the maximum redshift out to which the observer-frame PSF AB magnitude (in either g or r band) will be <23. We computed $z_{\rm max,h}$ using the best-fit prospector models derived in Section 4.2.2. To include the effects of PSF photometry on extended sources, we multiplied the model SED fluxes by a factor of $10^{-0.4(m_{\rm PSF}-m_{\rm LAMBDAR})}$, where $m_{\rm PSF}$ is the rPSFMag column in the PS1 StackObjectView catalog (Flewelling et al. 2020), and $m_{\rm LAMBDAR}$ is the PS1 r-band magnitude in the LAMBDAR photometry (see Table 10 in Appendix A). The derived values of $z_{\rm max,h}$ are given in Table 5.

Taken together,

$$z_{{\rm max},i} = \min(z_{{\rm max,t},i},\, z_{{\rm max,h},i}). \quad (8)$$

We find that all 33 TDEs in our sample satisfy $z_i < z_{{\rm max,t},i} < z_{{\rm max,h},i}$. Therefore, for this TDE sample, $z_{\rm max} = z_{\rm max,t}$.

6. Results and Discussion

6.1. Correlations between TDE Photometric and Galaxy Properties

Here, we investigate the correlations between the TDE photometric and host galaxy properties. We focus on the three blackbody parameters ($L_{\rm bb}$, $T_{\rm bb}$, $R_{\rm bb}$), $t_{1/2}$ (defined in

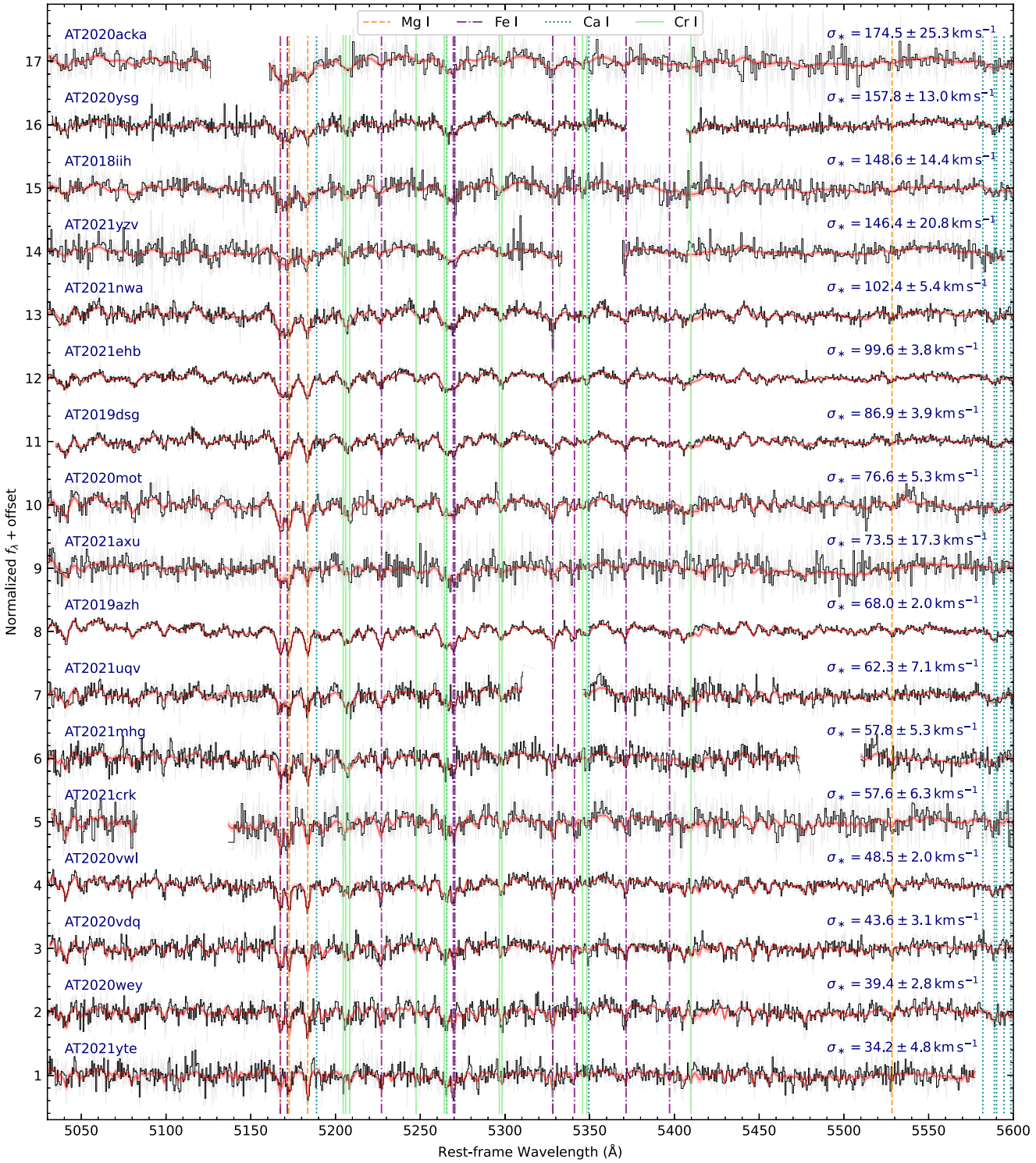

Figure 10. ESI spectra of 17 TDE host galaxies arranged in order of decreasing σ_*. The black lines are the data, and the red lines are the models. Prominent host galaxy absorption lines are indicated by the vertical lines. Masked regions are not plotted. The median S/N of the fitted wavelength range of each spectrum is given in Appendix A (Table 8).

Section 3.3), $\lambda_{\rm Edd}$, and $M_{\rm BH}$. We did not include $M_{\rm gal}$ since it is strongly correlated with $M_{\rm BH}$ (Figure 11). We also did not include $t_{1/2,\rm rise}$ and $t_{1/2,\rm decline}$, because both parameters are strongly correlated with $t_{1/2}$ (this can be seen in Figure 9, where TDEs that rise fast generally also decline fast). The p-value of a Kendalls tau test between $t_{1/2,\rm rise}$ and $t_{1/2,\rm decline}$ is 1.29×10^{-5}. This result is in agreement with Hammerstein et al. (2023). We note that the first ZTF TDE sample study found no correlation between the TDE rise and decline rates (van Velzen et al. 2021), which possibly results from the smaller sample size.

Figure 12 shows the distribution of our sample on various diagrams. Panel (p) shows the p-values of a Kendalls tau test between any two of the six quantities of interest, using the total sample of 33 TDEs and the subset of 28 TDEs at $z < 0.24$ (see reasons for this cut in Section 6.1.1).

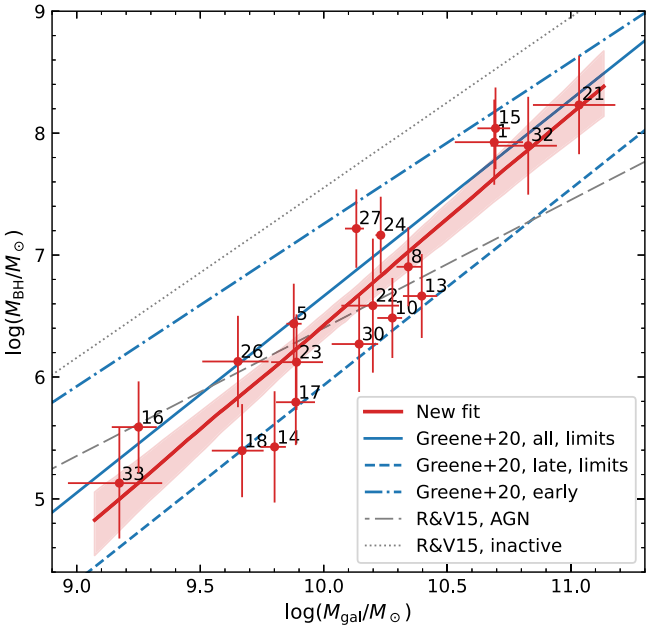

Figure 11. M_{BH} vs. M_{gal} for 19 TDEs with M_{BH} measurements inferred from σ_*, labeled by IDs in Table 3. The solid red line is a linear fit to these objects (Equation (5)). The solid, dashed, and dash–dotted blue lines are relations presented in Greene et al. (2020; supplemental Table 5), derived using all galaxies (with upper limits on M_{BH}), late-type galaxies (with upper limits), and early-type galaxies. The thin dotted and long dashed gray lines are from Reines & Volonteri (2015) using AGN and inactive galaxies.

6.1.1. The Selection Effects

Considering the whole sample of 33 TDEs, the correlations between eight pairs of parameters appear to be significant. While a few similar correlations have also been reported by Hammerstein et al. (2023), we note that such correlations might be promoted by selection effects. To be in our sample, the host galaxies need to be bright enough to be detected in the ZTF reference catalog (Section 2.2). Since $M_{BH} \propto M_{gal}^{1.6}$ (see Equation (5)) and $M_{gal} \propto L_{gal}$, we can find luminous TDEs hosted by higher-mass BHs even at high redshifts.

Based on the the values of $z_{max,h}$ computed in Section 5.2 (see Table 5), within $z < 0.24$, even the faintest host galaxy of our sample (i.e., the host of AT2020wey) can be detected in the ZTF reference catalog. Therefore, within this volume, there should be no observational bias toward bright galaxies.[34]

Restricting ourselves to the 28 TDEs at $z < 0.24$, the correlation between a few pairs of parameters becomes statistically less insignificant. The correlation between R_{bb} and T_{bb} becomes even more significant, as expected in a flux-limited sample if many TDEs have a similar peak blackbody luminosity. In Sections 6.1.2 and 6.1.3, we discuss the other two strong correlations.

6.1.2. Duration above Half-max Versus Black Hole Mass

The correlation between the light-curve evolutionary speed and BH mass has been reported in the literature (van Velzen et al. 2020; Gezari 2021; Hammerstein et al. 2023), which we confirm in panel (e) of Figure 12. We note that the p-values between $t_{1/2,rise}$ and log M_{BH} (2.3×10^{-3}) and between $t_{1/2,decline}$ and log M_{BH} (1.0×10^{-3}) are comparable to (but slightly greater than) the p-value between $t_{1/2}$ and log M_{BH} (5.0×10^{-4}).

We define $M_6 \equiv M_{BH}/(10^6\, M_\odot)$. A log-linear fit between $t_{1/2}$ and M_{BH} for 33 TDEs yields the following (see the dashed line):

$$\frac{t_{1/2}}{42.5^{+3.9}_{-3.5}\,\mathrm{days}} = M_6^{0.14\pm0.04}, \tag{9}$$

which has an intrinsic scatter of 0.17 dex. Restricting to the 28 TDEs at $z < 0.24$, we obtain a similar power-law relation of the following (see the solid line):

$$\frac{t_{1/2}}{41.6^{+3.8}_{-3.5}\,\mathrm{days}} = M_6^{0.16\pm0.05}, \tag{10}$$

which has an intrinsic scatter of 0.15 dex.

Equations (9), (10) can be compared with the fall-back timescale of the most bound debris (see the dotted line):

$$\frac{t_{fb}}{41\ \mathrm{days}} = M_6^{1/2} m_*^{-1} r_*^{3/2}. \tag{11}$$

The observed shallow power-law index may be caused by other processes. For example, the circularization of the stellar debris has been shown to be more rapid around higher-mass BHs (Bonnerot et al. 2016; Bonnerot & Lu 2020).

6.1.3. Eddington Ratio Versus Black Hole Mass

The distribution of our sample on the Eddington ratio and BH mass diagram is shown in panel (d) of Figure 12. A log-linear fit between λ_{Edd} and M_{BH} for 33 TDEs yields the following (see the dashed line):

$$\frac{\lambda_{Edd}}{0.45^{+0.12}_{-0.10}} = M_6^{-0.52\pm0.11}, \tag{12}$$

which has an intrinsic scatter of 0.28 dex. To correct for the selection bias, we also fit for the 28 TDEs at $z < 0.24$, obtaining a steeper power law as follows (see the solid line):

$$\frac{\lambda_{Edd}}{0.41^{+0.11}_{-0.09}} = M_6^{-0.74\pm0.12}, \tag{13}$$

which has an intrinsic scatter of 0.11 dex. This relatively tight correlation is not surprising since by definition $\log \lambda_{Edd} \equiv \log L_{bb} - \log M_{BH} - 38.10$. And Equation (13) comes from the fact that L_{bb} is only weakly positively correlated with M_{BH} (see the filled markers in panel (b)).

Equation (13) can also be compared with the expected peak fall-back rate of $\dot{M}_{fb} \approx M_*/(3t_{fb})$ relative to the Eddington accretion rate (see the dotted line):

$$\frac{\dot{M}_{fb}}{\dot{M}_{Edd}} = 136\, \eta_{-1} m_*^2 r_*^{-3/2} M_6^{-3/2} \tag{14}$$

where η is the accretion radiative efficiency, and $\eta_{-1} \equiv \eta/0.1$. The observed power law is much shallower than that in Equation (14). In fact, the majority of TDEs in panel (d) lie well below the dotted line. One likely reason might be Eddington-limited accretion. Indeed, none of the TDEs in our sample appear to have a peak blackbody luminosity that is significantly super-Eddington. Another natural explanation is that the UV and optical peak blackbody luminosity only

[34] Note that, here, we do not consider galaxies with an absolute r-band PSF magnitude fainter than that of AT2020wey.

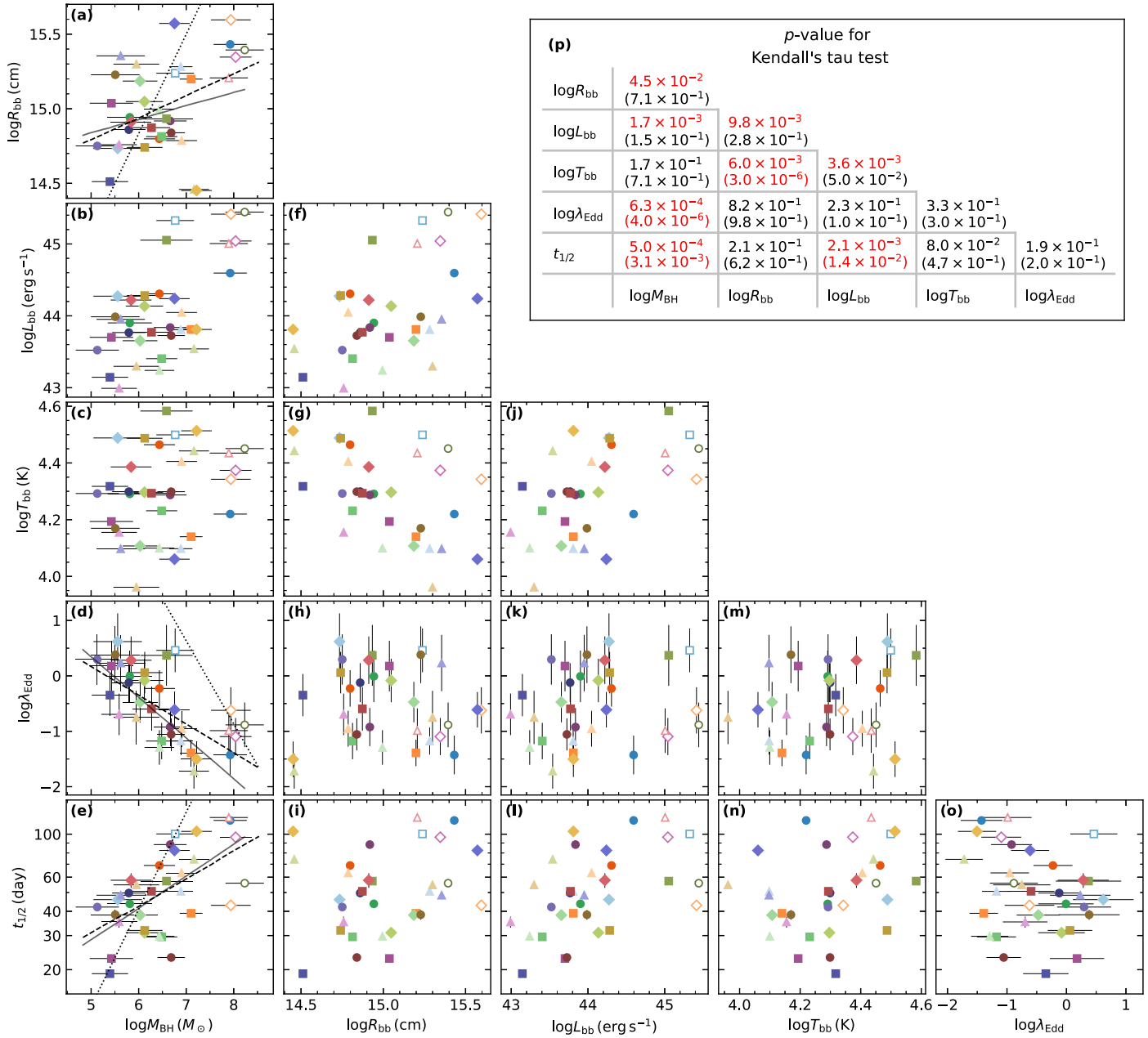

Figure 12. Panels (a)–(o): correlations between TDE photometric properties, $\lambda_{\rm Edd}$, and $M_{\rm BH}$. Symbol colors follow the same convention as in Figure 2 and Figure 9. Hollow markers show objects at $z > 0.24$, where there is an observational bias toward selecting TDEs in higher-mass galaxies. Panel (a): the dotted line shows the expected $R_{\rm bb} \propto M_{\rm BH}^{2/3}$ scaling relation in a fiducial cooling envelop model (Metzger 2022); the dashed ($R_{\rm bb} \propto M_{\rm BH}^{0.15}$) and solid ($R_{\rm bb} \propto M_{\rm BH}^{0.09}$) lines show the best-fit power laws using all markers and filled markers, respectively (see Section 6.3). Panel (d): the dotted line shows the expected Eddington ratio of peak fall-back accretion rate $\lambda_{\rm Edd} \propto M_{\rm BH}^{-3/2}$; the dashed ($\lambda_{\rm Edd} \propto M_{\rm BH}^{-0.52}$) and solid ($\lambda_{\rm Edd} \propto M_{\rm BH}^{-0.74}$) lines show the best-fit power laws using all markers and filled markers, respectively (see Section 6.1.3). Panel (e): the dotted line shows the expected fall-back timescale of $t_{\rm l/2} \propto M_{\rm BH}^{1/2}$; the dashed ($t_{\rm l/2} \propto M_{\rm BH}^{0.14}$) and solid ($t_{\rm l/2} \propto M_{\rm BH}^{0.16}$) lines show the best-fit power laws using all markers and filled markers, respectively (see Section 6.1.2). Panel (p): p-value of Kendall's tau test for 15 pairs of parameters. The results using 33 TDEs are shown outside the parenthesis, and the results using 28 TDEs at $z < 0.24$ are shown in the parenthesis. Significant correlations with $p < 0.05$ are highlighted in red colors.

captures a fraction of the total bolometric luminosity, with the EUV and X-ray luminosity unaccounted for.

6.2. Luminosity Functions

While theoretical calculations show that the TDE rate may decline by a factor of 5 from $z = 0$, to $z = 1$ (Kochanek 2016), a detailed discussion of the redshift evolution of TDE rates is beyond the scope of this work. Hereafter, we assume that the TDE rate remains the same out to the highest redshift object in our sample (i.e., $z < 0.519$).

6.2.1. Rest-frame g-band LF

In the upper panel of Figure 13, we show the distribution of the 33 TDEs in the observed redshift versus peak rest-frame g-band luminosity diagram, where the boundaries of the nine $\log L_g$ bins are indicated with vertical lines. For a certain bin j with n_j TDEs and width $\Delta_j \log L_g$, the rate

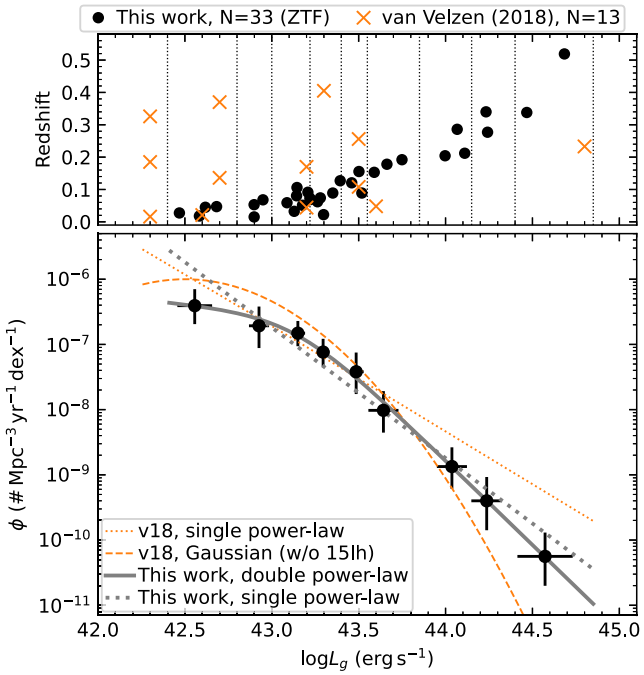

Figure 13. Upper: redshift vs. log L_g for 33 TDEs in this work (circles) and 13 TDEs used by van Velzen (2018; crosses). The boundaries of the 9 luminosity bins used in this work are indicated by the vertical dotted lines. Lower: TDE LF in rest-frame g band. We show the single and double power-law fits as well as the two LFs presented in van Velzen (2018).

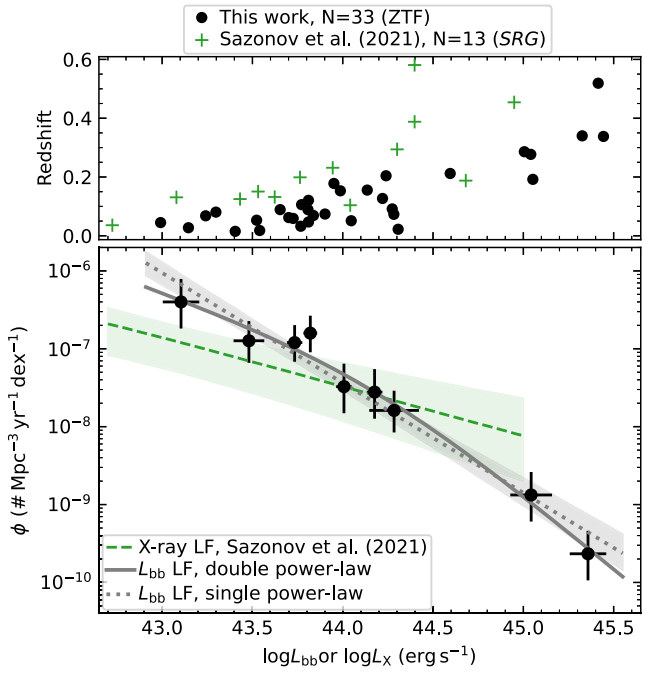

Figure 14. Upper: redshift vs. log L_{bb} for 33 TDEs in this work (circles), and vs. the peak X-ray luminosity for 13 SRG-selected TDEs presented by Sazonov et al. (2021). Lower: TDE LF in terms of peak UV and optical blackbody luminosity or peak 0.2–6 keV X-ray luminosity. The dotted and solid gray lines show the single power-law (Equation (17)) and double power-law (Equation (18)) fits. The dashed green line shows the X-ray LF given by Sazonov et al. (2021). For the dashed and dotted lines, 1σ uncertainties are indicated with the semitransparent regions.

$\phi_j = [\sum_{i=1}^{n_j} 1/(T_{\rm span,}i\mathcal{V}_{\rm max,}i)]/\Delta_j \log L_g$, and we compute the corresponding uncertainty of ϕ_j based on the Poisson error (Gehrels 1986). For example, when $n_j = 4$, the upper and lower limits of ϕ_j are $\phi_j^u = \phi_j \times 7.163/4$, and $\phi_j^l = \phi_j \times 2.086/4$.

First, we fit the seven solid data points in the lower panel of Figure 13 with a single power law of

$$\phi(L_g) = \frac{d\mathcal{R}(L_g)}{d\log L_g} = \dot{N}_0 \left(\frac{L_g}{L_0}\right)^{-\gamma}. \quad (15)$$

For $L_0 = 10^{43}$ erg s^{-1}, we have $\dot{N}_0 = 1.82^{+0.48}_{-0.39} \times 10^{-7}$ Mpc^{-3} yr^{-1}, and $\gamma = 2.00^{+0.15}_{-0.14}$. The best-fit model, shown as the dotted gray line in Figure 13, is steeper than the power-law model with $\gamma = 1.6 \pm 0.2$ presented by van Velzen (2018).

Next, we describe the LF with a double power law of the following:

$$\phi(L_g) = \dot{N}_0 \left[\left(\frac{L_g}{L_{\rm bk}}\right)^{\gamma_1} + \left(\frac{L_g}{L_{\rm bk}}\right)^{\gamma_2}\right]^{-1} \quad (16)$$

where $-\gamma_1$ is the faint-end slope, $-\gamma_2$ is the bright-end slope, and $L_{\rm bk}$ is the characteristic break luminosity. We perform the fit with MCMC, obtaining $L_{\rm bk} = 1.36^{+0.89}_{-0.48} \times 10^{43}$ erg s^{-1}, $\dot{N}_0 = 2.87^{+2.98}_{-1.68} \times 10^{-7}$ Mpc^{-3} yr^{-1}, $\gamma_1 = 0.26^{+0.61}_{-0.80}$, and $\gamma_2 = 2.58^{+0.27}_{-0.25}$. This model is shown as the solid gray line in Figure 13.

The BIC value of the double power-law fit is smaller than the single power-law fit by 6.07. According to Raftery (1995), a BIC difference of 0–2 is weak, a difference of 2–6 is positive, and a difference of 6–10 is strong. Therefore, we conclude that a double power-law LF provides a better description of the data.

Our result of $\phi(L_g)$ is consistent with that provided by van Velzen (2018) at $L_g \sim 10^{43.5}$ erg s^{-1}. For overluminous events, ASASSN-15lh is the only object with $L_g > 10^{43.6}$ erg s^{-1} in the van Velzen (2018) sample. The fact that nine objects in our sample have $L_g > 10^{43.6}$ erg s^{-1} allows us to constrain the upper end of the LF more precisely.

For subluminous events, the LF measured with the ZTF sample is shallower, and the rate is about a factor of 2 smaller than that measured by van Velzen (2018). No objects in our sample have $L_g < 10^{42.4}$ erg s^{-1}, while three objects in the van Velzen (2018) sample (GALEX-D1-9, GALEX-D23H-1, and iPTF16fnl) have $L_g \approx 10^{42.3}$ erg s^{-1}. However, the two GALEX events have relatively sparse light curves (note the lack of data points on the rise in Figure 15 of Gezari et al. 2008; and Figure 2 of Gezari et al. 2009), which can possibly lead to an underestimation of their peak g-band luminosity.

6.2.2. UV and Optical Blackbody LF

Following the procedures outlined in Section 6.2.1, we compute the TDE rate as a function of the peak UV and optical blackbody luminosity (see Figure 14).

With $L_0 = 10^{43}$ erg s^{-1}, a single power-law fit yields

$$\phi(L_{\rm bb}) = (9.43^{+4.53}_{-3.04} \times 10^{-7}\ {\rm Mpc^{-3}\ yr^{-1}}) \left(\frac{L_{\rm bb}}{L_0}\right)^{-1.41\pm0.14}. \quad (17)$$

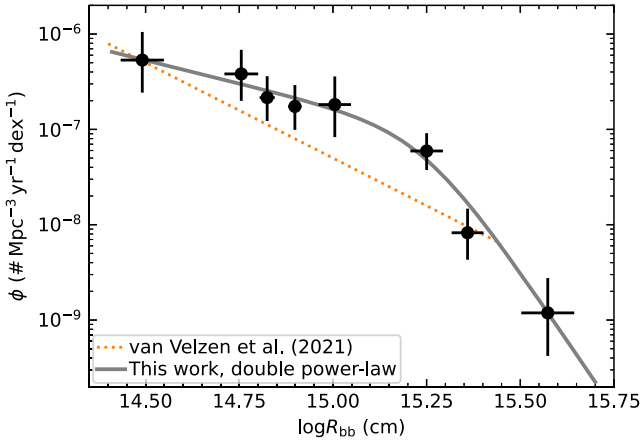

Figure 15. TDE rate as a function of $R_{\rm bb}$.

A double power-law fit yields

$$\phi(L_{\rm bb}) = (5.72^{+7.08}_{-3.29} \times 10^{-8}\,{\rm Mpc^{-3}\,yr^{-1}}) \times \left[\left(\frac{L_{\rm bb}}{L_{\rm bk}}\right)^{0.84^{+0.30}_{-0.36}} + \left(\frac{L_{\rm bb}}{L_{\rm bk}}\right)^{1.93^{+0.32}_{-0.27}}\right]^{-1}, \quad (18)$$

where $L_{\rm bk} = 1.46^{+1.20}_{-0.64} \times 10^{44}\,{\rm erg\,s^{-1}}$. The BIC value of the double power-law fit is greater than that of the single power-law fit by 2.2. Therefore, the single power-law fit is slightly favored.

With Equation (17), the integrated volumetric rate of optical TDEs with $L_{\rm bb} > 10^{43}\,{\rm erg\,s^{-1}}$ is $3.1^{+0.6}_{-1.0} \times 10^{-7}\,{\rm Mpc^{-3}\,yr^{-1}}$. This can be compared with the volumetric rate of X-ray selected TDEs. Using a sample of 13 TDEs selected from SRG/eROSITA, Sazonov et al. (2021) found that the majority of X-ray selected events are intrinsically faint in the optical. Previous studies also implied that the majority of ZTF-selected TDEs are intrinsically faint in the X-ray band (see Figure 8 of Hammerstein et al. 2023). Using the LF provided by Sazonov et al. (2021), the rate of X-ray TDEs with $L_{\rm X} > 10^{43}\,{\rm erg\,s^{-1}}$ is $\sim 2.3 \times 10^{-7}\,{\rm Mpc^{-3}\,yr^{-1}}$. Therefore, we conclude that the rates of optically loud and X-ray loud TDEs are comparable to each other.

6.3. Rate Dependence on R_{bb}

Following the procedures outlined in Section 6.2.1, we compute the TDE rate as a function of the peak blackbody radius $R_{\rm bb}$ (see Figure 15).

A double power-law fit gives

$$\phi(R_{\rm bb}) = (1.00^{+1.33}_{-0.62} \times 10^{-7}\,{\rm Mpc^{-3}\,yr^{-1}}) \times \left[\left(\frac{R_{\rm bb}}{R_{\rm bk}}\right)^{0.97^{+0.59}_{-0.67}} + \left(\frac{R_{\rm bb}}{R_{\rm bk}}\right)^{5.81^{+2.16}_{-1.57}}\right]^{-1}, \quad (19)$$

where $R_{\rm bk} = 1.75^{+0.53}_{-0.41} \times 10^{15}\,{\rm cm}$. Compared with the $\phi(R_{\rm bb}) \propto R_{\rm bb}^{-2}$ relation found by van Velzen et al. (2021), our results indicate a slope that is much shallower at small radii and much steeper at large radii.

van Velzen et al. (2021) suggested that the observed $R_{\rm bb}$ in the majority of TDEs can be explained by the self-intersection radius ($R_{\rm I}$) of the debris stream for disruptions of stars with $0.2 \lesssim m_* \lesssim 3$ and impact parameter $R_{\rm p}/R_{\rm T} \approx 1$ (Dai et al. 2015). For TDEs hosted by the most massive BHs, we find $R_{\rm bb} \gg R_{\rm I}$ because the self-intersection radius decreases with $M_{\rm BH}$ for $M_{\rm BH} \gtrsim 10^{6.5}\,M_\odot$ (see Figure 8 of Gezari 2021). In fact, we find that TDEs at a given $M_{\rm BH}$ show a broad range of $R_{\rm bb}$. As suggested by Nicholl et al. (2022), $R_{\rm bb}$ can vary a lot even for the same $M_{\rm BH}$ depending on the impact parameter—it could be set by the collision-induced outflow in shallow encounters, but by the disk wind in deep encounters.

In the TDE cooling envelope model (Loeb & Ulmer 1997; Metzger 2022), the stellar debris promptly form a quasi-spherical envelope. The "virial radius" of the envelope, which is bound to the massive BH by the energy spread imparted by the disruption process, is $R_{\rm v} \approx 6.8 \times 10^{13}\,{\rm cm}\,m_*^{2/15} M_6^{2/3} (M_{\rm e}/0.2\,M_\odot)$, where $M_{\rm e}$ is the mass of the envelope (see Equation (7) of Metzger 2022). The photosphere radius is greater than this $R_{\rm v}$ by a factor of $\sim$10, which is shown as the dotted line in panel (a) of Figure 12. The above scaling relation is derived assuming a lower main-sequence star mass–radius relationship. The observed $R_{\rm bb}$ dependence on $M_{\rm BH}$ is much shallower with huge scatter, which might be accounted for with a broader range of stellar properties.

The steep upper power-law index ($\gamma_2 \sim 5.8$) in Equation (19) suggests that there is a physical maximum blackbody radius for TDEs: $R_{\rm bb,max} \sim$ few $\times 10^{15}$ cm. One possibility is that this maximum radius corresponds to the semimajor axis of the most bound tidal debris $a \simeq 0.5 R_* (M_{\rm BH}/M_*)^{2/3} \simeq 3 \times 10^{15}\,{\rm cm} (M_{\rm BH}/10^{7.5} M_\odot)^{2/3}$, where we have taken the mass–radius relation $R_* \propto M_*^{\approx 2/3}$ for main-sequence stars. Under this hypothesis, the fact that the TDE rate is strongly suppressed at $M_{\rm BH} \gtrsim 10^{7.5} M_\odot$ (see Section 6.4) would lead to a maximum blackbody radius that is in reasonable agreement with observations. However, we leave detailed theoretical considerations to future works.

6.4. Optical TDE Black Hole Mass Function

Since the uncertainty of $\log M_{\rm BH}$ is relatively large (0.1–0.4 dex), instead of the binning method utilized in Sections 6.2 and 6.3, we compute the optical TDE black hole mass function using kernel density estimation. We adopt a Gaussian kernel with the same variance as the uncertainties of the log $M_{\rm BH}$ measurements.

The upper panel of Figure 16 shows the raw observed number of TDEs per dex $dN/d\log M_{\rm BH}$, which peaks at $M_{\rm BH} \approx 10^{6.6}\,M_\odot$. We estimated the 1σ Poisson single-sided upper and lower limits by interpolating Table 1 and Table 2 of Gehrels (1986).

The lower panel of Figure 16 shows the optical TDE rate with respect to $M_{\rm BH}$. We observed a significant drop of $\phi(M_{\rm BH})$ from $10^{7.4}\,M_\odot$ to $10^{8.2}\,M_\odot$. This roughly corresponds to $M_{\rm Hills}$ for main-sequence stars. A similar result was first reported by van Velzen (2018, Figure 3) and later updated by van Velzen (2020, Figure 13). While more massive galaxies exhibit shallower ("cored") stellar density profiles that can also lead to a suppression of TDE rates by a factor of $\lesssim$10 (see Figure 5 of Magorrian & Tremaine 1999; and Figure 4 of Stone & Metzger 2016), this effect alone does not account for the observed (much steeper) rate suppression.

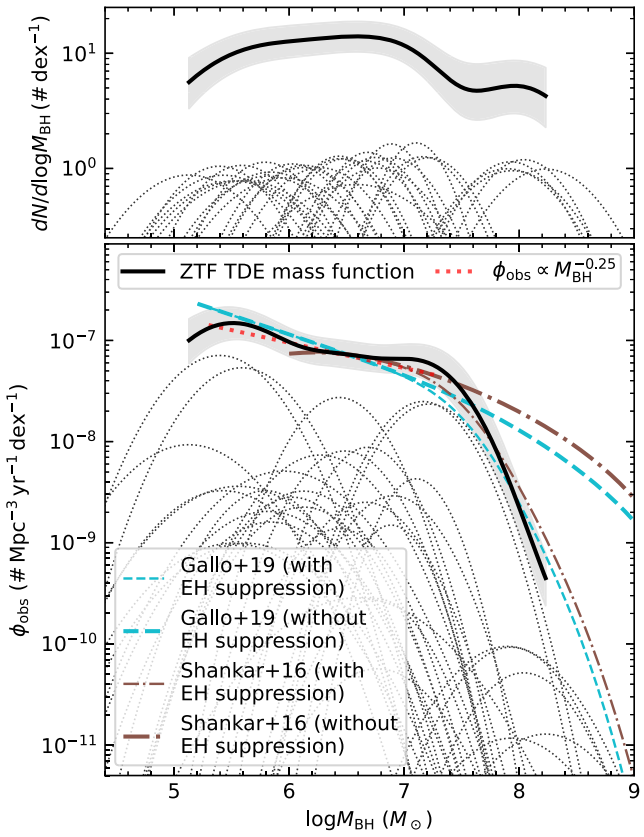

Figure 16. Upper: the thin lines are the log $M_{\rm BH}$ PDFs of the 33 TDE host galaxies. The think black line shows the total number of detected TDEs per dex, computed by summing over the individual Gaussians and plotted between the peak of the PDF of the lowest BH mass ($10^{5.13}\,M_\odot$) and highest BH mass ($10^{8.23}\,M_\odot$). The semitransparent region represents the 1σ uncertainties. Lower: the thin dotted lines are the PDFs (in the upper panel) multiplied by $\mathcal{R}_i$. The solid black curve shows the total optical TDE rate as a function of $M_{\rm BH}$. From $10^{5.3}\,M_\odot$ to $10^{7.3}\,M_\odot$, the slope follows a power law of $\phi \propto \log M_{\rm BH}^{-0.25}$ (red dotted line). We show predictions of two BHMFs (Shankar et al. 2016; Gallo & Sesana 2019) with and without the event-horizon (EH) suppression factor $g(M_{\rm BH})$ (see Equation (20)), normalized to match the black curve at $M_{\rm BH} = 10^{6.5}\,M_\odot$.

To compare our observations to theoretical predictions, we write the mass function for the BHs that are causing TDEs as

$$\phi(M_{\rm BH}) = \dot{N}_0 \times M_6^{\beta} \times \frac{dn_{\rm BH}}{d\log M_{\rm BH}} g(M_{\rm BH}), \tag{20}$$

where $\dot{N}_0 \times M_6^{\beta}$ is the rate at which stars are scattered into the loss cone ($\dot{N}_0$ being a normalization constant, and β will be explained shortly), $dn_{\rm BH}/d\log M_{\rm BH}$ is the local BHMF, and $g(M_{\rm BH})$ is the event-horizon suppression factor that describes the fraction of stars that produce observable optical flares. The observed optical TDE mass function, $\phi_{\rm obs}$, is computed by convolving Equation (20) with a Gaussian kernel of the typical $\log M_{\rm BH}$ measurement uncertainty of 0.3 dex. The convolution is needed since the measurement error blurs and broadens the distribution of quantities (Kelly & Merloni 2012).

Most TDEs originate from the BH's sphere of influence $R_{\rm infl}$ (Wang & Merritt 2004), where the number of stars within $R_{\rm infl}$ is $N \sim M_{\rm BH}/M_*$. Since $R_{\rm infl} \approx GM_{\rm BH}/\sigma_*^2 \propto \sigma_*^2 \sim M_{\rm BH}^{1/2}$, the orbital period at $R_{\rm infl}$ is $P_{\rm orb} \propto R_{\rm infl}^{3/2}/M_{\rm BH}^{1/2} \propto M_{\rm BH}^{1/4}$. The two-body relaxation timescale at $R_{\rm infl}$ is $t_{\rm rel} \propto (P_{\rm orb}/N)\left(\frac{M_{\rm BH}}{M_*}\right)^2 \propto M_{\rm BH}^{5/4}$ (Alexander 2017). The TDE rate is expected to be the total number of stars within the sphere of influence divided by $t_{\rm rel}$, which is $\sim N/t_{\rm rel} \propto M_{\rm BH}/t_{\rm rel} \propto M_{\rm BH}^{-1/4}$. Therefore, in Equation (20), we adopt $\beta = -0.25$.

The rate suppression factor $g(M_{\rm BH}) \sim 1$ at $M_{\rm BH} \lesssim 10^7\,M_\odot$, and drops at higher BH masses because stars are swallowed by the event horizon. The shape of $g(M_{\rm BH})$ depends on the stellar age, the stellar metallicity, the BH spin distribution, the stellar density structure (how centrally concentrated the star is), the exact boundary between full and partial TDEs, and the rate at which stars of different masses are scattered into the loss cone (see more detailed theoretical calculations in Huang & Lu 2022). We compute $g(M_{\rm BH})$ as the fraction of stars in a given stellar population that satisfies $M_{\rm Hills}(m_*, M_{\rm BH}) < M_{\rm BH}$. The stellar population we consider has metallicity $[{\rm Fe/H}] = 0.3$ (twice solar, appropriate for stars near galactic centers) and a single age of 100 Myr. Our small sample is insufficient to differentiate models of different stellar ages, BH spins, and loss-cone filling mechanisms.

Using two BHMFs (Shankar et al. 2016; Gallo & Sesana 2019), the predictions of $\phi_{\rm obs}$ are shown as the dashed cyan and dashed–dotted brown lines in the lower panel of Figure 16. To demonstrate the effect of event-horizon suppression, we show the results with and without the $g(M_{\rm BH})$ factor in thin and thick lines, respectively. All curves are scaled at $M_{\rm BH} = 10^{6.5}\,M_\odot$ to match the observation (the thick black line). We confirm that the observed high-mass rate drop is consistent with the theoretical expectation of the event-horizon effect.

A novel result in Figure 16 is that the optical TDE mass function roughly follows a power law of $\phi_{\rm obs} \propto M_{\rm BH}^{-0.25}$ over 2 orders of magnitude in BH mass ($10^{5.3}\,M_\odot \lesssim M_{\rm BH} \lesssim 10^{7.3}\,M_\odot$). In Section 6.7, we discuss the implications of this result for the local BHMF.

6.5. Rate Enhancement in Green Galaxies and Suppression in Blue Galaxies

Following the procedures outlined in Section 6.4, we compute the TDE rate as a function of $M_{\rm gal}$. We limit the minimum kernel bandwidth to be 0.15. In panel (a) of Figure 17, the thin lines show the probability density function (PDF) of each host's $\log M_{\rm gal}$ multiplied by $\mathcal{R}_i$, and the thick line shows the observed optical TDE galaxy mass function $\phi(M_{\rm gal})$.

Using Equations (5) and (20) and assuming that the occupation fraction of BHs is close to unity, the observed TDE galaxy mass function should follow

$$\phi(M_{\rm gal}) \approx \dot{N}_0' M_{\rm gal}^{-0.41} \frac{dn_{\rm gal}}{d\log M_{\rm gal}} g(M_{\rm gal}), \tag{21}$$

where $dn_{\rm gal}/d\log M_{\rm gal}$ is the local galaxy mass function (GMF). We took the GMF given by Baldry et al. (2012), which is similar to the most recent GMF (Wright et al. 2017) at $M_{\rm gal} \gtrsim 10^9\,M_\odot$. At a typical galaxy mass of $M_{\rm gal} = 10^{10}\,M_\odot$, the optical TDE rate is $3.2^{+0.8}_{-0.6} \times 10^{-5}$ galaxy^{-1} yr^{-1}, as shown by the dashed purple line in panel (a) of Figure 17.

Next, we aim to quantify the relative optical TDE rate in galaxies with different colors. In Figure 18, we show the host galaxy distribution on the ${}^{0,0}u - r$ versus $M_{\rm gal}$ diagram. To

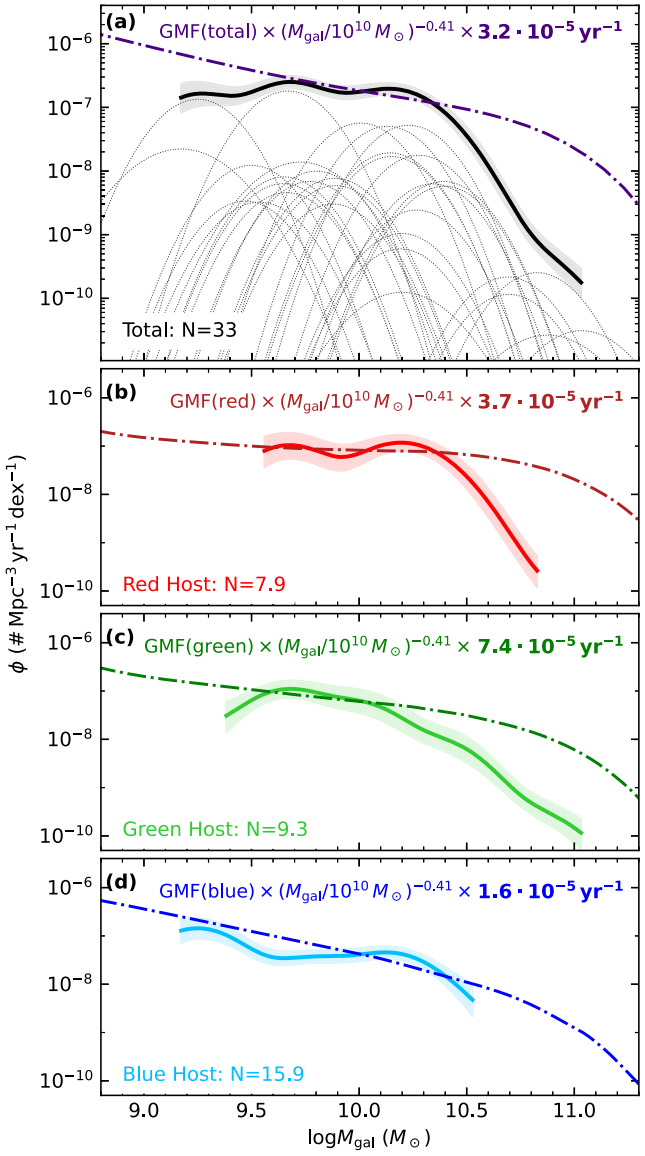

Figure 17. Panel (a): the dotted thin lines represent the values of $\mathcal{R}_i$ (Equation (7)) multiplied by the individual PDFs of log M_{gal}. The solid thick curve shows the total optical TDE rate as a function of M_{gal}, plotted between the peak of the PDF of the lowest galaxy mass ($10^{9.17}$ $M_\odot$) and highest galaxy mass ($10^{11.03}$ $M_\odot$). The semitransparent region represents the 1σ uncertainties. Panels (b)–(d): the observed optical TDE galaxy mass functions in three bins of $\mathcal{C}$ (Equation (23)). The dashed–dotted lines show the local GMFs multiplied by $M_{gal}^{-0.41}$ and scaled to match the observation at $M_{gal} = 10^{10}$ $M_\odot$.

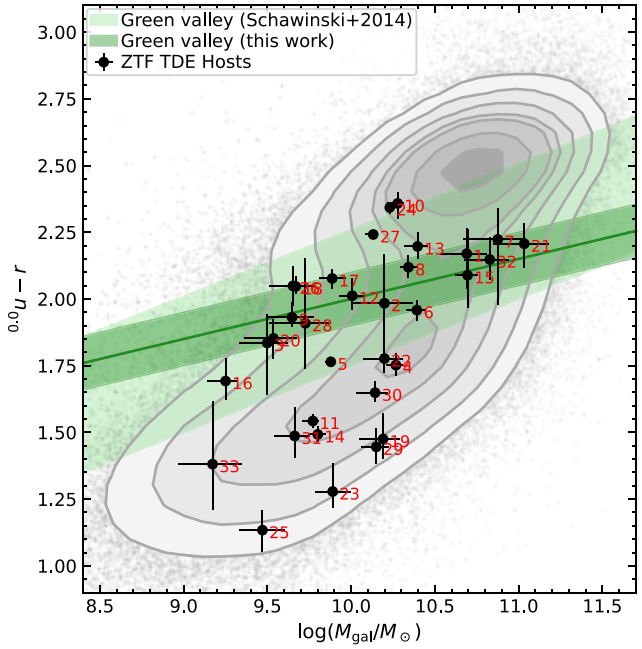

Figure 18. Host galaxies of the TDE sample on the $^{0,0}u - r$ vs. M_{gal} diagram, labeled by the IDs in Table 3. The background contours represent a comparison sample of galaxies from SDSS (see text). The region of green valley defined by Schawinski et al. (2014) is denoted by the light green band. In this work, we define a narrower region of green valley (dark green band) by following the contour of the SDSS comparison sample. The solid green line marks the middle of the new green valley (Equation (22)).

compare the properties of TDE hosts to the population of local galaxies, we started with the flux-limited ($14 \leqslant m_r \leqslant 17.77$) sample of $\sim 6.6 \times 10^5$ spectroscopically classified SDSS galaxies (Strauss et al. 2002) with M_{gal} estimated by Mendel et al. (2014; Table 4). We computed $^{0,0}u - r$ using the rest-frame absolute magnitude in u and r bands provided by the `Photoz` table in SDSS DR7 (Abazajian et al. 2009). To build a comparison sample representative of galaxies that our ZTF TDE selection is sensitive to, for each TDE in our sample, we randomly select 10^3 galaxies with $z < z_{max}$, where z is the redshift of the SDSS galaxy, and z_{max} is computed in Section 5.2. The gray contours in Figure 18 are regions encircling 6.7%, 16%, 31%, 50%, 69%, 84%, and 93.3% (i.e., in steps of 0.5σ) of the final sample of 3.3×10^4 galaxies.

The region of green-valley galaxies defined by Schawinski et al. (2014) is marked by the light green band in Figure 18, which already enclosed galaxies in the "red sequence" and "blue cloud" loci of the SDSS comparison sample. Therefore, we define a new green-valley locus (shown as the solid green line):

$$^{0,0}u - r \;=\; 0.5 + 0.15 \times \log(M_{gal}/M_\odot). \qquad (22)$$

Based on Equation (22), we define a new quantity of M_{gal}-corrected color:

$$\mathcal{C} \equiv {}^{0,0}u - r - 0.5\text{–}0.15 \times \log(M_{gal}/M_\odot), \qquad (23)$$

which represents the vertical distance to the green-valley loci on the color–mass diagram. We define red, green, and blue galaxies to be those with $\mathcal{C} > 0.1$, $|\mathcal{C}| \leqslant 0.1$, and $\mathcal{C} < -0.1$, respectively.

We compute $\phi(M_{gal})$ for red, green, and blue galaxies. Note that the uncertainty of $\mathcal{C}$ is not negligible and is dominated by the uncertainty of $^{0,0}u - r$. Therefore, for each TDE host, we computed the PDF of its $\mathcal{C}$ (assuming Gaussian distributions), and calculated the probabilities of it being a red or green or blue galaxy. For example, the host position of AT2018iih/ZTF18acaqdaa (ID 1) is in the green valley, but the probability of it being a red, green, and blue galaxy is 0.40, 0.52, and 0.08, respectively. The resulting $\phi(M_{gal})$ for three $\mathcal{C}$ bins are shown as the solid thick curves in panels (b)–(d) of Figure 17.

The GMFs for the three $\mathcal{C}$ bins are computed using the Mendel et al. (2014) sample. By definition, GMF(red) + GMF (green) + GMF(blue) = GMF(total). We compute $M_{gal}^{-0.41} \times$ GMF, and scale it to match the observed optical TDE galaxy mass function at the typical galaxy mass of 10^{10} $M_\odot$.

Considering red, green, and blue galaxies, the per-galaxy TDE rate is $3.7^{+2.3}_{-1.5} \times 10^{-5}$ galaxy^{-1} yr^{-1}, $7.4^{+5.0}_{-3.2} \times 10^{-5}$ galaxy^{-1} yr^{-1}, and $1.6^{+0.6}_{-0.4} \times 10^{-5}$ galaxy^{-1} yr^{-1}, respectively. At a typical galaxy mass of $M_{\rm gal} = 10^{10}\,M_\odot$, the relative ratio of optical TDE rate in red, green, and blue galaxies is $1 : \frac{7.4^{+5.0}_{-3.2}}{3.7^{+2.3}_{-1.5}} : \frac{1.6^{+0.6}_{-0.4}}{3.7^{+2.3}_{-1.5}} = 1 : 2.0^{+1.1}_{-0.7} : 0.4^{+0.2}_{-0.1}$.

The rate suppression in blue galaxies may come from the fact that star-forming galaxies exhibit larger amounts of dust in the galaxy nuclei. It is expected that optical searches, which generally select blue transients, will be biased against TDEs, which are intrinsically redder due to dust extinction (Roth et al. 2021). The rate enhancement in green-valley galaxies can be attributed to the higher number density of stars scattered into the loss cone following recent star formation or galaxy mergers (e.g., French et al. 2020; Hammerstein et al. 2021d). We note that the rate enhancement we found appears to be smaller than previous observational constraints (Law-Smith et al. 2017; French et al. 2020; Hammerstein et al. 2021d), although, instead of using the "green-valley" definition, some other studies focus on the overrepresentation factor in E + A galaxies.

6.6. TDE Rates: The Tension between Observations and Loss-cone Models

Our new results have brought back to life a tension between observationally inferred TDE rates and those computed using quasi-empirical models (Wang & Merritt 2004; Stone & Metzger 2016). For example, in Wang & Merritt (2004), the volumetric rate is estimated to be $\sim 10^{-5}$ Mpc^{-3} yr^{-1}, or few $\times 10^{-4}$ galaxy^{-1} yr^{-1} in galaxies similar to our Milky Way (MW). Stone & Metzger (2016) investigated ways to bring theory and observation into alignment, adopting conservative assumptions that would push the loss-cone rates down; yet, the rate was calculated to be $\sim 3 \times 10^{-6}$ Mpc^{-3} yr^{-1}, or (1–2) $\times 10^{-4}$ galaxy^{-1} yr^{-1} in MW-like galaxies. Both studies suggest an expected rate that is significantly higher than the observed value of few $\times 10^{-5}$ galaxy^{-1} yr^{-1} (see Section 6.5).

One possible resolution of this issue could be substantial dust obscuration in most galactic nuclei (as suggested for blue galaxies in Section 6.5). A more theoretical resolution would be a tangentially anisotropic velocity distribution in galactic nuclei, namely a preferential destruction of stars on radial orbits. If this kind of tangential bias is put in by hand and then the nucleus is allowed to evolve, the velocity anisotropy will be washed away too quickly to solve a TDE rate discrepancy (Lezhnin & Vasiliev 2015). However, Teboul et al. (2022) recently showed that it can be sustained for longer periods of time if most galactic nuclei have steep ("strongly segregated") cusps of stellar mass BHs; in this case, the ejection in strong scatterings will eliminate stars on the most radial orbits and effectively "shield" the SMBH loss cone.

6.7. Implications of the Local BHMF

Here, we aim to independently measure the shape of the local BHMF in the mass range of $10^{5.3}\,M_\odot \leqslant M_{\rm BH} \leqslant 10^{7.3}\,M_\odot$. We assume $g(M_{\rm BH}) = 1$, and use the observed optical TDE black hole mass function (lower panel of Figure 16). To correct for the relative rate differences in red, green, and blue galaxies (Section 6.5), we compute the corrected $\phi_{\rm corr}(M_{\rm BH}) = \phi_{\rm red}(M_{\rm BH}) \times \frac{3.2}{3.7} + \phi_{\rm green}(M_{\rm BH}) \times \frac{3.2}{7.4} + \phi_{\rm blue}(M_{\rm BH}) \times \frac{3.2}{1.6}$.

Parameterizing the BHMF as $dn_{\rm BH}/d\log M_{\rm BH} \propto M_{\rm BH}^{p}$, we obtain $p = 0.014 \pm 0.059$. Note that this value is subject to the uncertainty of β in Equation (20). For example, Stone & Metzger (2016) performed the most recent detailed theoretical calculations by applying loss-cone dynamics to observations of nearby galactic nuclei, finding $\beta = -0.247$ for core nuclei, and $\beta = -0.223$ for cusp nuclei. A greater value of $\beta = -0.22$ would render a lower value of $p = -0.016 \pm 0.059$. Generally speaking, our result favors a flat BHMF in the mass range of $10^{5.3}\,M_\odot \leqslant M_{\rm BH} \leqslant 10^{7.3}\,M_\odot$. Below, we compare it with literature estimates and model predictions in Section 6.7.1, and comment on some caveats in our assessment in Section 6.7.2.

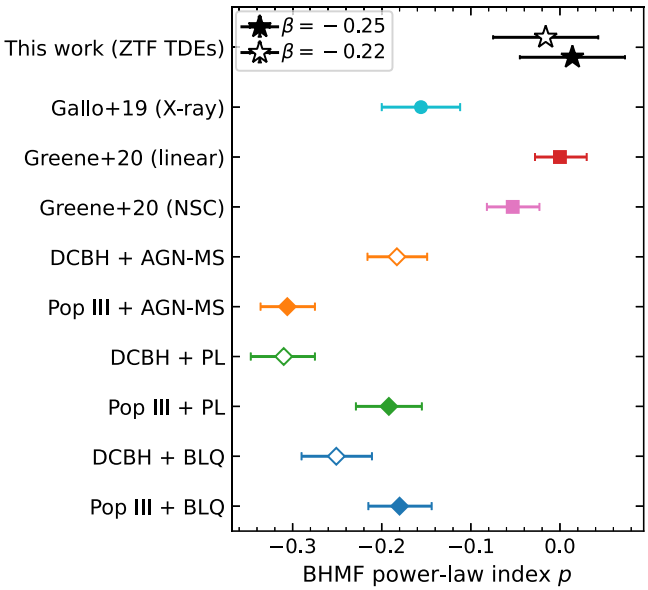

Figure 19. Power-law index of the local BHMF ($dn_{\rm BH}/d\log M_{\rm BH} \propto M_{\rm BH}^{p}$) from the optical TDE mass function (asterisks) with two assumptions on β (see Equation (20)), X-ray nuclei observations (circle, Gallo & Sesana 2019), GMF +scaling relations (squares, Greene et al. 2020), and SAMs (diamonds, Chadayammuri et al. 2023).

6.7.1. Comparison with Literature Estimates and Model Predictions

The traditional approach to calculate the local BHMF is to convert the observed galaxy distribution $\Phi(y)$ into the BHMF using a $M_{\rm BH}$–y scaling relation (see reviews by Kelly & Merloni 2012; Shankar 2013). A key assumption here is that BHs exist ubiquitously in galaxy nuclei, which has been justified in high-mass galaxies ($M_{\rm gal} \gtrsim 10^{10}\,M_\odot$; Miller et al. 2015). This approach has been widely applied to compute the BHMF at $M_{\rm BH} \gtrsim 10^{6}\,M_\odot$ (Marconi et al. 2004; Merloni & Heinz 2008; Yu & Lu 2008; Shankar et al. 2009; Vika et al. 2009; Shankar et al. 2016).

In a few nearby dwarf galaxies, however, stellar dynamical measurements have placed stringent upper limits on $M_{\rm BH}$ (e.g., Gebhardt et al. 2001; Valluri et al. 2005), suggesting that the occupation fraction in low-mass galaxies is <100%. An empirical method to constrain the occupation fraction is to use high spatial resolution Chandra X-ray observations (Gallo et al. 2008, 2010; Miller et al. 2012). By assuming that the nuclear X-ray luminosity $L_{\rm X}$ is a power-law function of $M_{\rm gal}$ with Gaussian scatter (Gallo et al. 2019), and that the occupation fraction $f_{\rm occ}(M_{\rm gal})$ follows

$$0.5 + 0.5 \times \tanh\left[2.5^{|8.9 - \log M_{\rm gal,0}|} \log(M_{\rm gal}/M_{\rm gal,0})\right], \quad (24)$$

one can simultaneously constrain the L_X–M_{gal} relation and the critical galaxy mass $M_{gal,0}$ at which $f_{occ} = 0.5$. This approach was first adopted by Miller et al. (2015) using 194 early-type galaxies, and later updated by Gallo & Sesana (2019) using 326 early-type galaxies. The latter study found a BHMF slope of $p = -0.16 \pm 0.04$ (see Figure 2 of Gallo & Sesana 2019).

The actual $f_{occ}(M_{gal})$ does not necessarily follow the functional form of Equation (24). Greene et al. (2020) assumed two different shapes of f_{occ}, with the pessimistic case drawn as a linear curve and the optimistic case provided by the fraction of nuclear star cluster (NSC) from Sánchez-Janssen et al. (2019). The authors then converted the GMF of Wright et al. (2017) into the local BHMF using the M_{BH}–M_{gal} relation (gray lines in Figure 11). The BHMFs thus derived exhibit $p = 0.00 \pm 0.03$, and $p = -0.05 \pm 0.03$ in the pessimistic case and optimistic case, respectively.

The slope of the BHMF inferred with optical TDEs is consistent with that of the Greene et al. (2020) method, whereas the Gallo & Sesana (2019) value is $\approx 2\sigma$ lower than our result (see Figure 19). Among the two BHMFs presented in Figure 6 of Greene et al. (2020), we are not able to differentiate the nuances under various f_{occ} assumptions with the current sample size.

Next, we compare our result with physically motivated BHMFs from the semianalytic models (SAMs) presented in Ricarte & Natarajan (2018a, 2018b), Ricarte et al. (2019), and Chadayammuri et al. (2023), which include halo masses down to $10^7\,M_\odot$ from redshifts $0 < z < 20$. We explore two different BH seeding models, and three different BH growth prescriptions. Population III (Pop III) models place a *light* seed initialized at approximately $10^2\,M_\odot$ in almost all dwarf galaxies by $z = 0$, while the direct collapse black hole (DCBH) models place a *heavy* seed of approximately $10^5\,M_\odot$ in a subset of these halos.

These SAMs do not model the astrophysics of galaxy formation, and instead use empirical relations to determine the BH growth rate across cosmic time. Each of them includes a *burst* mode triggered during a major merger until the BH reaches the M_{BH}–σ_* relation, and a *steady* mode that operates otherwise. Under the power-law growth, BHs grow at the Eddington rate during the burst mode, and otherwise draw from a universal power-law Eddington ratio distribution. Under the AGN-main sequence (AGN-MS) growth, BHs grow at the Eddington rate during the burst mode, and otherwise accrete at a fixed fraction of the star formation rate. The broad-line quasar (BLQ) growth only contains a burst mode, where BHs grow at an Eddington ratio drawn from a log-normal distribution that was fit to BLQs (Kelly & Shen 2013; Tucci & Volonteri 2017).

These SAMs all match the M_{BH}–σ_* relation at high masses but deviate at lower masses depending on the seeding and accretion prescriptions. Figure 19 shows the measured power-law slope of the resulting BHMFs in the mass range of $10^{5.3} < M_{BH} < 10^{7.3}\,M_\odot$. Interestingly, the SAMs generally show a higher fraction of lower-mass BHs that are not seen in the BHMF shape determined by optical TDEs.

6.7.2. Caveats

The above analysis only includes the optical TDE sample. Therefore, the implications for the local BHMF are only robust if the M_{BH} distribution of optical TDEs is representative of the underlying M_{BH} distribution of all TDEs. While previous studies do not find a significant difference in the M_{BH} distributions between optically and X-ray selected TDE samples (Wevers et al. 2019; French et al. 2020), we note that the literature samples consist of events from various surveys with different sensitivity and selection criteria. A robust assessment requires detailed understanding of how TDE emission properties (across the electromagnetic spectrum from X-ray to radio) depend on M_{BH} in a way that biases the sample M_{BH} distributions under different selection criteria.

We also note that, in order to obtain the BHMF, we assumed that the M_{BH}–σ_* relation remains valid down to $M_{BH} \sim 10^5\,M_\odot$. There are two caveats associated with this assumption: (i) the number of dynamical M_{BH} measurements at $M_{BH} \lesssim 10^6\,M_\odot$ is still insufficient to robustly test the M_{BH}–σ_* relation in the IMBH regime (Greene et al. 2020), (ii) the Kormendy & Ho (2013, Equation (3)) relation is mainly based on massive elliptical galaxies. If using the M_{BH}–σ_* relations derived by Gültekin et al. (2009), Greene et al. (2020), the inferred M_{BH} will be lower by by 0.2–0.4 dex across the range of σ_* measurements, whereas the shape of the inferred BHMF remains flat.

7. Summary

We present a complete flux-limited sample of 55 blue nuclear transients systematically selected with ZTF. Among the 55 objects, 33 are classified as TDEs. Their BH masses are inferred with host galaxy scaling relations (using central velocity dispersion σ_* for 19 objects, and using galaxy total stellar mass M_{gal} for the other 14 objects). We recovered a number of correlations between M_{BH} and photometric properties (Section 6.1).

For rate inferences, we develop a survey efficiency corrected maximum volume method (Section 5). We present the rest-frame g-band LF (Section 6.2.1), precisely constrain the upper end ($10^{43.5} \lesssim L_g \lesssim 10^{44.7}$ erg s^{-1}) for the first time, and observe a shallower slope (compared to van Velzen 2018) at the low end ($10^{42.5} \lesssim L_g \lesssim 10^{43.1}$ erg s^{-1}) that drives a $\approx 2\times$ reduction in the inferred volumetric rate. Using a newly determined LF in terms of the peak UV and optical blackbody luminosity (Section 6.2.2), we find the rates of optically loud and X-ray loud TDEs are comparable.

We construct the optical TDE mass function (Section 6.4), confirming the previous result of rate suppression due to event horizon, and revealing a $\phi(M_{BH}) \propto M_{BH}^{-0.25}$ dependence at $10^{5.3}\,M_\odot \lesssim M_{BH} \lesssim 10^{7.3}\,M_\odot$. This indicates that the local BHMF is relatively flat (Section 6.7). At a typical galaxy mass of $10^{10}\,M_\odot$, we constrain the per-galaxy TDE rate to be [3.7, 7.4, and 1.6] $\times\, 10^{-5}$ galaxy^{-1} yr^{-1} in galaxies with red, green, and blue colors, respectively (Section 6.5).

While we have mainly focused on TDE demographics in this paper, the TDE sample presented here can also be used to address the origin of TDE's UV and optical emission, and to train machine-learning algorithms (e.g., Gomez et al. 2023) for real-time photometric selection of TDE candidates. The luminosity and mass functions of optical TDEs should ultimately be compared to that of X-ray-, infrared- and radio-selected TDEs.

Over the next few years, we expect substantial progresses to be made in studies of TDE demographics. The excellent angular resolution and depth of the Vera Rubin Observatory Legacy Survey of Space and Time (Ivezić et al. 2019) will enable the creation of a reference galaxy catalog that is complete to low-mass galaxies out to higher redshifts. Since

TDE BH mass scales positively with transient duration [see Equation (10) and panel (e) of Figure 12], the selection of fast-evolving TDEs will rely on high-cadence wide-field experiments such as those conducted by ZTF, the La Silla Schmidt Southern Survey (LS4), and the wide-field (200 $\deg^2$) Ultraviolet Transient Astronomy Satellite (Ben-Ami et al. 2022).

Acknowledgments

We thank Jenny Greene for insightful discussions, and Ryan Chornock for providing the spectrum of PS1-11af. We thank Morgan MacLeod, Nick Stone, and Brian Metzger for constructive comments.

Y.Y. and S.R.K. acknowledge support from Heising-Simons Foundation. E.K.H. acknowledges support from NASA under award No. 80GSFC21M0002. M.N. is supported by the European Research Council (ERC) under the European Unions Horizon 2020 research and innovation program (grant agreement No. 948381) and by funding from the UK Space Agency. This research benefited from interactions at workshops funded by the Gordon and Betty Moore Foundation through grant GBMF5076. This research was made possible in part through the support of grants from the Gordon and Betty Moore Foundation and the John Templeton Foundation. The opinions expressed in this publication are those of the author(s) and do not necessarily reflect the views of the Moore or Templeton Foundations.

This work is based on observations obtained with the Samuel Oschin Telescope 48 inch and the 60 inch Telescope at the Palomar Observatory as part of the Zwicky Transient Facility project. ZTF is supported by the National Science Foundation under grants No. AST-1440341 and AST-2034437 and a collaboration including current partners Caltech, IPAC, the Weizmann Institute of Science, the Oskar Klein Center at Stockholm University, the University of Maryland, Deutsches Elektronen-Synchrotron and Humboldt University, the TANGO Consortium of Taiwan, the University of Wisconsin at Milwaukee, Trinity College Dublin, Lawrence Livermore National Laboratories, IN2P3, University of Warwick, Ruhr University Bochum, Northwestern University and former partners the University of Washington, Los Alamos National Laboratories, and Lawrence Berkeley National Laboratories. Operations are conducted by Caltech Optical Observatories, IPAC, and University of Washington.

The ZTF forced-photometry service was funded under the Heising-Simons Foundation grant No. 12540303 (PI: Graham). SED Machine is based upon work supported by the National Science Foundation under grant No. 1106171.

This work has made use of data from the Asteroid Terrestrial-impact Last Alert System (ATLAS) project. The ATLAS project is primarily funded to search for near-Earth asteroids through NASA grants NN12AR55G, 80NSSC18K0284, and 80NSSC18K1575; byproducts of the near-earth object search include images and catalogs from the survey area. This work was partially funded by Kepler/K2 grant J1944/80NSSC19K0112 and Hubble Space Telescope GO-15889, and STFC grants ST/T000198/1 and ST/S006109/1. The ATLAS science products have been made possible through the contributions of the University of Hawaii Institute for Astronomy, the Queens University Belfast, the Space Telescope Science Institute, the South African Astronomical Observatory, and The Millennium Institute of Astrophysics (MAS), Chile.

Appendix A
Supplementary Tables

The UV and optical photometry of 33 TDEs is presented in Table 6. The observing logs of low-resolution spectroscopy and ESI spectroscopy are provided in Tables 7 and 8, respectively. The pre-flare host galaxy photometry is provided in Tables 9 and 10.

Table 6
UV and Optical Photometry of 33 TDEs

IAU Name	MJD	Instrument	Filter	f_ν (μJy)	σ_{f_ν} (μJy)
AT2021mhg	59421.5384	ATLAS	*o*	23.2366	8.7284
AT2021mhg	59422.3478	ZTF	*i*	6.4130	11.8362
AT2021mhg	59422.4213	ZTF	*r*	29.2828	3.0782
AT2021mhg	59422.4560	ZTF	*g*	50.9955	4.8532
AT2021mhg	59424.3924	ZTF	*r*	23.6341	3.0218
AT2021uqv	59454.7033	UVOT	*uvw*1	92.3872	8.6091
AT2021uqv	59454.7044	UVOT	*U*	80.0122	13.5501
AT2021uqv	59454.7062	UVOT	*uvw*2	89.1477	6.2627
AT2021uqv	59454.7097	UVOT	*uvm*2	91.1047	6.2769
AT2021uqv	59455.3383	ZTF	*g*	70.7813	4.0499
AT2021yzv	59524.3409	ZTF	*g*	88.7688	2.8362
AT2021yzv	59524.3631	ZTF	*r*	72.1670	2.9713
AT2021yzv	59524.5512	ATLAS	*c*	79.4877	3.7740
AT2021yzv	59526.3054	ZTF	*i*	58.4191	5.1675
AT2021yzv	59526.3680	ZTF	*g*	84.3688	2.6204

Note. f_ν is observed flux density before extinction correction.

(This table is available in its entirety in machine-readable form.)

Table 7
Log of Low-resolution Optical Spectroscopy

ID	IAU Name	Start Date	t (days)	Telescope	Instrument	Wavelength Range (Å)	Slit Width (″)	Exposure Time (s)
17	AT2020vwl	2021-01-11.5	+54	LDT	DeVeny	3586–8034	1.5	2700
19	AT2020yue	2022-11-17.6[a]	+599	Keck I	LRIS	3200–10250	1.0	2700
		2022-11-25.6[a]	+605	Keck I	LRIS	3200–10250	1.0	2400
20	AT2020abri	2022-04-07.5	+395	Keck I	LRIS	3200–10250	1.0	1500
21	AT2020acka	2021-01-14.5	+7	P60	SEDM	3770–9223	⋯	2700
		2021-01-16.5	+9	P60	SEDM	3770–9223	⋯	2700
		2021-02-08.5	+26	P60	SEDM	3770–9223	⋯	2700
		2021-02-20.5	+31	P200	DBSP	3410–5550, 5750–9995	1.5	1200
		2021-04-14.5	+70	Keck I	LRIS	3200–10250	1.0	400
		2021-06-07.5	+111	Keck I	LRIS	3200–10250	1.0	430
		2021-08-13.3	+161	Keck I	LRIS	3200–10250	1.0	430
		2021-09-07.3	+179	Keck I	LRIS	3200–10250	1.0	900
		2022-02-06.6	+293	Keck I	LRIS	3200–10250	1.0	900
22	AT2021axu	2021-06-07.3	+100	Keck I	LRIS	3200–10250	1.0	485
23	AT2021crk	2021-04-09.4	+34	P200	DBSP	3410–5550, 5750–9995	1.5	1200
25	AT2021jjm	2021-05-13.5	+17	Keck I	LRIS	3200–10250	1.0	300
26	AT2021mhg	2021-08-01.4	+51	P200	DBSP	3410–5550, 5750–9995	1.5	1800
27	AT2021nwa	2021-07-06.3	−1	Keck I	LRIS	3200–10250	1.0	300
28	AT2021qth	2021-08-04.2	+27	P200	DBSP	3410–5550, 5750–9995	1.5	900
		2022-05-26.3	+300	Keck I	LRIS	3200–10250	1.0	900
29	AT2021sdu	2021-08-13.4	+18	Keck I	LRIS	3200–10250	1.0	750
30	AT2021uqv	2021-09-17.5	+25	Keck I	LRIS	3200–10250	1.0	600
31	AT2021utq	2022-10-03.2	+353	P200	DBSP	3410–5550, 5750–9995	1.0	1500
32	AT2021yzv	2021-10-04.6	−15	Keck I	LRIS	3200–10250	1.0	600
		2022-02-05.3	+80	Keck I	LRIS	3200–10250	1.0	900
		2023-01-16.4	+349	Keck I	LRIS	3200–10250	1.0	1200
33	AT2021yte	2021-10-14.5	+14	P200	DBSP	3410–5550, 5750–9995	1.5	900

Note.
[a] On 2022 November 17, one exposure (900 s) on the red CCD is badly affected by cosmic rays and is therefore not included in spectral extraction. We stack the observations on 2022 November 17 and 2022 November 25 together to create a deep spectrum for analysis.

Table 8
Details of ESI Spectroscopy

ID	IAU Name	Start Date	Slit Width (″)	Exposure Time (s)	$r_{\rm extract}$ (pixel)	Fitted $\lambda_{\rm rest}$ (Å)	σ_* (km s^{-1})	S/N
1	AT2018iih	2022-07-04.5	0.5	1200	4.2	5030–5600	148.6 ± 14.4	6.9
5	AT2019azh	2022-10-21.6	0.5	1200	5.7	5030–5600	68.0 ± 2.0	33.3
8	AT2019dsg	2022-08-24.4	0.5	900	4.3	5030–5600	86.9 ± 3.9	16.9
13	AT2020mot	2022-10-21.4	0.5	1200	9.3	5030–5600	76.6 ± 5.3	8.8
15	AT2020ysg	2023-03-26.4	0.75	2400	7.8	5030–5392, 5407–5600	157.8 ± 13.0	13.6
16	AT2020vdq	2022-11-25.5	0.3	2700	5.8	5030–5600	43.6 ± 3.1	12.0
17	AT2020vwl	2022-03-07.6	0.5	600	4.2	5030–5600	48.5 ± 2.0	11.6
18	AT2020wey	2022-10-22.6	0.5	600	8.2	5030–5600	40.1 ± 3.1	7.4
21	AT2020acka	2022-03-07.6	0.5	2400	6.0	5030–5127, 5159–5600	174.5 ± 25.3	9.1
22	AT2021axu	2022-03-07.3	0.5	1500	4.3	5030–5600	73.5 ± 17.3	7.2
		2022-11-25.6	0.5	2400				
23	AT2021crk	2022-03-07.3	0.5	1600	5.6	5030–5083, 5137–5600	57.6 ± 6.3	6.8

Table 8
(Continued)

ID	IAU Name	Start Date	Slit Width ($''$)	Exposure Time (s)	$r_{\rm extract}$ (pixel)	Fitted $\lambda_{\rm rest}$ (Å)	σ_* (km s^{-1})	S/N
		2022-11-25.6	0.5	2400				
24	AT2021ehb	2021-12-28.4	0.75	300	5.0	5030–5600	99.6 ± 3.8	18.4
26	AT2021mhg	2022-10-22.3	0.5	1800	4.2	5030–5196, 5200–5600	57.8 ± 5.3	8.1
27	AT2021nwa	2022-03-07.7	0.5	600	4.6	5030–5600	102.4 ± 5.4	11.3
30	AT2021uqv	2022-08-24.5	0.5	1200	5.0	5030–5310, 5346–5600	62.3 ± 7.1	10.6
32	AT2021yzv	2023-03-26.3	0.75	2400	8.2	4900–5335, 5369–5600	146.4 ± 20.8	8.6
33	AT2021yte	2022-03-07.2	0.5	1120	3.8	5030–5578	34.2 ± 4.8	7.3

Note. All ESI spectra were obtained after the optical TDE flux has faded to <10% of the host galaxy flux. $r_{\rm extract}$ can be converted to angular scale using a conversion factor of $0\farcs154$ per pixel.

Table 9
GALEX, SDSS, and WISE Photometry of TDE Host Galaxies

ID	FUV[a]	NUV	SDSS/u	SDSS/g	SDSS/r	SDSS/i	SDSS/z	WISE/W1	WISE/W2
1				20.55 ± 0.19	19.24 ± 0.16	18.80 ± 0.17	18.28 ± 0.17		
2		23.73 ± 0.89		22.73 ± 0.28	21.32 ± 0.13	20.95 ± 0.14	20.23 ± 0.17	20.59 ± 0.57	20.66 ± 0.45
3								19.57 ± 0.19	20.91 ± 0.62
4	20.91 ± 0.27	20.19 ± 0.12	19.63 ± 0.13	18.37 ± 0.03	17.69 ± 0.01	17.28 ± 0.02	17.11 ± 0.19	17.02 ± 0.04	17.47 ± 0.04
5	19.24 ± 0.18	17.83 ± 0.03	16.51 ± 0.08	15.01 ± 0.02	14.49 ± 0.01	14.20 ± 0.01	14.04 ± 0.04	14.60 ± 0.01	15.23 ± 0.02
6	22.51 ± 1.04	21.12 ± 0.23	20.13 ± 0.28	19.00 ± 0.04	18.24 ± 0.02	17.81 ± 0.03	17.71 ± 0.10	17.78 ± 0.04	18.36 ± 0.05
7								19.22 ± 0.13	19.89 ± 0.17
8	21.19 ± 0.32	21.22 ± 0.26						15.65 ± 0.02	16.16 ± 0.02
9		22.54 ± 0.19	20.29 ± 0.30	19.28 ± 0.06	18.52 ± 0.07	18.24 ± 0.07	17.96 ± 0.18	18.50 ± 0.07	19.08 ± 0.09
10								13.95 ± 0.02	14.60 ± 0.04
11	21.12 ± 0.09	20.87 ± 0.04	20.04 ± 0.10	19.07 ± 0.02	18.55 ± 0.01	18.23 ± 0.02	17.97 ± 0.06	18.40 ± 0.05	18.90 ± 0.07
12			20.05 ± 0.09	18.63 ± 0.02	17.90 ± 0.01	17.50 ± 0.02	17.33 ± 0.04	17.56 ± 0.04	18.13 ± 0.04
13	22.65 ± 0.64	21.56 ± 0.25						16.66 ± 0.03	17.21 ± 0.03
14	20.91 ± 0.34	19.61 ± 0.11	19.18 ± 0.09	18.20 ± 0.01	17.68 ± 0.02	17.35 ± 0.02	17.23 ± 0.05	17.53 ± 0.05	18.01 ± 0.05
15		21.97 ± 0.25	21.79 ± 0.70	21.14 ± 0.26	19.81 ± 0.07	19.22 ± 0.07	19.46 ± 0.35	18.59 ± 0.07	19.10 ± 0.08
16			19.80 ± 0.14	18.87 ± 0.02	18.26 ± 0.02	18.05 ± 0.02	17.94 ± 0.12	18.48 ± 0.11	18.98 ± 0.12
17			18.81 ± 0.12	17.24 ± 0.02	16.53 ± 0.02	16.18 ± 0.01	15.90 ± 0.05	16.48 ± 0.03	17.16 ± 0.04
18	21.82 ± 0.34	21.61 ± 0.09	18.88 ± 0.09	17.40 ± 0.01	16.70 ± 0.01	16.34 ± 0.01	16.11 ± 0.02	16.63 ± 0.03	17.22 ± 0.03
19	21.98 ± 0.34	21.09 ± 0.15						18.49 ± 0.07	19.10 ± 0.09
20			23.14 ± 0.64	21.83 ± 0.14	21.00 ± 0.07	20.63 ± 0.07	20.83 ± 0.35	20.75 ± 0.20	
21			22.84 ± 0.89	21.07 ± 0.11	19.71 ± 0.07	19.09 ± 0.08	18.66 ± 0.17	18.18 ± 0.14	18.65 ± 0.16
22				20.34 ± 0.04	19.57 ± 0.03	19.29 ± 0.06	18.77 ± 0.15	19.33 ± 0.10	20.15 ± 0.20
23			20.52 ± 0.21	19.51 ± 0.04	19.04 ± 0.05	18.68 ± 0.07	18.50 ± 0.28	18.98 ± 0.10	19.80 ± 0.18
24			17.66 ± 0.06	15.86 ± 0.01	14.98 ± 0.01	14.50 ± 0.01	14.18 ± 0.02	14.57 ± 0.02	15.25 ± 0.02
25								19.98 ± 0.19	20.11 ± 0.17
26								18.70 ± 0.10	19.30 ± 0.10
27	23.29 ± 0.17	22.05 ± 0.09	19.22 ± 0.10	17.67 ± 0.01	16.90 ± 0.01	16.51 ± 0.01	16.24 ± 0.03	16.69 ± 0.03	17.29 ± 0.03
28		22.51 ± 0.38							
29		20.01 ± 0.14						16.11 ± 0.04	16.62 ± 0.03
30	21.76 ± 0.39	20.76 ± 0.13	20.33 ± 0.39	18.79 ± 0.05	18.14 ± 0.05	17.78 ± 0.04	17.62 ± 0.07	17.72 ± 0.06	18.16 ± 0.07
31	21.88 ± 0.51	21.61 ± 0.31						19.55 ± 0.44	20.49 ± 1.05
32								18.68 ± 0.11	19.19 ± 0.16
33			20.62 ± 0.36					18.03 ± 0.25	18.73 ± 0.30

Note.
[a] FUV as far-UV.

Table 10
PS1 and 2MASS Photometry of TDE Host Galaxies

ID	PS1/g	PS1/r	PS1/i	PS1/z	PS1/y	2MASS/J	2MASS/H	2MASS/K_s
1	20.42 ± 0.22	19.18 ± 0.15	18.74 ± 0.15	18.54 ± 0.16	18.55 ± 0.27	18.66 ± 0.41	17.99 ± 0.32	17.66 ± 0.28
2	23.02 ± 0.67	21.55 ± 0.17	20.96 ± 0.15	20.72 ± 0.18	20.78 ± 0.34			
3	20.41 ± 0.26	19.57 ± 0.14	19.20 ± 0.13	19.16 ± 0.22	18.93 ± 0.15			
4	18.34 ± 0.05	17.70 ± 0.03	17.29 ± 0.01	17.10 ± 0.03	16.82 ± 0.06			
5	14.99 ± 0.03	14.48 ± 0.01	14.26 ± 0.01	14.09 ± 0.02	13.88 ± 0.03	13.71 ± 0.01	13.61 ± 0.02	13.77 ± 0.03
6	18.94 ± 0.03	18.24 ± 0.02	17.85 ± 0.03	17.57 ± 0.05	17.34 ± 0.05		17.17 ± 0.12	
7		21.53 ± 0.15	20.63 ± 0.10	20.63 ± 0.14	20.11 ± 0.22			
8	17.03 ± 0.04	16.20 ± 0.02	15.83 ± 0.02	15.57 ± 0.03	15.39 ± 0.06	15.02 ± 0.02	15.02 ± 0.03	15.13 ± 0.04
9	19.30 ± 0.07	18.65 ± 0.10	18.28 ± 0.06	18.21 ± 0.08	18.03 ± 0.11			
10	15.01 ± 0.05	14.33 ± 0.03	13.91 ± 0.06	13.69 ± 0.04	13.44 ± 0.05	13.26 ± 0.02	12.95 ± 0.02	13.26 ± 0.03
11	19.03 ± 0.02	18.52 ± 0.01	18.27 ± 0.02	18.05 ± 0.03	17.97 ± 0.06	17.62 ± 0.12	17.69 ± 0.16	
12	18.54 ± 0.03	17.92 ± 0.02	17.51 ± 0.02	17.34 ± 0.03	17.06 ± 0.05	16.72 ± 0.05	16.83 ± 0.10	17.04 ± 0.12
13	17.99 ± 0.03	17.20 ± 0.01	16.76 ± 0.01	16.53 ± 0.02	16.39 ± 0.05	16.05 ± 0.04		15.98 ± 0.06
14	18.10 ± 0.04	17.68 ± 0.04	17.33 ± 0.02	17.20 ± 0.02	17.07 ± 0.06			
15	21.44 ± 0.26	19.88 ± 0.09	19.37 ± 0.04	19.10 ± 0.08	19.26 ± 0.28			
16	18.79 ± 0.06	18.30 ± 0.03	18.03 ± 0.02	17.88 ± 0.03	17.82 ± 0.09			
17	17.17 ± 0.05	16.51 ± 0.03	16.16 ± 0.03	16.03 ± 0.03	15.87 ± 0.06	15.77 ± 0.05	15.38 ± 0.05	15.67 ± 0.08
18	17.32 ± 0.01	16.69 ± 0.01	16.36 ± 0.01	16.15 ± 0.01	16.00 ± 0.03			
19	19.74 ± 0.11	19.33 ± 0.05	18.89 ± 0.09	18.71 ± 0.21	18.40 ± 0.16			
20	22.00 ± 0.15	20.87 ± 0.05	20.64 ± 0.06	20.63 ± 0.09	20.26 ± 0.19			
21		19.84 ± 0.13	19.17 ± 0.07	18.89 ± 0.07	18.69 ± 0.24	18.32 ± 0.17	18.01 ± 0.21	17.67 ± 0.15
22	20.32 ± 0.05	19.53 ± 0.05	19.17 ± 0.04	19.01 ± 0.07				
23	19.66 ± 0.07	19.09 ± 0.06	18.86 ± 0.05	18.63 ± 0.07	18.62 ± 0.15			
24	15.73 ± 0.02	14.93 ± 0.01	14.49 ± 0.01	14.21 ± 0.01	13.98 ± 0.02	13.83 ± 0.01	13.62 ± 0.01	13.80 ± 0.01
25	20.44 ± 0.06	20.08 ± 0.04	19.82 ± 0.05	19.58 ± 0.04	19.67 ± 0.12			
26	19.63 ± 0.07	18.93 ± 0.03	18.55 ± 0.08	18.33 ± 0.07	18.25 ± 0.09	18.26 ± 0.18	18.30 ± 0.26	18.07 ± 0.22
27	17.56 ± 0.02	16.88 ± 0.02	16.52 ± 0.01	16.27 ± 0.02	16.17 ± 0.04	15.87 ± 0.04	15.59 ± 0.04	15.91 ± 0.07
28	19.84 ± 0.09	19.01 ± 0.09	18.58 ± 0.13	18.33 ± 0.09	18.09 ± 0.12			
29	17.49 ± 0.02	16.84 ± 0.02	16.39 ± 0.05	16.18 ± 0.05	15.93 ± 0.06	15.73 ± 0.03	15.79 ± 0.05	15.46 ± 0.04
30	18.79 ± 0.03	18.19 ± 0.03	17.88 ± 0.01	17.78 ± 0.04	17.53 ± 0.11	17.35 ± 0.13	17.29 ± 0.17	
31	20.03 ± 0.06	19.53 ± 0.08	19.19 ± 0.07	18.98 ± 0.11	18.91 ± 0.11	19.08 ± 0.52		
32	20.96 ± 0.15	19.90 ± 0.14	19.25 ± 0.06	19.04 ± 0.12	18.80 ± 0.13		18.09 ± 0.29	
33	19.34 ± 0.22	18.65 ± 0.26	18.18 ± 0.25	18.09 ± 0.33	17.77 ± 0.24	17.90 ± 0.14	17.92 ± 0.23	

Appendix B
Details of Sample Selection

Here, we justify a few selection cuts adopted in Section 2.2.

B.1. sgscore1

The `sgscore` parameter is close to 1 (0) for a star-like (galaxy-like) morphology. Its value is set to 0.5 if the PS1 counterpart is not "detected" in the PS1 `StackObjectAttributes` table (see details in Tachibana & Miller 2018; Miller & Hall 2021). In Figure 20, we show the distribution of the 55 photometric TDE candidates (after step (7) in Section 2.2) on the `magnr` versus `sgscore1` diagram. The highest value of `sgscore` is 0.5, implying that our selection cut of `sgscore1` is sufficiently liberal.

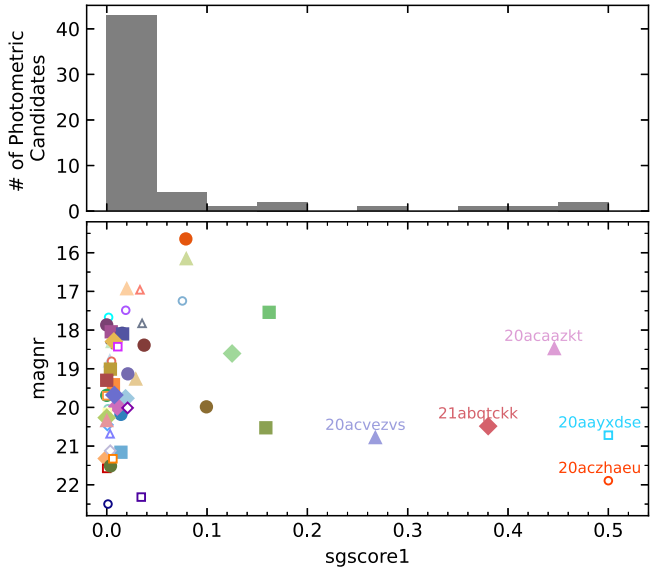

Figure 20. The `sgscore1` (star–galaxy classification score) and `magnr` (magnitude of the nearest object in the ZTF reference image) parameters of 55 photometric TDE candidates. Symbol colors follow the same convention as in Figure 2. The 33 TDEs are shown in solid markers, and the 22 false positives are shown in hollow markers. We show the ZTF names for objects with `sgscore1>0.2`.

B.2. Rise and Decline Timescales

In Figure 21, the observer-frame e-folding rise and decline timescales (computed using the best-fit models derived in Section 3) are shown versus $M_{\rm BH}$. The values are well within the boundaries of 2 and 300 days, implying that our criteria adopted in steps (5) and (6) of Section 2.2 are not at the boundaries.

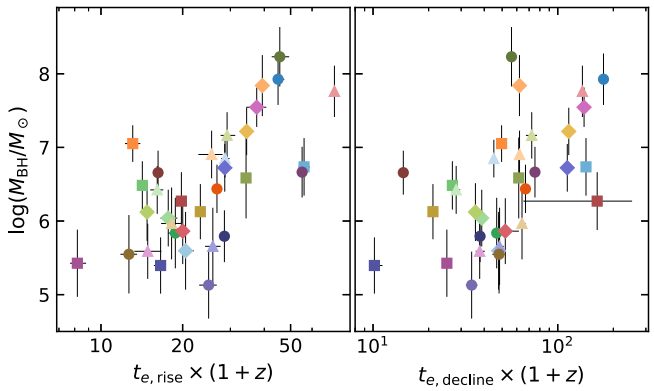

Figure 21. The black hole mass and observer-frame e-folding rise and decline timescales of 33 TDEs.

Appendix C
Host Galaxy SEDs and Comparison with Previous Studies

Figure 22 shows the SEDs of 33 TDE host galaxies.

There are 13 galaxies in common between our sample and Hammerstein et al. (2023). The left panel of Figure 23 shows the distributions of these objects on the galaxy color–mass diagram, using values derived in this work and Hammerstein et al. (2023). For nine of the 13 objects, the $\log(M_{\rm gal}/M_{\odot})$ and ${}^{0,0}u-r$ parameters are consistent with each other (to within 2σ). For the other four objects (AT2019qiz, AT2019vcb, AT2019azh, and AT2020ysg), the difference probably comes from the different source of photometry: Hammerstein et al. (2023) obtained photometry from various catalogs whereas we measured the host brightness using `LAMBDAR` (see Section 4).

There are 7 galaxies in common between our sample and that from Ramsden et al. (2022). The mean offset in $\log(M_{\rm gal}/M_{\odot})$ between this work and that from Ramsden et al. (2022) is -0.17 dex (see the right panel of Figure 23). The difference could be because Ramsden et al. (2022) used a nonparametric SFH, whereas we assumed a delayed exponentially declining function.

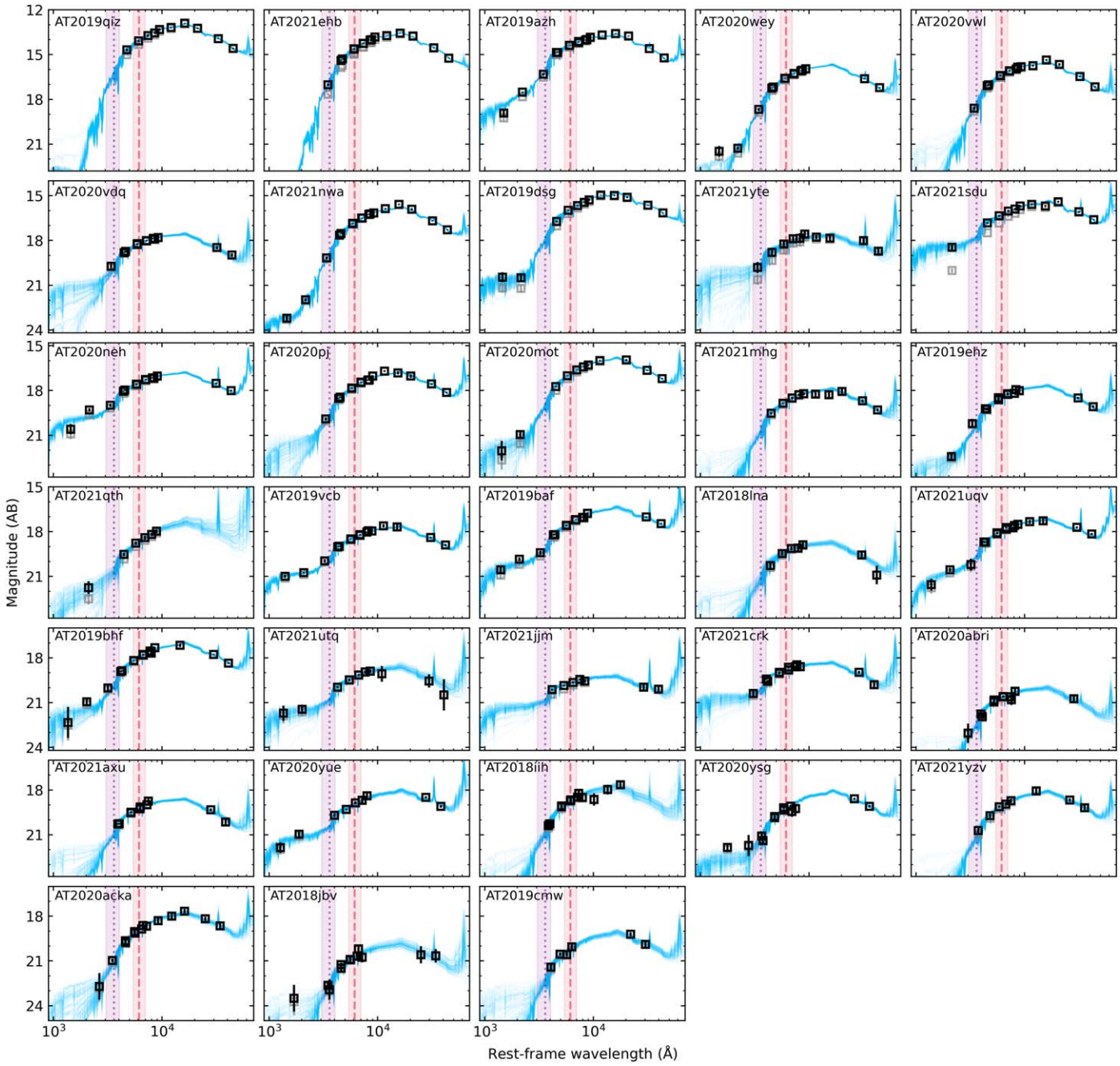

Figure 22. Host galaxy SEDs (sorted by redshift). The gray and black squares show the observed and Galactic extinction-corrected photometry, respectively. The blue lines show models of the 100 walkers in the MCMC sampler. The dotted and dashed vertical lines mark rest-frame wavelength of the SDSS u and r filters.

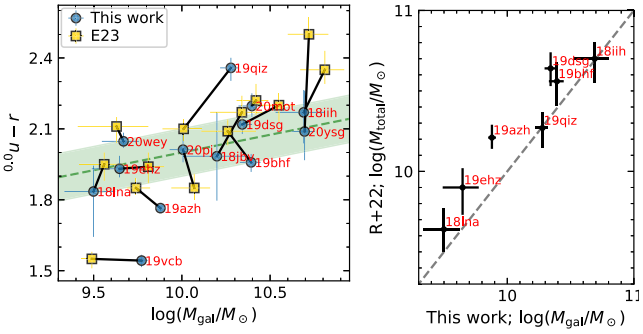

Figure 23. Left: distributions of 13 galaxies on the color–mass diagram in both this work and Hammerstein et al. (2023). Data points for the same object are connected with the solid black lines. The dashed green line shows the green valley defined by Equation (22). Right: comparison of host galaxy total stellar mass derived in this work and Ramsden et al. (2022).

ORCID iDs

Yuhan Yao https://orcid.org/0000-0001-6747-8509
Vikram Ravi https://orcid.org/0000-0002-7252-5485
Suvi Gezari https://orcid.org/0000-0003-3703-5154
Sjoert van Velzen https://orcid.org/0000-0002-3859-8074
Wenbin Lu https://orcid.org/0000-0002-1568-7461
Steve Schulze https://orcid.org/0000-0001-6797-1889
Jean J. Somalwar https://orcid.org/0000-0001-8426-5732
S. R. Kulkarni https://orcid.org/0000-0001-5390-8563
Erica Hammerstein https://orcid.org/0000-0002-5698-8703
Matt Nicholl https://orcid.org/0000-0002-2555-3192
Matthew J. Graham https://orcid.org/0000-0002-3168-0139
Daniel A. Perley https://orcid.org/0000-0001-8472-1996
S. Bradley Cenko https://orcid.org/0000-0003-1673-970X
Robert Stein https://orcid.org/0000-0003-2434-0387
Angelo Ricarte https://orcid.org/0000-0001-5287-0452
Eliot Quataert https://orcid.org/0000-0001-9185-5044
Eric C. Bellm https://orcid.org/0000-0001-8018-5348
Joshua S. Bloom https://orcid.org/0000-0002-7777-216X
Richard Dekany https://orcid.org/0000-0002-5884-7867
Andrew J. Drake https://orcid.org/0000-0003-0228-6594
Steven L. Groom https://orcid.org/0000-0001-5668-3507
Ashish A. Mahabal https://orcid.org/0000-0003-2242-0244
Thomas A. Prince https://orcid.org/0000-0002-8850-3627
Reed Riddle https://orcid.org/0000-0002-0387-370X
Ben Rusholme https://orcid.org/0000-0001-7648-4142
Yashvi Sharma https://orcid.org/0000-0003-4531-1745
Jesper Sollerman https://orcid.org/0000-0003-1546-6615
Lin Yan https://orcid.org/0000-0003-1710-9339

References

Abazajian, K. N., Adelman-McCarthy, J. K., Agüeros, M. A., et al. 2009, ApJS, 182, 543
Ahn, C. P., Alexandroff, R., Allende Prieto, C., et al. 2012, ApJS, 203, 21
Aird, J., Coil, A. L., Moustakas, J., et al. 2012, ApJ, 746, 90
Alexander, T. 2017, ARA&A, 55, 17
Amaro Seoane, P. 2022, in Handbook of Gravitational Wave Astronomy, ed. C. Bambi, S. Katsanevas, & K. Kokkotas (Singapore: Springer), 17
Amaro-Seoane, P., Audley, H., Babak, S., et al. 2017, arXiv:1702.00786
Angus, C. R. 2021, TNSCR, 2021-2291, 1
Angus, C. R., Baldassare, V. F., Mockler, B., et al. 2022, NatAs, 6, 1452
Arcavi, I., Burke, J., Nyiha, I., et al. 2020, TNSCR, 2020-3228, 1
Arcavi, I., Gal-Yam, A., Sullivan, M., et al. 2014, ApJ, 793, 38
Bade, N., Komossa, S., & Dahlem, M. 1996, A&A, 309, L35
Bailer-Jones, C. A. L., Rybizki, J., Fouesneau, M., Mantelet, G., & Andrae, R. 2018, AJ, 156, 58
Baldry, I. K., Driver, S. P., Loveday, J., et al. 2012, MNRAS, 421, 621
Beck, R., Szapudi, I., Flewelling, H., et al. 2021, MNRAS, 500, 1633
Bellm, E. C., Kulkarni, S. R., Barlow, T., et al. 2019b, PASP, 131, 068003
Bellm, E. C., Kulkarni, S. R., Graham, M. J., et al. 2019a, PASP, 131, 018002
Ben-Ami, S., Shvartzvald, Y., Waxman, E., et al. 2022, Proc. SPIEs, 12181, 1218105
Blagorodnova, N., Neill, J. D., Walters, R., et al. 2018, PASP, 130, 035003
Blanchard, P. K., Nicholl, M., Berger, E., et al. 2017, ApJ, 843, 106
Bonnerot, C., & Lu, W. 2020, MNRAS, 495, 1374
Bonnerot, C., Rossi, E. M., Lodato, G., & Price, D. J. 2016, MNRAS, 455, 2253
Brown, J. S., Holoien, T. W. S., Auchettl, K., et al. 2017, MNRAS, 466, 4904
Bruch, R., Strotjohann, N., Gal-Yam, A., et al. 2021, TNSAN, 200, 1
Burke, J., Arcavi, I., Lam, M., et al. 2021, TNSCR, 2021-3259, 1
Calzetti, D., Armus, L., Bohlin, R. C., et al. 2000, ApJ, 533, 682
Cappellari, M. 2017, MNRAS, 466, 798
Cappellari, M., & Emsellem, E. 2004, PASP, 116, 138
Cardelli, J. A., Clayton, G. C., & Mathis, J. S. 1989, ApJ, 345, 245
Cenko, S. B., Fox, D. B., Moon, D.-S., et al. 2006, PASP, 118, 1396
Chabrier, G. 2003, PASP, 115, 763
Chadayammuri, U., Bogdán, Á., Ricarte, A., & Natarajan, P. 2023, ApJ, 946, 51
Chambers, K. C., Magnier, E. A., Metcalfe, N., et al. 2016, arXiv:1612.05560
Charalampopoulos, P., Leloudas, G., Malesani, D. B., et al. 2022, A&A, 659, A34
Charalampopoulos, P., Pursiainen, M., Leloudas, G., et al. 2023, A&A, 673, A95
Chomiuk, L., Chornock, R., Soderberg, A. M., et al. 2011, ApJ, 743, 114
Chornock, R., Berger, E., Gezari, S., et al. 2014, ApJ, 780, 44
Chu, M., Dahiwale, A., & Fremling, C. 2021a, TNSCR, 2021-3438, 1
Chu, M., Dahiwale, A., & Fremling, C. 2021b, TNSCR, 2021-2672, 1
Chu, M., Dahiwale, A., & Fremling, C. 2021c, TNSCR, 2021-2712, 1
Chu, M., Dahiwale, A., & Fremling, C. 2022, TNSCR, 2022-363, 1
Conroy, C., Gunn, J. E., & White, M. 2009, ApJ, 699, 486
Coughlin, E. R., & Begelman, M. C. 2014, ApJ, 781, 82
Dahiwale, A., & Fremling, C. 2020a, TNSCR, 2020-3800, 1
Dahiwale, A., & Fremling, C. 2020b, TNSCR, 2020-534, 1
Dahiwale, A., & Fremling, C. 2020c, TNSCR, 2020-3308, 1
Dahiwale, A., & Fremling, C. 2020d, TNSCR, 2020-1756, 1
Dahiwale, A., & Fremling, C. 2020e, TNSCR, 2020-601, 1
Dahiwale, A., & Fremling, C. 2021, TNSCR, 2021-1378, 1
Dai, L., McKinney, J. C., & Miller, M. C. 2015, ApJL, 812, L39
Dai, L., McKinney, J. C., Roth, N., Ramirez-Ruiz, E., & Miller, M. C. 2018, ApJL, 859, L20
Dekany, R., Smith, R. M., Riddle, R., et al. 2020, PASP, 132, 038001
Demircan, O., & Kahraman, G. 1991, Ap&SS, 181, 313
Du, P., Egaña-Ugrinovic, D., Essig, R., Fragione, G., & Perna, R. 2022, NatCo, 13, 4626
Duev, D. A., Mahabal, A., Masci, F. J., et al. 2019, MNRAS, 489, 3582
Flesch, E. W. 2019, arXiv:1912.05614
Flewelling, H. A., Magnier, E. A., Chambers, K. C., et al. 2020, ApJS, 251, 7
Foreman-Mackey, D., Hogg, D. W., Lang, D., & Goodman, J. 2013, PASP, 125, 306
Foreman-Mackey, D., Sick, J., & Johnson, B. 2014, Python-Fsps: Python Bindings To Fsps, v0.1.1, Zenodo, doi:10.5281/zenodo.12157
Frederick, S., Gezari, S., Graham, M. J., et al. 2021, ApJ, 920, 56
Fremling, C., Miller, A. A., Sharma, Y., et al. 2020, ApJ, 895, 32
French, K. D., Arcavi, I., & Zabludoff, A. 2016, ApJL, 818, L21
French, K. D., Wevers, T., Law-Smith, J., Graur, O., & Zabludoff, A. I. 2020, SSRv, 216, 32
Gallo, E., Hodges-Kluck, E., Treu, T., et al. 2019, BAAS, 51, 35
Gallo, E., & Sesana, A. 2019, ApJL, 883, L18
Gallo, E., Treu, T., Jacob, J., et al. 2008, ApJ, 680, 154
Gallo, E., Treu, T., Marshall, P. J., et al. 2010, ApJ, 714, 25
Gebhardt, K., Lauer, T. R., Kormendy, J., et al. 2001, AJ, 122, 2469
Gehrels, N. 1986, ApJ, 303, 336
Gehrels, N., Chincarini, G., Giommi, P., et al. 2004, ApJ, 611, 1005
Gezari, S. 2021, ARA&A, 59, 21
Gezari, S., Basa, S., Martin, D. C., et al. 2008, ApJ, 676, 944
Gezari, S., Chornock, R., Rest, A., et al. 2012, Natur, 485, 217
Gezari, S., Heckman, T., Cenko, S. B., et al. 2009, ApJ, 698, 1367
Gezari, S., Martin, D. C., Milliard, B., et al. 2006, ApJL, 653, L25
Gomez, S., Villar, V. A., Berger, E., et al. 2023, ApJ, 949, 113
Graham, M. J., Kulkarni, S. R., Bellm, E. C., et al. 2019, PASP, 131, 078001
Greene, J. E., Strader, J., & Ho, L. C. 2020, ARA&A, 58, 257
Grupe, D., Thomas, H. C., & Leighly, K. M. 1999, A&A, 350, L31

Gültekin, K., Richstone, D. O., Gebhardt, K., et al. 2009, ApJ, 698, 198
Hammerstein, E., Gezari, S., van Velzen, S., et al. 2021d, ApJL, 908, L20
Hammerstein, E., Gezari, S., Velzen, S. V., et al. 2021a, TNSCR, 2021-159, 1
Hammerstein, E., Gezari, S., Velzen, S. V., et al. 2021b, TNSCR, 2021-262, 1
Hammerstein, E., Gezari, S., Velzen, S. V., et al. 2021c, TNSCR, 2021-955, 1
Hammerstein, E., van Velzen, S., Gezari, S., et al. 2023, ApJ, 942, 9
Hills, J. G. 1975, Natur, 254, 295
Hinkle, J. T., Holoien, T. W. S., Auchettl, K., et al. 2021, MNRAS, 500, 1673
Ho, A. Y. Q., Perley, D. A., Gal-Yam, A., et al. 2023, ApJ, 949, 120
Holoien, T. W. S., Prieto, J. L., Bersier, D., et al. 2014, MNRAS, 445, 3263
Huang, H.-T., & Lu, W. 2022, arXiv:2301.00259
Hung, T., Gezari, S., Blagorodnova, N., et al. 2017, ApJ, 842, 29
Jani, K., Shoemaker, D., & Cutler, C. 2020, NatAs, 4, 260
Jiang, Y.-F., Guillochon, J., & Loeb, A. 2016, ApJ, 830, 125
Johnson, B. D., Leja, J., Conroy, C., & Speagle, J. S. 2021, ApJS, 254, 22
Ivezić, Ž., Kahn, S. M., Tyson, J. A., et al. 2019, ApJ, 873, 111
Kangas, T., Yan, L., Schulze, S., et al. 2022, MNRAS, 516, 1193
Kelly, B. C., & Merloni, A. 2012, AdAst, 2012, 970858
Kelly, B. C., & Shen, Y. 2013, ApJ, 764, 45
Kesden, M. 2012, PhRvD, 85, 024037
Kewley, L. J., Groves, B., Kauffmann, G., & Heckman, T. 2006, MNRAS, 372, 961
Kim, Y. L., Rigault, M., Neill, J. D., et al. 2022, PASP, 134, 024505
Kochanek, C. S. 2016, MNRAS, 461, 371
Komossa, S., Zhou, H., Wang, T., et al. 2008, ApJL, 678, L13
Kormendy, J., & Ho, L. C. 2013, ARA&A, 51, 511
Lacy, M., Baum, S. A., Chandler, C. J., et al. 2020, PASP, 132, 035001
Lang, D. 2014, AJ, 147, 108
Latimer, L. J., Reines, A. E., Bogdan, A., & Kraft, R. 2021a, ApJL, 922, L40
Latimer, L. J., Reines, A. E., Hainline, K. N., Greene, J. E., & Stern, D. 2021b, ApJ, 914, 133
Law-Smith, J., Ramirez-Ruiz, E., Ellison, S. L., & Foley, R. J. 2017, ApJ, 850, 22
Lezhnin, K., & Vasiliev, E. 2015, ApJL, 808, L5
Lin, Z., Jiang, N., Kong, X., et al. 2022, ApJL, 939, L33
Loeb, A., & Ulmer, A. 1997, ApJ, 489, 573
Lu, W., & Bonnerot, C. 2020, MNRAS, 492, 686
MacLeod, M., Guillochon, J., & Ramirez-Ruiz, E. 2012, ApJ, 757, 134
MacLeod, M., Ramirez-Ruiz, E., Grady, S., & Guillochon, J. 2013, ApJ, 777, 133
Magorrian, J., & Tremaine, S. 1999, MNRAS, 309, 447
Mahabal, A., Rebbapragada, U., Walters, R., et al. 2019, PASP, 131, 038002
Mainzer, A., Bauer, J., Grav, T., et al. 2011, ApJ, 731, 53
Marconi, A., Risaliti, G., Gilli, R., et al. 2004, MNRAS, 351, 169
Margalit, B., Quataert, E., & Ho, A. Y. Q. 2022, ApJ, 928, 122
Martin, D. C., Fanson, J., Schiminovich, D., et al. 2005, ApJL, 619, L1
Masci, F. J., Laher, R. R., Rusholme, B., et al. 2019, PASP, 131, 018003
Mendel, J. T., Simard, L., Palmer, M., Ellison, S. L., & Patton, D. R. 2014, ApJS, 210, 3
Merloni, A., & Heinz, S. 2008, MNRAS, 388, 1011
Merritt, D., & Ferrarese, L. 2001, ApJ, 547, 140
Metzger, B. D. 2022, ApJL, 937, L12
Metzger, B. D., & Stone, N. C. 2016, MNRAS, 461, 948
Miller, A. A., & Hall, X. J. 2021, PASP, 133, 054502
Miller, B., Gallo, E., Treu, T., & Woo, J.-H. 2012, ApJ, 747, 57
Miller, B. P., Gallo, E., Greene, J. E., et al. 2015, ApJ, 799, 98
Miller, M. C. 2015, ApJ, 805, 83
Million, C., Fleming, S. W., Shiao, B., et al. 2016, ApJ, 833, 292
Nicholl, M., Berger, E., Blanchard, P. K., Gomez, S., & Chornock, R. 2019a, ApJ, 871, 102
Nicholl, M., Short, P., Lawrence, A., et al. 2019b, TNSCR, 2019-2271, 1
Nicholl, M., Blanchard, P. K., Berger, E., et al. 2019c, MNRAS, 488, 1878
Nicholl, M., Lanning, D., Ramsden, P., et al. 2022, MNRAS, 515, 5604
Nicholl, M., Wevers, T., Oates, S. R., et al. 2020, MNRAS, 499, 482
Nordin, J., Brinnel, V., van Santen, J., et al. 2019, A&A, 631, A147
Oke, J. B., Cohen, J. G., Carr, M., et al. 1995, PASP, 107, 375
Oke, J. B., & Gunn, J. E. 1982, PASP, 94, 586
Onori, F., Cannizzaro, G., Jonker, P. G., et al. 2019, MNRAS, 489, 1463
Palaversa, L., Gezari, S., Sesar, B., et al. 2016, ApJ, 819, 151
Patterson, M. T., Bellm, E. C., Rusholme, B., et al. 2019, PASP, 131, 018001
Perez-Fournon, I., Poidevin, F., Angel, C. J., et al. 2020, TNSCR, 2020-2456, 1
Perley, D. A., Taggart, K., Dahiwale, A., & Fremling, C. 2020a, TNSCR, 2020-2086, 1
Perley, D. A., Fremling, C., Sollerman, J., et al. 2020b, ApJ, 904, 35
Pessi, P. J., Anderson, J., Galbany, L., & Yaron, O. 2020, TNSCR, 2020-3712, 1
Pinkney, J., Gebhardt, K., Bender, R., et al. 2003, ApJ, 596, 903
Piran, T., Svirski, G., Krolik, J., Cheng, R. M., & Shiokawa, H. 2015, ApJ, 806, 164
Predehl, P., Andritschke, R., Arefiev, V., et al. 2021, A&A, 647, A1
Prugniel, P., & Soubiran, C. 2001, A&A, 369, 1048
Prugniel, P., Soubiran, C., Koleva, M., & Le Borgne, D. 2007, arXiv:astro-ph/0703658
Quimby, R. M., Kulkarni, S. R., Kasliwal, M. M., et al. 2011, Natur, 474, 487
Raftery, A. E. 1995, Sociol. Methodol., 25, 111
Ramsden, P., Lanning, D., Nicholl, M., & McGee, S. L. 2022, MNRAS, 515, 1146
Rees, M. J. 1988, Natur, 333, 523
Reines, A. E., & Volonteri, M. 2015, ApJ, 813, 82
Reynolds, C. S. 2021, ARA&A, 59, 117
Ricarte, A., & Natarajan, P. 2018a, MNRAS, 481, 3278
Ricarte, A., & Natarajan, P. 2018b, MNRAS, 474, 1995
Ricarte, A., Pacucci, F., Cappelluti, N., & Natarajan, P. 2019, MNRAS, 489, 1006
Rigault, M., Neill, J. D., Blagorodnova, N., et al. 2019, A&A, 627, A115
Roming, P. W. A., Kennedy, T. E., Mason, K. O., et al. 2005, SSRv, 120, 95
Roth, N., & Kasen, D. 2018, ApJ, 855, 54
Roth, N., Kasen, D., Guillochon, J., & Ramirez-Ruiz, E. 2016, ApJ, 827, 3
Roth, N., van Velzen, S., Cenko, S. B., & Mushotzky, R. F. 2021, ApJ, 910, 93
Sánchez-Janssen, R., Côté, P., Ferrarese, L., et al. 2019, ApJ, 878, 18
Saxton, R., Komossa, S., Auchettl, K., & Jonker, P. G. 2020, SSRv, 216, 85
Sazonov, S., Gilfanov, M., Medvedev, P., et al. 2021, MNRAS, 508, 3820
Schawinski, K., Urry, C. M., Simmons, B. D., et al. 2014, MNRAS, 440, 889
Schlafly, E. F., & Finkbeiner, D. P. 2011, ApJ, 737, 103
Schmidt, M. 1968, ApJ, 151, 393
Schulze, S., Yaron, O., Sollerman, J., et al. 2021, ApJS, 255, 29
Shankar, F. 2013, CQGra, 30, 244001
Shankar, F., Bernardi, M., Sheth, R. K., et al. 2016, MNRAS, 460, 3119
Shankar, F., Weinberg, D. H., & Miralda-Escudé, J. 2009, ApJ, 690, 20
Sheinis, A. I., Bolte, M., Epps, H. W., et al. 2002, PASP, 114, 851
Shingles, L., Smith, K. W., Young, D. R., et al. 2021, TNSAN, 7, 1
Siebert, M. 2020, TNSCR, 2020-1469, 1
Skrutskie, M. F., Cutri, R. M., Stiening, R., et al. 2006, AJ, 131, 1163
Smith, K. W., Smartt, S. J., Young, D. R., et al. 2020, PASP, 132, 085002
SNIascore 2021, TNSCR, 2021-1939, 1
Somalwar, J. J., Ravi, V., Dong, D., et al. 2022, ApJ, 929, 184
Soumagnac, M. T., & Ofek, E. O. 2018, PASP, 130, 075002
Stein, R., Velzen, S. v., Kowalski, M., et al. 2021, NatAs, 5, 510
Stone, N. C., Kesden, M., Cheng, R. M., & van Velzen, S. 2019, GReGr, 51, 30
Stone, N. C., & Metzger, B. D. 2016, MNRAS, 455, 859
Stone, N. C., Vasiliev, E., Kesden, M., et al. 2020, SSRv, 216, 35
Strauss, M. A., Weinberg, D. H., Lupton, R. H., et al. 2002, AJ, 124, 1810
Sunyaev, R., Arefiev, V., Babyshkin, V., et al. 2021, A&A, 656, A132
Tachibana, Y., & Miller, A. A. 2018, PASP, 130, 128001
Teboul, O., Stone, N. C., & Ostriker, J. P. 2022, arXiv:2211.05858
Thomsen, L. L., Kwan, T. M., Dai, L., et al. 2022, ApJL, 937, L28
Tonry, J. L., Denneau, L., Heinze, A. N., et al. 2018, PASP, 130, 064505
Tucci, M., & Volonteri, M. 2017, A&A, 600, A64
Tucker, M. A. 2021, TNSCR, 2021-433, 1
Valluri, M., Ferrarese, L., Merritt, D., & Joseph, C. L. 2005, ApJ, 628, 137
van Velzen, S. 2018, ApJ, 852, 72
van Velzen, S., Farrar, G. R., Gezari, S., et al. 2011, ApJ, 741, 73
van Velzen, S., Gezari, S., Cenko, S. B., et al. 2019, ApJ, 872, 198
van Velzen, S., Gezari, S., Hammerstein, E., et al. 2021, ApJ, 908, 4
van Velzen, S., Holoien, T. W. S., Onori, F., Hung, T., & Arcavi, I. 2020, SSRv, 216, 124
Vika, M., Driver, S. P., Graham, A. W., & Liske, J. 2009, MNRAS, 400, 1451
Wang, J., & Merritt, D. 2004, ApJ, 600, 149
Wevers, T., Stone, N. C., van Velzen, S., et al. 2019, MNRAS, 487, 4136
Wevers, T., van Velzen, S., Jonker, P. G., et al. 2017, MNRAS, 471, 1694
Woods, T. E., Agarwal, B., Bromm, V., et al. 2019, PASA, 36, e027
Wright, A. H., Robotham, A. S. G., Bourne, N., et al. 2016, MNRAS, 460, 765
Wright, A. H., Robotham, A. S. G., Driver, S. P., et al. 2017, MNRAS, 470, 283
Yan, L., Lunnan, R., Perley, D., Schulze, S., & Chen, T. W. 2020, TNSCR, 2020-3640, 1
Yao, Y. 2021, TNSCR, 2021-3411, 1
Yao, Y. 2022, TNSCR, 2022-2915, 1
Yao, Y., Chu, M., Das, K. K., et al. 2021a, TNSCR, 2021-3611, 1

Yao, Y., Gezari, S., Velzen, S. V., Hammerstein, E., & Somalwar, J. 2021b, TNSCR, 2021-2155, 1
Yao, Y., Hammerstein, E., Gezari, S., et al. 2021c, TNSCR, 2021-2535, 1
Yao, Y., Lu, W., Guolo, M., et al. 2022a, ApJ, 937, 8
Yao, Y., Ho, A. Y. Q., Medvedev, P., et al. 2022b, ApJ, 934, 104
Yao, Y., Miller, A. A., Kulkarni, S. R., et al. 2019, ApJ, 886, 152
Yao, Y., Velzen, S. V., Perley, D., et al. 2021d, TNSCR, 2021-1632, 1
Yaron, O., & Gal-Yam, A. 2012, PASP, 124, 668
Yu, Q., & Lu, Y. 2008, ApJ, 689, 732
Yu, Z., Kochanek, C. S., Mathur, S., et al. 2022, MNRAS, 515, 5198